MODELING RELATIVISTIC HEAVY ION COLLISIONS

By

Sen Cheng

A DISSERTATION

Submitted to
Michigan State University
in partial fulfillment of the requirements
for the degree of

DOCTOR OF PHILOSOPHY

Department of Physics and Astronomy

2002

ABSTRACT

MODELING RELATIVISTIC HEAVY ION COLLISIONS

By

Sen Cheng

Experiments with relativistic heavy-ion collisions offer the prospect of studying a range of novel phenomena. One such phenomenon is the restoration and rebreaking of chiral symmetry, which might lead to detectable consequences in the fluctuations of charged vs. neutral pions. Alternative sources for isospin fluctuations such as total isospin conservation, Bose-Einstein symmetrization, and hadronic resonance decays are examined in this work. Exact and calculable expressions are derived for multiplicity distributions and isospin fluctuations within a canonical ensemble, in which additive quantum numbers and total isospin are strictly conserved.

Most attention in the research of relativistic heavy-ion collisions is directed toward creating and studying the quark-gluon plasma, a new state of matter predicted by lattice Quantum Chromodynamics calculations. Discerning the consequences of the phase transition from the collision debris requires extensive numerical modeling. To this end, a new framework for modeling relativistic heavy-ion collisions, Gromit, is developed in this work on the basis of the Boltzmann transport equation. Gromit overcomes the limitations of previous numerical descriptions through its modular construction and improved collision finding meshes and collision algorithms.

The new framework is employed to study some general properties of microscopic transport models such as the role of viscosities due to finite-range interactions and the sensitivi-

ties of observables like elliptic flow and particle spectra to the sampling factor λ. Gromit is also used to explore the influence of secondary hadronic interactions on balance functions, a new observable proposed as a possible signal of a new state of matter. As previous definitions of balance functions were applicable only for vanishing net charge, a new formulation for extracting balance functions in the presence of net charges is introduced and studied.

Furthermore, a new technique is presented for calculating two-pion correlations from microscopic models. The technique accounts for quantum corrections due to pions originating from resonance decays. Considering a simple thermal model, the importance of such quantum corrections is quantified by comparing to semi-classical methods.

To Vini and my family.

ACKNOWLEDGMENTS

This thesis could only be completed with the help of many people and organizations, to whom I am very much indebted. In particular, I would like to thank the "Studienstiftung des deutschen Volkes" and Wolfgang Bauer for the initial financial support that brought me to Michigan State University; the National Superconducting Cyclotron Laboratory for providing an excellent workplace; Marc-Jan van Goethem for proof-reading my thesis; my adviser Scott Pratt for academic and professional support, particularly during the last year when times were rough for both of us; and Malini Vinita Samarasinghe and my family for much and often needed moral support, which kept me going.

Table of Contents

List of Tables

List of Figures

Chapter 1

Introduction

All interactions in the universe can be described in terms of four fundamental interactions: gravitation, electromagnetism, the weak force, and the strong force. Macroscopically, gravitation is well explained by the theory of general relativity but it is generally neglected at the scale of elementary particles because its strength is 30 or more orders of magnitude smaller than that of the weak force. The electromagnetic and weak forces, however, were successfully combined into the electro-weak force and theoretically described by an $SU(2) \otimes U(1)$ gauge theory [76, 153]. The strong force is represented by Quantum Chromodynamics (QCD), a nonAbelian $SU(3)$ gauge theory, as interaction between colored quarks [73, 87].

In the theory of QCD, the exchange bosons, gluons, carry color charge and therefore interact with each other. The interaction between gluons has a profound impact on the behavior of QCD and is responsible for its peculiar properties like confinement of quarks and gluons into hadrons, asymptotic freedom [83, 82, 84], and a running coupling constant α_s that decreases with energy transfer. This property of the strong coupling is the reason why the perturbative expansion order-by-order in α_s can only yield satisfactory results for high-energy scattering experiments, such as those that first observed the top quark at Fermilab [1, 2]. Perturbative QCD (pQCD) cannot be applied to describe phenomena at length scales above 0.1 fm. This prevents pQCD from describing the binding of quarks

into hadrons or describing the condensation of gluonic and quark degrees of freedom into the vacuum condensates. These condensates couple to the quarks that comprise hadrons and are responsible for most of the mass of the proton and therefore most of the mass of the universe.

A nonperturbative approach to deal with the complexity of QCD is lattice QCD, where space is discretized into cells and partition functions are calculated by Monte Carlo sampling (see for example [51]). Lattice QCD can be used to calculate the phase diagram for quark-gluon matter, which has recently become feasible even for finite chemical potential [68, 67]. The calculated QCD phase diagrams show a deconfinement phase transition from hadronic matter to a plasma of free quarks and gluons. The order of this transition depends on the degrees of freedom used in the lattice calculation and remains a theoretical uncertainty [40, 98]. Originally, the quark-gluon plasma (QGP) had been postulated by extrapolating the notion of asymptotic freedom to a hot and dense environment [48, 69, 46, 140]. It was thought that if the strength of the interaction between quarks decreased with smaller distances, then quarks should form a liberated plasma at high temperatures and densities.

The critical temperature for the phase transition from ordinary hadronic matter to the QGP is predicted to be on the order of 150–200 MeV, varying between different lattice calculations. The extreme conditions necessary to create a QGP existed at around 5 μs after the big bang and might also exist within the interiors of massive stars. There is also a prospect of creating and studying the QGP in accelerator experiments by colliding relativistic heavy ions, which has led to several experiments at either fixed target machines, such as the Alternating Gradient Synchrotron (AGS) at the Brookhaven National Laboratory (BNL) and the Super Proton Synchrotron (SPS) at the European Organization for Nuclear Research (CERN), or colliders such as the Relativistic Heavy Ion Collider (RHIC) at BNL and the planned Large Hadron Collider (LHC) at CERN.

One aspect of the potential phase transition at high temperature and/or density is the restoration of chiral symmetry, which is expected to occur concurrently with the deconfinement transition. Chiral symmetry is a spontaneously broken symmetry of QCD in the limit of zero quark masses with the pion as the associated Goldstone boson. The spontaneous breaking of chiral symmetry leads to a nonzero expectation value for the scalar quark–anti-quark condensate at low temperatures and densities. This condensate is melted as chiral symmetry is restored at high temperature and/or density. As the system cools off and chiral symmetry is spontaneously broken again, all directions along the pion fields and the scalar quark–anti-quark field are equally probable. The chosen direction at recondensation might not coincide with the usual scalar quark–anti-quark condensate, which is referred to as disoriented chiral condensate (DCC) [16, 17, 33, 133, 132]. As chiral symmetry is also explicitly broken, the DCC would eventually decay, possibly leading to measurable signatures.

Nucleus-nucleus collisions create a phase of hot and dense matter that subsequently cools quickly. Therefore, irrespective of whether a QCD phase transition took place during the evolution of the collision process, only ordinary photons, leptons, and hadrons escape the collision region and reach the detectors. The challenge in relativistic heavy-ion collision experiments is to reconstruct the hot and dense phase, which lasted on the order of 10^{-23} s and had an extent on the order of 10^{-15} m, from its remnants. Although lattice QCD predicts the existence of a QGP, it offers little guidance on this reconstruction as it can neither describe hadronization nor the hadronic interactions thereafter. Quantum mechanical treatments such as solving the Klein-Gordon or Dirac Equations are not feasible in this case because of the large number of independent particles involved (at RHIC typically around 6000). They also might not be required because the thermal wavelength is small compared to the size of the system.

Semi-classical models have provided the basis to gaining insight into the collision dy-

namics of a relativistic heavy-ion collision and have proven to be essential to designing experiments, analyzing data, and making detailed predictions. In a simplified picture, most models for relativistic heavy-ion collisions can be fit into three major categories: hydrodynamical or statistical models, Glauber-type models, and microscopic models.

Hydrodynamical models were employed in the 1950's to describe the dynamics of pp collisions because the underlying processes were not well understood and the models relied mainly on the basic physical principles of energy and momentum conservation [66, 122, 104]. These models assume local thermal equilibrium and neglect viscosities, surface energy, Coulomb energy, and single-particle effects, when modeling the collision system as a nuclear fluid. The first numerical solution of hydrodynamics for collisions of heavy ions became feasible in 1975 [11, 12]. Hydrodynamical models have evolved into a workhorse for predicting and understanding measurements of observables at RHIC energies, e.g., [141, 102]. However, despite the maturity of these models, some challenges remain, such as the inclusion of viscosities in the numerical treatments [112].

Glauber-type models exploit the well-understood dynamics of nucleon-nucleon collisions. Nucleus-nucleus (AA) collisions are modeled by dividing the nuclei into nucleons with some density distribution and describing the entire reaction as a superposition of binary nucleon-nucleon collisions [14, 138, 151, 41, 94]. These models provide invaluable benchmarks to compare with experimental results since they only contain dynamics from nucleon-nucleon collisions, in which the number of interactions between quarks and gluon is insufficient to create the temperature and energy density needed for the phase transition to a QGP.

Microscopic transport models describe the dynamics of a relativistic heavy-ion collision by modeling its microscopic constituents and their interactions. Such models are currently available in a wide variety of flavors, ranging from quantum molecular dynamics

[143, 23] to solutions of the Boltzmann Transport Equation (BTE) in its various incarnations [120, 109, 107, 10, 62, 114, 159, 72, 154]. Some of these models are based on transport theory that has a long history dating back to the works of Boltzmann and Maxwell on the kinetic theory of gases in the 1870's. Over time, the original Boltzmann equation has been modified to incorporate new physical insights like relativity, quantum statistics, and the nuclear mean field. In addition to choosing the equations that they solve, microscopic models select the degrees of freedom, i.e. partons, hadrons, Lund string phenomenology [15, 13], or subsets thereof; the interactions between those particles; and the numerical solution techniques. This flexibility might account for the wide variety of currently available models that fall into this category. The main appeal of microscopic transport models derives from their ability to describe nonequilibrium phenomena [85, 109], as opposed to hydrodynamical models, which have to rest on the assumption of local thermal equilibrium.

It should be mentioned that some models transcend the categories mentioned above by either following different ideas like solving the equations of motion of classical QCD color fields [58] or by combining several models into a hybrid model, where different stages of the relativistic heavy-ion collision are treated with different models. Some hybrid models combine microscopic models for different degrees of freedom [144, 162] in an attempt to choose the most appropriate description for the various stages of the collision. For example, one approach [22, 146] employs a hydrodynamical model for the first part of the collision, where the assumption of local thermal equilibrium seems most justified, and a microscopic transport model for the later stages.

The theoretical and experimental study of relativistic heavy-ion collisions has yielded a wealth of knowledge about the dynamics of a relativistic heavy-ion collision. When viewing a relativistic heavy-ion collision at RHIC energies in the center of mass frame (c.m.f.) the following time evolution picture emerges (see for example [113]):

In the *initial stage* two Lorentz-contracted nuclei head toward each other at nearly light speed. These nuclei pass through each other within a time less than 0.1 fm/c, during which on the order of 10^4 quarks, anti-quarks, and gluons interact with each other and create a region of hot and dense matter. The system persists in this *preequilibrium stage* for about 0.1– 1.0 fm/c until local thermal equilibrium is established through collisions. In addition to the deconfinement phase transition to a QGP that might take place in this stage, there might be a concurrent restoration of chiral symmetry.

Once the *equilibrium stage* is reached, the system consists of either a liberated plasma of quarks and gluons or excited hadronic matter, depending on whether there was a deconfinement phase transition. In case a QGP was created, quarks and gluons have to be confined into hadrons, once the system temperature falls below the critical value, which is predicted by lattice QCD to be on the order of 150–200 MeV. The hadrons appearing at this *hadronization phase transition* are formed significantly later in the collision than in the scenario without QGP.

In either scenario, the system ends up in the *hadronic stage*, where hadrons decay and interact with each other until the system is so dilute, i.e., the inter-particle spacing so large, that the hadrons cease to interact. *Chemical freeze-out* is marked by the drop in the rates of inelastic collisions which are required to maintain equilibrium in the abundances of the various particle types. *Kinetic (or thermal) freeze-out* is marked by the drop in the rate of elastic collisions necessary to maintain the thermal shapes of the local momentum distributions. Chemical freeze-out is expected to occur simultaneously with hadronization [127], whereas kinetic equilibrium should be maintained until the particles have their last interactions.

The goal of this thesis is to study signatures that reveal the processes within relativistic heavy-ion collisions and to provide means for modeling the dynamics of such collisions.

One proposed signature of the disoriented chiral condensate (DCC) is anomalous isospin fluctuations, which would indicate a restoration and rebreaking of chiral symmetry. To test the validity of this signature of the DCC, alternative sources for such fluctuations are studied in Chapter 2 by considering the influence of total isospin conservation, quantum symmetrization, and resonance decays. Exact and calculable expressions are derived for multiplicity distributions and isospin fluctuations within a canonical ensemble, in which additive quantum numbers and total isospin are strictly conserved. It is found that the combined effect of total isospin conservation, quantum symmetrization, and resonance decays cannot account for anomalous isospin fluctuations.

Chapter 3 of this thesis introduces Gromit, a modular framework for building microscopic transport models for the study of relativistic heavy-ion collisions. Gromit was developed and written entirely within the RHIC Transport Theory Collaboration (RTTC) [137]. The collaboration's goal is to develop thoroughly tested and documented models that are available to the community on an open-source basis. Model assumptions about degrees of freedom and interactions are entirely modular and can be easily replaced to independently test nearly every assumption made in a model. New features like mean fields, novel cross sections, and dynamic linking to other models can be easily incorporated into the existing framework.

The influence of numerical artifacts and arbitrary algorithmic choices in microscopic transport models is investigated in Chapter 4. Observables like elliptic flow and particle spectra are found to be sensitive to the sampling factor λ, but fortunately, rather small values of λ are sufficient for extracting reliable results. These findings indicate that transport models based on the Boltzmann Equation are invalid in the cascade limit, $\lambda = 1$, and that solutions converge in the Boltzmann limit, $\lambda \to \infty$.

The importance of viscosities in relativistic heavy-ion collision is explored in Chapter

5. The consequences of a nonzero interaction range are studied by varying the interaction range in the scattering kernel, while leaving the mean free path unchanged. Finite interaction range is demonstrated to contribute viscous terms in a manner similar to the finite mean free path, but with different dependencies with respect to density and temperature. In particular, a comparison of heating derived from an analysis of the collision kernel with the heating observed in a simplified simulation is presented.

The influence of resonance decays on pion correlation functions is studied in Chapter 6. Correlations between particles originating from a common source are generally introduced through quantum statistics and contain information about the spacetime extent of the source. The importance of quantum treatments for the extraction of correlation functions from microscopic models is quantified by comparing to semi-classical forms for a simple thermal model. It is found that quantum corrections become important when kinematics constrain the resonances to be off shell. An alteration of the methods for extracting correlations from classical simulations is proposed to better account for quantum effects. This modification can account for the quantum corrections by incorporating information regarding the off-shell energy of the decaying resonance.

Finally, Gromit is used in Chapter 7 to explore the influence of hadronic interactions on balance functions, a new observable proposed as a possible signal of late-stage hadronization. Balance functions quantify on a statistical basis the relative location of charge–anti-charge pairs, which are created together. It is found that secondary hadronic interactions widen the $\pi^+\pi^-$ balance function in relative rapidity, but not in $q^2_{\rm inv}$. The wider balance function in relative rapidity is argued to be merely a consequence of cooling due to hadronic rescattering. It is also demonstrated that previous definitions of balance functions are applicable only for a small net charge. A new formulation for extracting balance functions in the presence of net charges is introduced. Though not entirely efficient, the new balance function is shown to remove the dramatic effects of the net electric charge of the protons.

The above findings on the effect of hadronic interactions on the balance function remain valid when studied with the corrected balance function.

It should be noted that parts of Chapter 4 (namely Section 4.1 and Subsection 4.2.1) and Chapters 5 and 6 have been previously published in a similar form [43, 45] and that Chapter 2 has been submitted for publication [44].

Chapter 2

Isospin Fluctuations in Ensembles with Exact Quantum Number and Isospin Conservation

The temperatures and densities created in a relativistic heavy-ion collision, e.g. at RHIC, are believed to be sufficiently high for the restoration of chiral symmetry. A brief description of this approximate symmetry in given in the next section. The subsequent rebreaking of this symmetry as the collision region cools can then lead to the creation of a disoriented chiral condensate (DCC). This concept was first introduced to explain the observation of large fluctuations in the ratio of neutral to charged particles in cosmic ray events [16, 17, 33, 133, 132]. These so-called Centauro events [105, 37], have sparked numerous studies of isospin fluctuations during the last decade. It has been proposed that the melting and subsequent recondensation of the chiral condensate could provide a dynamical means for coherent pion emission where dozens of pions are emitted with the same isospin. If N pions are confined to a single quantum state in addition to being in an isosinglet [92], the probability of finding n_0 neutral pions takes a simple form in the limit of large $N = n_+ + n_- + n_0$,

$$\frac{dN}{df} = \frac{1}{2\sqrt{f}}, \quad f \equiv n_0/N. \tag{2.1}$$

The same result can be obtained by considering a coherent state

$$|\vec{\eta}\rangle = \exp(\vec{\eta}\cdot\vec{\pi})\,|0\rangle, \tag{2.2}$$

where the pion field operators are $\pi_0 = \pi_z$, $\pi_\pm = (\pi_x \pm i\pi_y)/\sqrt{2}$, and the direction of $\vec{\eta}$ is averaged over all directions. The source of the field $\vec{\eta}$ has been proposed to be the chiral condensate which might disorient itself in a quenching scenario.

Alternative sources for such isospin fluctuations have been studied. The dramatically broad isospin distribution of Eq. (2.1) relies on the assumption that the emission proceeds via a single quantum state. The inclusion of Bose-Einstein effects in the thermal emission of pions from a nondegenerate array of states was shown to broaden the isospin distribution [124] with respect to a random distribution, but not nearly as much as in Eq. (2.1). Neglecting isospin conservation in [124] accounted for the reduced broadening of the peak. A crude accounting for isospin conservation was suggested by considering the emission of neutral pion pairs (2/3 $\pi^+\pi^-$ and 1/3 $2\pi_0$) [128], but came far short of considering the complete ensemble of isoscalar states in a multi-level system. The emission of pairs through a classical isoscalar field into nondegenerate single-particle levels, which may be considered as an oriented chiral condensate, has been studied as well [150].

The effects of exact charge conservation in canonical ensembles were also studied in other contexts with a projection method. Strangeness and baryon number conservation were found to restrict strangeness productions in $\bar{p}pN$ collisions, particularly for small systems [56]. The confinement of the quark-gluon plasma to color-singlets was shown to lead to a reduction in the number of internal degrees of freedom, which could lead to measurable finite size effects in relativistic heavy ion collisions [64, 65, 63].

In the following, the sophistication of statistical treatments is extended by considering the entire ensemble of isoscalar states available in a system with many single-particle levels. Methods for calculating isospin distributions are presented, which include Bose-Einstein

symmetrization, the effects of resonances and the conservation of both total isospin I and its projection M. Sample calculations are presented to illustrate the above-mentioned effects. It is found that symmetrization effects are important for high quantum degeneracies, that isospin conservation has little impact when the size of the domain exceeds a dozen pions, and that resonances can strongly narrow the distribution.

2.1 Chiral Symmetry in Nuclear Physics

The notion of chiral symmetry was inspired by studies of nuclear beta decay. There, the weak coupling constant for the hadronic vector current C_V was found to coincide with the leptonic analogue, and the coupling for the axial vector current C_A was determined to differ by only 25% from that for the leptonic counterparts. Chiral symmetry was proposed to explain the conservation of both currents [1] and can be well illustrated with the linear sigma model which was proposed by Gell-Mann and Levy [74] as a model for nucleons before QCD was known as the theory of the strong interaction.

The linear sigma model describes interactions between the nucleon field ψ as couplings to two meson fields, the isovector pion field π and a hypothetical scalar sigma field σ. The Lagrangian for the linear sigma model is given by

$$\mathcal{L} = i\bar{\psi}\,\partial\!\!\!/\,\psi - g_\pi(i\bar{\psi}\gamma_5\tau\psi\pi + \bar{\psi}\psi\sigma) + \frac{1}{2}\partial_\mu\pi\partial^\mu\pi + \frac{1}{2}\partial_\mu\sigma\partial^\mu\sigma, \tag{2.3}$$

where τ are the Pauli (iso)spin matrices and g_π is the coupling constant for the interaction. This Lagrangian was defined such that it is invariant under the following vector transformation

$$\Lambda_V: \quad \psi \longrightarrow e^{-i\tau\theta/2}\psi \approx (1 - i\tau\theta/2)\,\psi \tag{2.4}$$

$$\bar{\psi} \longrightarrow e^{+i\tau\theta/2}\bar{\psi} \approx (1 + i\tau\theta/2)\,\bar{\psi}. \tag{2.5}$$

[1] The fact that the axial vector current is only partially conserved is ignored for the moment and introduced later as explicit breaking of chiral symmetry.

Like any other symmetry, this symmetry is associated with a conserved charge or current as stated by the Noether theorem. In this case the vector current associated with Λ_V,

$$V_\mu^a = \bar{\psi}\gamma_\mu \frac{\tau^a}{2}\psi, \tag{2.6}$$

is simply the isospin current. Another symmetry of the chiral Lagrangian is the invariance under the axial vector transformation

$$\Lambda_A: \quad \psi \longrightarrow e^{-i\gamma_5\tau\theta/2}\psi \approx (1 - i\gamma_5\tau\theta/2)\psi \tag{2.7}$$

$$\bar{\psi} \longrightarrow e^{-i\gamma_5\tau\theta/2}\bar{\psi} \approx (1 - i\gamma_5\tau\theta/2)\bar{\psi}. \tag{2.8}$$

The associated axial current,

$$A_\mu^a = \bar{\psi}\gamma_\mu\gamma_5 \frac{\tau^a}{2}\psi, \tag{2.9}$$

is not easily associated with a physical current because chiral symmetry is only an approximate symmetry. The invariance of the Lagrangian in Eq. (2.3) under both transformations Λ_V and Λ_A is referred to as chiral symmetry.

Although the Lagrangian is invariant under the transformations Λ_V and Λ_A, the ground state is not. This is known as spontaneous symmetry breaking and is imposed through the potential

$$V = \frac{\xi}{4}\left((\pi^2 + \sigma^2) - f_\pi^2\right)^2, \tag{2.10}$$

which is illustrated in Figure 2.1. The constant ξ determines the mass of the σ meson. The potential of chiral symmetry, which will become part of the Lagrangian, is invariant under the transformations Λ_V and Λ_A. However, the ground state, $\sigma_0 = f_\pi$, breaks chiral symmetry. Excitations in the σ directions require a finite amount of energy, thus giving the σ a finite mass, whereas excitations in the pion direction (orthogonal to both axis shown in Figure 2.1) do not require energy and leaves the pions massless. The pion is, therefore, the Goldstone boson associated with the spontaneous breaking of chiral symmetry.

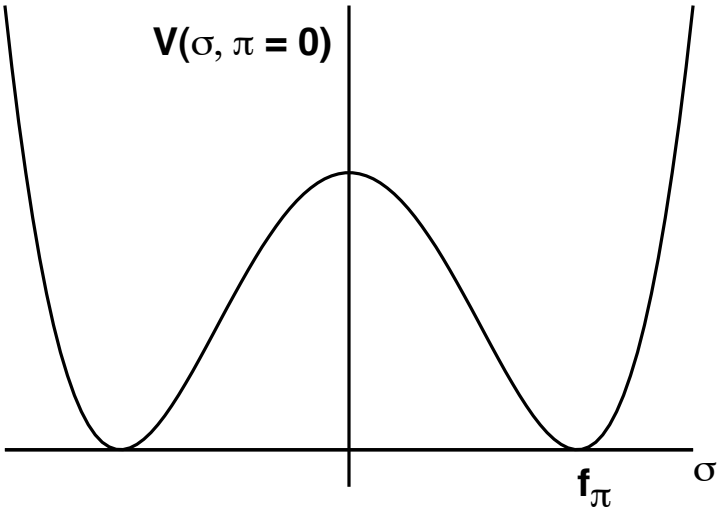

Figure 2.1: Potential of the linear sigma model.

However, chiral symmetry is only an approximate symmetry because it is explicitly broken by a term in the Lagrangian ignored so far,

$$\delta\mathcal{L} = \varepsilon\sigma. \tag{2.11}$$

Due to this small explicit breaking of chiral symmetry, pions acquire a finite mass, although it is small compared to that of other hadrons. The pion mass determines the symmetry breaking parameter ε. This small explicit breaking of chiral symmetry is also responsible for the the nonconservation of the axial vector current.

At high temperature and/or density the potential of chiral symmetry is predicted to change such that chiral symmetry is restored explicitly. Then, the ground state would be located at $\pi = 0$ and $\sigma = 0$. If the system cools off quickly, the potential of chiral symmetry from Eq. (2.10) can be recovered with the ground state remaining in its previous location. This state is, of course, instable and eventually chiral symmetry must be spontaneously broken again. When this occurs all directions along the pion fields and the scalar σ field are equally probable and the chosen direction might not coincide with the usual ground state. This disoriented state is referred to as disoriented chiral condensate (DCC) [133, 132]. As

chiral symmetry is also explicitly broken, the DCC is also instable and would eventually decay to return the chiral condensate to its usual ground state.

This decay of the DCC might then lead to measurable signatures. One proposed signature of the disoriented chiral condensate (DCC) are anomalous isospin fluctuations, which was discussed in the introduction to this chapter. To test the validity of this signature, alternative sources for such fluctuations are studied in the following by considering the influence of total isospin conservation, quantum symmetrization, and resonance decays.

2.2 Recursion Relations for Partition Functions

2.2.1 Nondegenerate Systems

When the number of available states is much larger than the number of particles, the probability for two or more particles occupying the same quantum state is small. In such a nondegenerate system, quantum statistics can be neglected. The partition function for a canonical ensemble of A particles conserving an additive quantum number or a vector of such quantities Q can be written as a product of single-particle partition functions

$$Z_{A,Q} = \sum_{\substack{\langle \sum \nu_k a_k = A \rangle \\ \langle \sum \nu_k q_k = Q \rangle}} \prod_{k=1}^{N} \frac{\omega_k^{\nu_k}}{\nu_k!}, \tag{2.12}$$

where N is the number of particle types, ν_k is the occupation number of particle type k, q_k is the charge of one particle, and the particle number a_k indicates how many times a particle contributes to the main conserved quantity A. For example, if A is the number of pions then $a_\rho = 2$, since the ρ meson decays predominantly into two pions. The single-particle partition function $\omega_k = g_k \sum_i \exp(-\varepsilon_i^{(k)}/T)$ sums Boltzmann factors weighted by the the spin degeneracy g_k over all available single-particle levels i.

Summation over the immense number of partitions in Eq. (2.12) can be avoided by

rewriting the partition function as a recursion relation [42, 55, 130],

$$Z_{A,Q} = \sum_{k=1}^{N} \frac{a_k \omega_k}{A} Z_{A-a_k,Q-q_k}. \tag{2.13}$$

If intermediate values of the partition function are stored, the computations required for Eq. (2.13) scale linearly in both A and N, thus making it possible to quickly calculate the canonical partition function numerically.

A partition function conserving total isospin as well as additive quantum numbers is derived by adding a sum over all possible isospin configurations for a given partition, $\{\nu_k\}$, and isospin weights $\xi\left(I,M|\{\nu_k\}\right)$ to Eq. (2.12),

$$\Omega_{A,I,M} = \sum_{\substack{\langle \sum \nu_j a_j = A \rangle \\ \langle \sum \nu_j q_j = Q \rangle}} \sum_{\{\nu_j\}} \xi\left(I,M|\{\nu_j\}\right) \prod_{j=1}^{N} \frac{\omega_j^{\nu_j}}{\nu_j!}. \tag{2.14}$$

To convert this partition function into a recursion relation insert $\frac{1}{A}\sum_{k=1}^{N} a_k \nu_k = 1$ into Eq. (2.14),

$$\Omega_{A,I,M} = \sum_{k=1}^{N} \frac{a_k \omega_k}{A} \sum_{\substack{\langle \sum \nu_j a_j = A \rangle \\ \langle \sum \nu_j q_j = Q \rangle}} \frac{\omega_k^{\nu_k - 1}}{(\nu_k - 1)!} \prod_{j \neq k} \frac{\omega_j^{\nu_j}}{\nu_j!} \sum_{\{\nu_j\}} \xi\left(I,M|\{\nu_j\}\right). \tag{2.15}$$

The entire system can be broken into two subsystems, a single particle with isospin I_k and projection m_k and a remainder system with isospin I' and projection $M - m_k$, which are coupled with the appropriate Clebsch-Gordan coefficients. All possible values for the total isospin of the remainder system have to be summed over,

$$\sum_{\{\nu_j\}} \xi\left(I,M|\{\nu_j\}\right) = \sum_{I'=|M-m_k|}^{I_k+I} \sum_{\{\nu'_j\}} \xi\left(I',M|\{\nu'_j\}\right) \langle I_k m_k; I', M-m_k | IM \rangle^2. \tag{2.16}$$

With this modification, the summation indexes in Eq. (2.15) can be switched,

$$\nu'_j = \begin{cases} \nu_j & , j \neq k \\ \nu_j - 1 & , j = k \end{cases} \tag{2.17}$$

and the partition function written as recursion relation

$$\Omega_{A,I,M} = \sum_{k=1}^{N} \frac{a_k \omega_k}{A} \sum_{I'=|I-I_k|}^{I+I_k} \Omega_{A-a_k,I',M-m_k} \langle I_k m_k; I', M-m_k | IM \rangle^2. \tag{2.18}$$

Since the partition function is the trace of an isoscalar, i.e. $e^{-H/T}$, it will not depend on the isospin projection M. Hence, Eq. (2.18) can be further simplified by summing the RHS over all isospin projections m_k of an isospin multiplet,

$$\Omega_{A,I} = \sum_{k'} \frac{a_k \omega_k}{A} \sum_{I'=|I-I_k|}^{I+I_k} \Omega_{A-a_k,I'}, \tag{2.19}$$

where the sum over k' includes isomultiplets, not individual particles species.

2.2.2 Degenerate Systems

Since several particles might occupy the same quantum state in a degenerate system, symmetrization of the wave function has to be accounted for. This discussion will be restricted to studying Bose-Einstein particles. States with multiple particles have to be added to Eq. (2.13), which only contains states that are occupied by zero or one particle,

$$Z_{A,M} = \sum_{n=1}^{\infty} \sum_{k=1}^{N} \frac{a_k}{A} C_n^{(k)} Z_{A-na_k,M-nm_k}, \tag{2.20}$$

where the cycle diagram is

$$C_n^{(k)} = \langle \tilde{\alpha} | e^{-H/T} | \alpha \rangle = \sum_l g_l \exp(-n\varepsilon_l^{(k)}/T). \tag{2.21}$$

Here, the state $|\alpha\rangle$ refers to an n-particle state of distinguishable particles and $|\tilde{\alpha}\rangle$ is the cyclic permutation of that state. The single-particle energy levels are $\varepsilon_l^{(k)}$ for particle type k. A more rigorous derivation of Eq. (2.20) is given in [129].

Since the partition function for conserved total isospin $\Omega_{A,I,M}$ is independent of the isospin projection M, as mentioned above, a simple relation can be derived, $Z_{A,M} = \sum_{I \geq M} \Omega_{A,I}$,

which in turn leads to

$$\Omega_{A,I} = Z_{A,M=I} - Z_{A,M=I+1}. \tag{2.22}$$

A second method for calculating the pion partition function constraining total isospin is obtained by evaluating the cycle diagram $C_n^{(k)}$ in Eq. (2.21) for its isospin content. These new cycle diagrams are defined as

$$\zeta_{n,i} \equiv \sum_{\beta} \langle \tilde{\beta}, n, i | e^{-H/T} | \beta, n, i \rangle, \tag{2.23}$$

where the sum over β represents a sum over all states with fixed particle number n and isospin i. The particles are assumed to be distinguishable and $\tilde{\beta}$ represents a cyclic permutation of particles. The partition function for the pions in term of this new cycle diagram is then

$$\Omega_{A,I} = \frac{1}{A} \sum_{n=1}^{A} \sum_{i=0}^{n} \sum_{I'=|I-i|}^{I+i} \zeta_{n,i} \Omega_{A-n,I'}, \tag{2.24}$$

where the new cycle diagrams ζ are yet to be determined. After obtaining a recursion relation for these functions from Eq. (2.24) itself,

$$\zeta_{A,I} = A\Omega_{A,I} - \sum_{n=1}^{A-1} \sum_{i=0}^{n} \sum_{I'=|I-i|}^{I+i} \zeta_{n,i} \Omega_{A-n,I'}, \tag{2.25}$$

these cycle diagrams are found to follow a simple pattern by considering a one-level system where $\Omega_{A,I}$ is easily calculated,

$$\zeta_{n,i} = \begin{cases} C_n, & i = n \\ -C_n, & i = n-1 \\ C_n, & i = 0 \\ 0, & \text{otherwise} \end{cases} \tag{2.26}$$

Since resonances are more massive and have lower phase space occupations, the probability of creating several resonances in the same state can be neglected except in the limit of extremely high densities. Therefore, resonances might be treated as independent, non-degenerate subsystems, for which a partition function can be obtained through Eq. (2.18).

The partition functions of two subsystems, 1 and 2, can then be convoluted to obtain that of the entire system,

$$\Omega_{A,I,M} = \sum_{A'=0}^{A} \sum_{I'=0}^{A'} \sum_{I''=|I-I'|}^{I+I'} \Omega^{(1)}_{A',I'} \Omega^{(2)}_{A-A',I''}. \tag{2.27}$$

If there are more than two subsystems Eq. (2.27) can be applied successively, i.e., partition functions of any two subsystems are convoluted first to obtain a new partition function, which is then convoluted with the partition function of another subsystem, and so on.

It should be pointed out that treating resonances as if they are in a different system is not consistent with the indistinguishability of pions from resonances and direct pions. For narrow resonances, the pions could be uniquely identified by constructing the invariant masses of the constituents. However, broad resonances cannot be identified confidently. The criteria for resonances being narrow are identical to the criteria that they have sufficiently long lifetime to decay outside the collision region. For all the calculations considered in this study, it is assumed that the resonances are separable. This assumption is excellent for pions from η mesons, good for pions from ω resonances and questionable for pions from ρ decays. Including the effects of symmetrizing the resonant and nonresonant pions remains an open question.

2.2.3 Monte Carlo Algorithm for Particle Production

The partition functions with exact quantum number and isospin conservation obtained in 2.2, can be applied in a Monte Carlo algorithm for particle generation. Recently, there has been much interest in modeling relativistic heavy ion collisions with hybrid models, in which early, dense stages of the collision are described by a hydrodynamical model before switching to a hadronic cascade to simulate the freeze-out stage [22]. The change of degrees of freedom at the interface between the two models from the energy-momentum tensor to hadrons is generally modeled by a grand-canonical ensemble, which conserves

charges only in the average over many events. However, event-by-event charge conservation is essential to calculating observables like fluctuations and balance functions, which have been proposed as possible signal for the quark-gluon plasma [24, 146].

Energy and momentum conservation is generally enforced with the Cooper-Frye formalism [49, 50], whereas the object of this algorithm is to generate an ensemble of particles with given quantum numbers Q and total isospin I. The following algorithm is shown to be consistent with partition functions derived in 2.2.1 for the nondegenerate case. The algorithm can be easily adjusted to generate Bose-Einstein particles with only additive quantum number conservation. An equivalent generation algorithm that conserves total isospin while accounting for Bose-Einstein symmetrization is difficult to derive because of negative contributions in Eq. (2.26) and is not attempted here.

An ensemble of particles with given quantum numbers Q and total isospin I can be generated by following these steps: In the first step, the total number of hadrons A has to be determined according to the probability for finding a certain hadron number in a grand-canonical ensemble

$$w_A = \frac{\Omega_{A,I,Q}}{\sum_{A=0}^{\infty} \Omega_{A,I,Q}}. \tag{2.28}$$

Particles are then generated one by one in an iterative process until the number of hadrons determined in the first step has been exhausted. In the second step, the particle type k to be generated is obtained according to their relative weights

$$w_k = \frac{1}{\Omega_{A,I,M,Q}} \frac{a_k \omega_k}{A} \sum_{I'=|M-m_k|}^{I+I_k} \langle I_k m_k; I', M-m_k | IM \rangle^2 \Omega_{A-a_k,I',M-m_k,Q-q_k}. \tag{2.29}$$

The total isospin of the system I and the isospin of the particle I_k can couple to more than one isospin of the remainder system I'. Therefore, in the third step, that isospin I' has to be

picked with the appropriate probability

$$w_{I'} = \frac{\langle I_k m_k; I', M-m_k | IM\rangle^2 \Omega_{A-a_k, I', M-m_k, Q-q_k}}{\sum_{I''=|M-m_k|}^{I+I_k} \langle I_k m_k; I'', M-m_k | IM\rangle^2 \Omega_{A-a_k, I'', M-m_k, Q-q_k}} \tag{2.30}$$

The last two steps are repeatedly iterated with the following substitutions

$$\begin{aligned} I &\rightarrow I' \\ M &\rightarrow M - m_k \\ A &\rightarrow A - a_k \end{aligned}$$

until the number of hadrons acquired in the first step has been generated, i.e. $A = 0$. Conservation laws are ascertained at every step of this algorithm because the probabilities Eqs. (2.28)–(2.30) would vanish for those configurations that violated the conservation laws, hence, no such configuration will be encountered.

2.3 Recursion Relations for Multiplicity Distributions and Isospin Fluctuations

2.3.1 Nondegenerate Systems

The multiplicity distribution can be calculated from a ratio of partition functions, where the numerator includes an extra constraint,

$$P_{A,M}(n_j) = \frac{Z_{A,M,n_j}}{Z_{A,M}}. \tag{2.31}$$

Here the numerator represents a canonical ensemble with the appropriate conservation laws containing n_j particles of type j. This additional constraint can be regarded as a "charge" and, therefore, is added to the indices of the partition function. The partition function in the numerator can be rewritten with the aid of Eq. (2.13),

$$Z_{A,M,n_j} = \sum_{k=1}^{N} \frac{a_k \omega_k}{A} Z_{A-a_k, M-m_k, n_j - d_{k,j}}, \tag{2.32}$$

where the feed-down factor $d_{k,j}$ indicates that a particle of type k decays into $d_{k,j}$ particles of type j. This approach, however, will not work for a resonance that decays via more than one decay channel. In such a case, a pseudo-particle is included for each decay branch with its degeneracy g_i scaled by the corresponding branching ratio.

It will prove more convenient to write equations in terms of the product of partition function and multiplicity distribution

$$W_{A,M}(n_j) \equiv Z_{A,M} P_{A,M}(n_j) \tag{2.33}$$

instead of the multiplicity distribution itself. For a nondegenerate system conserving only additive charges, the multiplicity distribution can be obtained from

$$W_{A,M}(n_j) = \sum_{k=1}^{N} \frac{a_k \omega_k}{A} W_{A-a_k,M-m_k}(n_j - d_{k,j}). \tag{2.34}$$

The occupation number for particle type j including feed-downs from resonance decays is determined by multiplying the occupation number of all particles, given in [130], by the feed-down-factor and summing over all resonances,

$$\langle n_j \rangle = \frac{1}{Z_{A,M}} \sum_{k=1}^{N} d_{k,j} \omega_k Z_{A-a_k,M-m_k}. \tag{2.35}$$

The second moment of the distribution will be needed for calculating isospin fluctuations as in Subsection 2.3.4,

$$\langle n_j n_{j'} \rangle = \sum_{k,k'=1}^{N} \frac{d_{k,j} d_{k',j'}}{Z_{A,M}} \left\{ \delta_{k,k'} \omega_k Z_{A-a_k,M-m_k} + \omega_k \omega_{k'} Z_{A-a_k-a_{k'},M-m_k-m_{k'}} \right\}. \tag{2.36}$$

The multiplicity distribution incorporating conserved total isospin can be derived in a similar manner as was employed for Eq. (2.18),

$$W_{A,I,M}(n_j) = \sum_{k=1}^{N} \frac{a_k \omega_k}{A} \sum_{I'} \langle I_k m_k; I', M - m_k | IM \rangle^2 W_{A-a_k,I',M-m_k}(n_j - d_{k,j}). \tag{2.37}$$

2.3.2 Degenerate Systems

When considering only quantum numbers corresponding to additive charges, the multiplicity distribution is obtained through Eqs. (2.20) and (2.31) and

$$W_{A,M}(n_j) = \sum_{k=1}^{N} \frac{a_k}{A} \sum_{l=1}^{\infty} C_l^{(k)} W_{A-la_j,M-lm_j}(n_j - ld_{k,j}), \tag{2.38}$$

where C_l is the cycle diagram defined in Eq. (2.21). Calculating the two-point function and the four-point functions permits the derivation of the first two moments of the multiplicity distribution. The 2-point function is

$$\langle a_i^\dagger a_j \rangle = \frac{\delta_{ij}}{Z_{A,M}} \sum_n \exp(-n\varepsilon_i/T) Z_{A-na_i,M-nm_i}. \tag{2.39}$$

Summing over all particle types and states and multiplying by feed-down factors results in an expression for the occupation numbers,

$$\langle n_j \rangle = \frac{1}{Z_{A,M}} \sum_{k=1}^{N} d_{k,j} \sum_{l=1}^{\infty} C_l^{(k)} Z_{A-la_k,M-lm_k}. \tag{2.40}$$

Similarly, the 4-point function

$$\begin{aligned} \langle a_i^\dagger a_j^\dagger a_k a_l \rangle &= \frac{\delta_{il}\delta_{jk} + \delta_{ik}\delta_{jl}}{Z_{A,M}} \\ &\quad \times \sum_{n_i,n_j} \exp(-n_i\varepsilon_i/T) \exp(-n_j\varepsilon_j/T) Z_{A-n_ia_i-n_ja_j,M-n_im_i-n_jm_j} \end{aligned} \tag{2.41}$$

serves to obtain second moments of the multiplicity distribution

$$\langle n_j n_{j'} \rangle = \frac{\delta_{j,j'}}{Z_{A,M}} \sum_{l,l'} C_{l+l'} Z_{A-(l+l')a_j,M-(l+l')m_j} \tag{2.42}$$

$$+ \frac{1}{Z_{A,M}} \left\{ \sum_l \delta_{j,j'} C_l Z_{A-la_k,M-lm_k} + \sum_{l,l'} C_l C_{l'} Z_{A-la_k-l'a_{k'},M-lm_k-l'm_{k'}} \right\}.$$

Neglecting the terms with C_ℓ where $\ell > 1$, leads back to the nondegenerate result, Eq. (2.36).

Calculating the multiplicity distribution for degenerate systems with the constraint of total isospin conservation becomes difficult because the analog of the cycle diagram, $C_n^{(k)}$

in Eq. (2.38), needs to be analyzed for isospin i and charge n_j. Such a cycle diagram with a particles and isospin projection m can be written as

$$\chi_{a,i,m}(n_j) \equiv \sum_{\alpha,\beta} \langle \tilde{\alpha}, a, i, m | e^{-H/T} | \beta, a, n_j, m \rangle \langle \beta, a, n_j, m | \alpha, a, i, m \rangle, \tag{2.43}$$

where the sums over α and β correspond to sums over all states with fixed (a,i,m) and (a,n_j,m), respectively, and $\tilde{\alpha}$ represents a cyclic permutation of particles, which are assumed to be distinguishable.

The multiplicity distribution can be calculated in terms of these cycle diagrams

$$W_{A,I,M}(n_j) = \frac{1}{A} \sum_{a,i,m,n'_j,I'} \chi_{a,i,m}(n'_j) W_{A-a,I',M-m}(n_j - n'_j) \langle I', M-m; i, m | I, M \rangle^2. \tag{2.44}$$

The general cycle diagram accounting for all energy levels, $\chi_{a,i,m}(n'_j)$, can be derived in terms of cycle diagrams for a single-level system, $\chi^{(1)}$,

$$\chi_{a,i,m,n_k} = \chi^{(1)}_{a,i,m,n_k} \sum_{\ell} g_\ell \exp\left(-aE_\ell/T\right), \tag{2.45}$$

where ℓ indicates the single-particle energy levels with energy E_ℓ. Applying, Eq. (2.44) to a single-level system leads to a recursion relation for $\chi^{(1)}$

$$\begin{aligned} \chi^{(1)}_{A,I,M}(n_j) &= A W^{(1)}_{A,I,M}(n_j) \\ &- \sum_{a<A,i,m,n_j,I'} \chi^{(1)}_{a,i,m}(n_j) W^{(1)}_{A-a,I',M-m}(n_j - n_j) \langle I', M-m; i, m | I, M \rangle^2, \end{aligned} \tag{2.46}$$

where the distribution $W^{(1)}_{a,i,m}(n_j)$ will be derived in the next subsection.

If other particles, like resonances, are to be included in the ensemble, one can either insert a sum over species into Eq. (2.44); or calculate W separately for each species and convolute them to find W for the entire system,

$$W_{A,I,M}(n_j) = \sum_{A',I',M',n'_j,I''} W^{(1)}_{A',I',M'}(n'_j) W^{(2)}_{A-A',I'',M-M'}(n_j - n'_j) \langle I'M'; I'', M-M' | IM \rangle^2. \tag{2.47}$$

In these calculations, W was calculated separately for resonances neglecting symmetrization and then convoluted with W calculated for pions with proper symmetrization.

2.3.3 Single-level Multiplicity Distribution Conserving Total Isospin

By definition, the distribution $W^{(1)}_{a,i,m}(n_j)$, needed in Eq. (2.46), can be written as the product of the partition function and the multiplicity distribution,

$$W^{(1)}_{a,i,m,n_j} = \omega^{(1)}_{a,i,m} p^{(1)}_{a,i,m}(n_j), \tag{2.48}$$

where the partition function for a particles in a single level with energy E is

$$\omega^{(1)}_{a,i,m} = \begin{cases} \exp(-aE/T) & ,\text{if } a+i \text{ even} \\ 0 & ,\text{if } a+i \text{ odd.} \end{cases} \tag{2.49}$$

$p^{(1)}_{a,i,m}(n_j)$ is the probability of observing n_j pions in a single-state system that contains a total of a pions with total isospin i and projection m. This probability distribution has to be calculated for only one type of pions because the pion occupation numbers are related through

$$m = n_+ - n_-, \tag{2.50}$$

$$a = n_0 + n_+ + n_-. \tag{2.51}$$

In the following, probability distributions will be derived for positive pions. The isospin wave function of the system can be written in terms of eigenstates of the number operators

$$|a,i,m\rangle = \sum_{n_+=m}^{(a+m)/2} \alpha_{a,i,m,n_+} |n_0\rangle |n_+\rangle |n_-\rangle, \tag{2.52}$$

where $n_0 = a+m-2n_+$ and $n_- = n_+ - m$. The coefficients in Eq. (2.52) are related to the probability distribution by

$$p^{(1)}_{a,i,m}(n_+) = (\alpha_{a,i,m,n_+})^2. \tag{2.53}$$

The isospin wave function $|a,a,a\rangle$ can only be constructed if all pions in the state are positive, i.e., $n_+ = a$, therefore

$$\alpha_{a,a,a,n_+} = \begin{cases} 1 & ,\text{if } n_+ = a \\ 0 & ,\text{otherwise.} \end{cases} \tag{2.54}$$

Leaving the pion number a and isospin $i = a$ fixed, the isospin lowering operator can be applied $I_- = \sqrt{2}(\pi_-^\dagger \pi_0 + \pi_0^\dagger \pi_+)$ to reach lower values of m,

$$I_-|a,i,m\rangle = \sqrt{i(i+1) - m(m-1)}|a,i,m-1\rangle. \tag{2.55}$$

The LHS of Eq. (2.55) expands to

$$\begin{aligned} & I_- \sum_{n_+} \alpha_{a,a,m,n_+} |a+m-2n_+\rangle |n_+\rangle |n_+ - m\rangle = \\ & \sqrt{2} \sum_{n_+=m}^{(a+m)/2} \sqrt{a+m-2n_+}\sqrt{n_+ - m + 1}\,\alpha_{a,a,m,n_+} |a+(m-1)-2n_+\rangle |n_+\rangle |n_+ - (m-1)\rangle \\ & + \sqrt{2} \sum_{n_+=m-1}^{(a+m)/2-1} \sqrt{a+(m-1)-2n_+}\sqrt{n_+ + 1}\,\alpha_{a,a,m,n_+ +1} \\ & \qquad \times |a+(m-1)-2n_+\rangle |n_+\rangle |n_+ - (m-1)\rangle. \end{aligned} \tag{2.56}$$

When the coefficients on the LHS are match with those on the RHS of Eq. (2.55) a recursion relation is obtained,

$$\begin{aligned} \alpha_{a,a,m-1,n_+} = \sqrt{\frac{2}{i(i+1)-m(m-1)}} \quad & \Big\{ \sqrt{(a+m-2n_+)(n_+ - m + 1)}\,\alpha_{a,a,m,n_+} \\ & + \sqrt{(a+m-1-2n_+)(n_+ + 1)}\,\alpha_{a,a,m,n_+ +1} \Big\}. \end{aligned} \tag{2.57}$$

So far, only the coefficients α_{a,i,m,n_+} for $a = i$ were found. With the help of the isoscalar operator

$$U_2 = 2\pi_+^\dagger \pi_-^\dagger - \pi_-^\dagger \pi_-^\dagger \tag{2.58}$$

that creates two pions without altering the isospin, higher values of a can be reached,

$$U_2|a,i,m\rangle = N_{a,i}|a+2,i,m\rangle, \tag{2.59}$$

where the normalization constant is

$$N_{a,i} = \sqrt{(a+2)(a+3) - i(i+1)}. \tag{2.60}$$

Matching the coefficients on both sides of Eq. (2.59) to each other leads to

$$\alpha_{a+2,i,m,n_+} = \frac{1}{N}\Big\{2\sqrt{n_+(n_+-m)}\alpha_{a,i,m,n_+-1} - \sqrt{(a+m-1-2n_+)(a+m-2-2n_+)}\alpha_{a,i,m,n_+}\Big\}. \quad (2.61)$$

In case, $a+i$ is odd, no combination of pions yields the isospin wave function $|a,i,m\rangle$, as is evident from Eq. (2.49). Therefore

$$\alpha_{a,i,m,n_+} = 0 \quad , \text{ if } a+i \text{ odd.} \quad (2.62)$$

Equations (2.54), (2.57), (2.61), and (2.62) completely determine the coefficients α_{a,i,m,n_+}, which in turn define the probability distributions $p^{(1)}_{a,i,m}(n_+)$ and, therefore, the single-level partition functions $W^{(1)}_{a,i,m,n_j}$.

If some states $l_1, l_2, \cdots, l_g$ have degenerate energies, the amount of computations can be reduced by including only one energy state l with a g-fold degeneracy. The partition function for such a degenerate state is obtained by successively convoluting the partition functions of states $l_1, l_2, \cdots, l_g$ with the aid of Eq. (2.27).

2.3.4 Isospin Fluctuations

Given some system with quantum states α, pion isospin fluctuations can be defined as

$$G^2 = \sum_\alpha \langle \alpha | (N_+ + N_- - 2N_0)^2 | \alpha \rangle, \quad (2.63)$$

where N_+, N_- and N_0 are the number operators of the respective pions. These isospin fluctuations could be computed through multiplicity distributions or with the expressions for densities and higher moments that were given above. However, when total isospin should be conserved as well, multiplicity distribution calculations are slow and expressions for densities and higher moments are difficult to derive. Instead, the isospin fluctuations will be derived for a system in an isosinglet in terms of isospin projection states.

The operator in Eq. (2.63) is a product of two rank-2 spherical tensors components

$$(N_+ + N_- - 2N_0)^2 = 6T_{20}T_{20}, \tag{2.64}$$

where

$$T_{20} = \sum_i \frac{1}{\sqrt{6}} \left(\pi^\dagger_{+,i}\pi_{+,i} + \pi^\dagger_{-,i}\pi_{-,i} - 2\pi^\dagger_{0,i}\pi_{0,i} \right), \tag{2.65a}$$

$$T_{2\pm1} = \sum_i \frac{1}{\sqrt{2}} \left(\pi^\dagger_{0,i}\pi_{\mp,i} - \pi^\dagger_{\pm,i}\pi_{0,i} \right), \tag{2.65b}$$

$$T_{2\pm2} = \sum_i \pi^\dagger_{\pm,i}\pi_{\mp,i}. \tag{2.65c}$$

A product of spherical tensors can be decomposed into other spherical tensor components

$$T_{20}T_{20} = \sum_{J,M} \langle 20;20|JM\rangle A_{JM}. \tag{2.66}$$

By the Wigner-Eckart theorem only A_{00} contributes when contracted between isosinglet states, and because A_{00} is an isoscalar one can write

$$\langle G^2 \rangle = \frac{6}{\sqrt{5}} \sum_{I=0} \langle A_{00} \rangle = \frac{6}{\sqrt{5}} \left(\sum_{M=0} - \sum_{M=1} \right) \langle M|A_{00}|M\rangle. \tag{2.67}$$

Some algebra leads to

$$A_{00} = \sum_M \langle 2M;2,-M|00\rangle T_{2M}T_{2,-M} = A'_{00} + A^{\mathrm{QM}}_{00}, \tag{2.68}$$

where

$$A'_{00} = \frac{1}{\sqrt{5}} \left[\frac{3}{2}N_+ + \frac{3}{2}N_- + N_0 + \frac{1}{6}(N_+ + N_- - 2N_0)^2 \right] \tag{2.69}$$

and

$$A^{\mathrm{QM}}_{00} = \frac{1}{\sqrt{5}} \sum_{i,j} \left(2\pi^\dagger_{+,i}\pi^\dagger_{-,j}\pi_{+,j}\pi_{-,i} + \pi^\dagger_{+,i}\pi^\dagger_{0,j}\pi_{+,j}\pi_{0,i} + \pi^\dagger_{0,i}\pi^\dagger_{-,j}\pi_{0,j}\pi_{-,i} \right). \tag{2.70}$$

The expectation of A^{QM}_{00} is nonzero when particles of different charges are in the same quantum state, or when two differently charged pions are produced into two different states

with a quantum correlation arising from a resonance decay. The contribution to $A_{00}^{\rm QM}$ from the degenerate nature of the pion states can be determined via Eq. (2.41),

$$\langle \pi^\dagger_{k,i}\pi^\dagger_{k',j}\pi_{k,j}\pi_{k',i}\rangle = \frac{1}{Z_{A,M}}\sum_{l,l'} C^{(\pi)}_{l+l'} Z_{A-la_k-l'a_{k'},M-lm_k-l'm_{k'}}. \tag{2.71}$$

This contribution can be ignored in the nondegenerate limit, where occupation numbers are small.

Contributions to $A_{00}^{\rm QM}$ from the coherent correlation between pions from resonant decays can be found by expressing the resonances in terms of pion creation operators. For example, the ρ^+ meson, which is a member of an isotriplet, can be considered as one pion in an *s* wave and a second pion in a *p* state. Referring to these two states as *i* and *j*,

$$|\rho^+\rangle = \frac{1}{\sqrt{2}}\left(\pi^\dagger_{+,i}\pi^\dagger_{0,j} - \pi^\dagger_{+,j}\pi^\dagger_{0,i}\right)|0\rangle. \tag{2.72}$$

How the states *i* and *j* are chosen is irrelevant since they are summed over in Eq. (2.70), but the coherent mixture of the two permutations, which is necessary for the ρ^+ to be a member of an isotriplet, results in a nonzero contribution to $A_{00}^{\rm QM}$,

$$\langle A_{00}^{\rm QM}\rangle = -\frac{1}{\sqrt{5}}\left(2N_{\rho^0} + N_{\rho^+} + N_{\rho^-}\right). \tag{2.73}$$

The ω and η mesons are isosinglets and can be treated accordingly. For instance,

$$|\eta\rangle = \frac{1}{\sqrt{6}}\sum_{i,j,k}\varepsilon_{ijk}\pi^\dagger_{+,i}\pi^\dagger_{-,j}\pi^\dagger_{0,k}|0\rangle, \tag{2.74}$$

which adds another term to $A_{00}^{\rm QM}$,

$$\langle A_{00}^{\rm QM}\rangle = -\frac{4}{\sqrt{5}}\left(N_\omega + N_\eta\right). \tag{2.75}$$

2.4 Numerical Results and Comparisons

In heavy-ion reactions, and perhaps in *pp* reactions, pions reinteract with other pions in their neighborhood, or domain, and might be expected to sample a large portion of the

available phase space. As isospin should be conserved in each domain, it seems reasonable to explore distributions for a few dozen pions rather than creating an ensemble of a few thousand pions, which could be treated as a grand canonical ensemble [71]. One of the study's goals is to understand how many pions are required for conservation constraints to become irrelevant.

In the following, symmetrization and resonances are first ignored in order to focus on the effects of conserving isospin, subsequently, the effects of symmetrization and resonances are illustrated by considering a simple example.

2.4.1 Total Isospin Conservation

When quantum degeneracy and resonances are ignored, isospin distributions are independent of energy levels or temperature. Therefore, the results presented in the following are generic to any system where only pions are considered and the phase space occupation numbers are small. A random distribution ignoring isospin conservation, i.e. a mixed-event construction, will serve as a benchmark.

$$P_{\text{random}}(n_0) = \left(\frac{1}{3}\right)^N \sum_{n_+ + n_- + n_0 = N} \frac{N!}{n_+!n_-!n_0!} \tag{2.76}$$

Unlike distributions that conserve isospin, this distribution allows both even and odd numbers of neutral pions and is, therefore, scaled by a factor of two to compare the width with that of the other distributions. Secondly, when pion creation is constrained to isoscalar pairs, as in [128], the distribution can be considered as a binomial distribution of pairs where one third of the time the pair is comprised of two neutral pions and two thirds of the time the pair is comprised of a positive and negative pion.

$$P_{\text{pairwise}}(n_0) = \left(\frac{1}{3}\right)^{n_0/2} \left(\frac{2}{3}\right)^{(N-n_0)/2} \frac{(N/2)!}{(n_0/2)!(N/2-n_0/2)!} \tag{2.77}$$

This pairwise distribution is broader than the random distribution by a factor of $\sqrt{2}$, as can be seen in Figure 2.2.

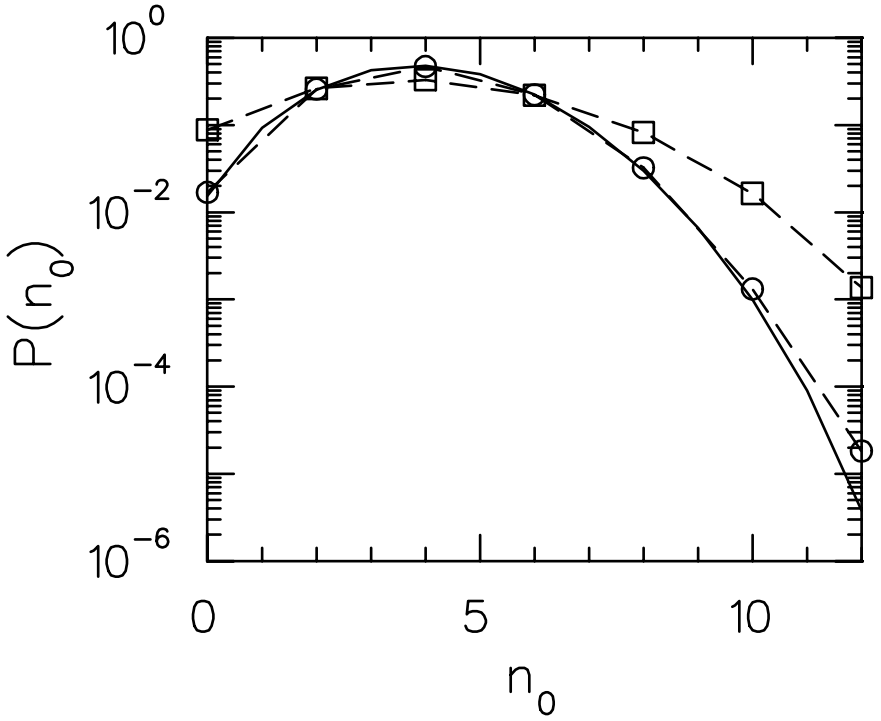

Figure 2.2: The probability of observing n_0 neutral pions is shown for a system of 12 pions. Symmetrization and resonances are neglected. A random distribution, multiplied by 2 for comparison, is represented by a solid line and is used as a benchmark. A distribution resulting from isoscalar pairs of pions (squares) is significantly broader, whereas a distribution including all isosinglets (circles) approaches the random distribution.

Finally, the isospin distribution for nondegenerate particles is calculated with the methods of Subsection 2.3.1 with all 12-pion isosinglet states being considered. The constraint of exact isospin conservation only modestly broadens the distribution relative to the random distribution as shown in Figure 2.2.

These findings are underscored by comparing the isospin fluctuations as a function of total pion number, as shown in Figure 2.3. When pion emission is constrained to isoscalar pairs, fluctuations are twice as large as compared to the random case for all system sizes. When considering all N-pion isosinglets fluctuations are larger by a factor which falls from two to unity as N approaches infinity.

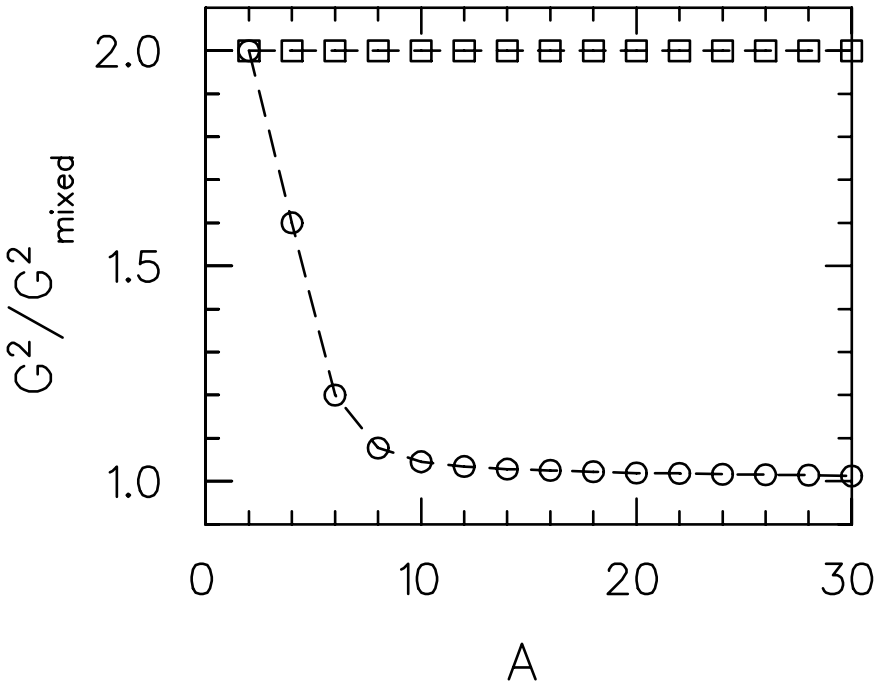

Figure 2.3: The fluctuation G^2 for nondegenerate systems as a function of system size for an ensemble of isoscalar pairs (squares) and one including all isosinglet states (circles). The fluctuations have been normalized by the fluctuation for a random system. The fluctuations for the pairwise distribution are twice the fluctuations for a random distribution, whereas including all isosinglet states relaxes the constraint and results in the same width as the random distributions for large systems.

2.4.2 Including Symmetrization and Resonances

To illustrate the effects of Bose-Einstein symmetrization, total isospin conservation, and resonance decays, an assumption must be made about the available single-particle energy levels that are summed over in the single-particle partition function. Assuming the model system is confined to a cube of volume V, the energy states are obtained

$$\varepsilon_{n,m,l} = \sqrt{\frac{\pi^2}{R^2}(n^2+m^2+l^2)+M^2}, \tag{2.78}$$

where $R = V^{1/3}$, M is the mass of the particle, and n,m,l are chosen to be half-integers. The choice of half integers, instead of the more usual integers, de-emphasizes zero-point surface energy effects and seems more physical if the confinement to the volume does not arise from an infinite potential well. This becomes important when systems are confined to

a small volume.

Isospin distributions were calculated for a system of 24 pions at two densities, 0.3 fm^{-3}, which is well above breakup densities for hadronic collisions, and 0.1 fm^{-3}. The temperature was chosen to be 125 MeV. The Bose-Einstein nature of pions was taken into account when calculating multiplicities according to the formalism from Subsection 2.3.2. The multiplicity distributions were then convoluted with those of three resonant states, the isotriplet ρ mesons and the isosinglet ω and η mesons, which were treated as nondegenerate systems according to Subsection 2.3.1.

As expected, the isospin distributions for symmetrized pions in an isosinglet are broader than the random distribution when resonances are neglected, as shown in Figure 2.4. This broadening is especially pronounced at high density. However, the inclusion of resonances more than compensates for the symmetrization effects and results in distributions that are narrower than the random distribution. Figure 2.5 displays fluctuations as a function of density for the 24-pion system. The dramatic broadening induced by symmetrization at high density is counteracted by a remarkable narrowing when resonant states are considered.

The conditions for pions to prefer forming a resonance are similar to the conditions for symmetrization to be important, i.e., a high phase space density. At low temperature, where the mass penalty for resonant formation would play a larger role, resonant effects would become relatively less important than symmetrization. However, for the temperature of 125 MeV considered here, the resonant effects overwhelm the effects of symmetrization at all densities.

The presented calculations with only three included meson resonance are largely schematic, a more realistic calculation requires more resonances like strange mesons and baryonic resonances, which need to be added along with strangeness and baryon number conservation. The formalism scales linearly with the number of particle species if the resonances were to

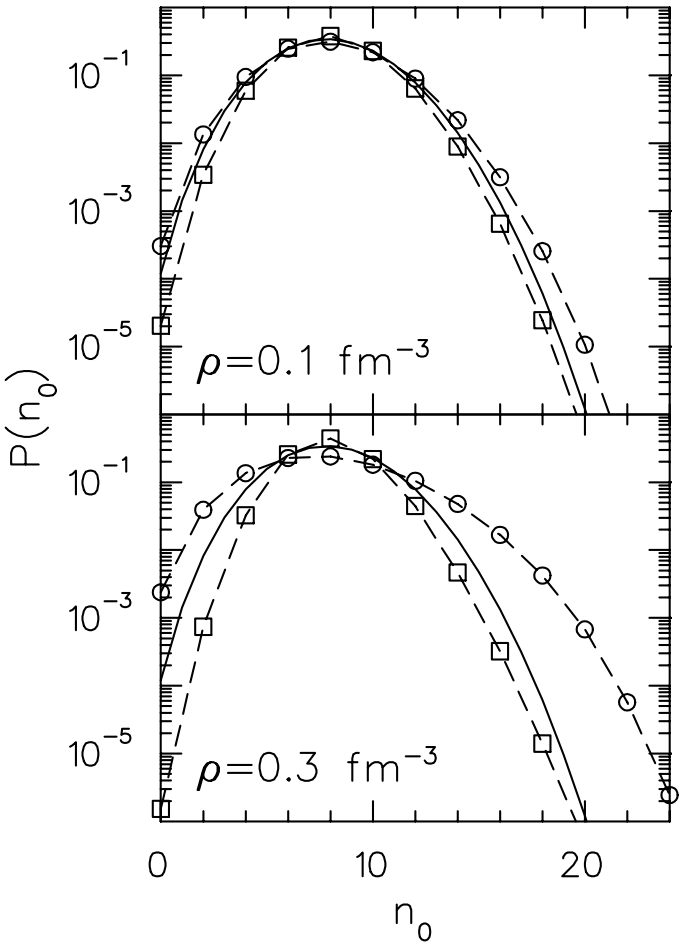

Figure 2.4: The probability for producing n_0 neutral pions in a system of $A = 24$ pions at $T = 125$ MeV is shown for ensembles restricted to an overall isosinglet and with symmetrization included. Calculations with resonances (squares) and without (circles) are displayed. Although symmetrization broadens the distribution relative to the random distribution (solid line), the inclusion of resonances results in a narrower distribution as compared to the random distribution.

be included without additional conserved charges. Theoretically, any amount of quantum numbers can be conserved as long as they commute with the isospin operator. Practically, every new index, which has to be added to the partition function and multiplicity distributions, to conserve another charge increments the number of loops by one. The increase in run-time has little consequence for calculations of partition functions and direct calculations of isospin fluctuations, which are virtually instantaneous, whereas any additional index would significantly slow down calculations of multiplicity distributions, which take

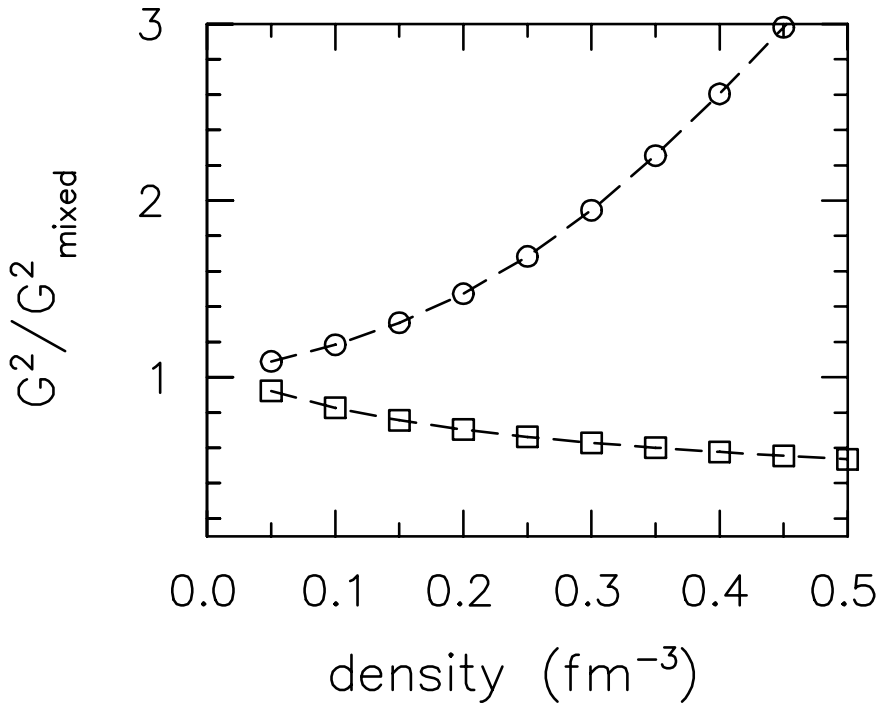

Figure 2.5: Isospin fluctuations, or squared width of the isospin distributions, as a function of density scaled by the width of a random distribution. Calculations with resonances (squares) and without (circles) are displayed. Calculations were performed for 24 pions restricted to isosinglet states at a temperature of 125 MeV. At high density, the distributions are broadened by including symmetrization and narrowed by including resonances produces.

on the order of one minute.

The aforementioned caveats are not expected to become major obstacles in the application of the presented formalism. Although the particle multiplicities are high, in the thousands, in possible physical applications like relativistic heavy ion collisions, the local nature of charge conservation would limit the number of particles considered at any given time. The system under consideration would have to be broken into domains, in which the charges are conserved locally, then calculations proceed one domain at a time. Each domain would have a relatively small number of particles with which to cope.

Also, the limitations of any comparison with experiment should be considered before tackling the more numerically challenging problem of including strangeness and baryon

number. It is difficult to detect neutral pions since each neutral pion decays into two photons. Furthermore, the ability to identify neutrons and kaons, especially those kaons which then decay into pions, should be considered. Given the inherent complexity of any such measurement, it seems proper to stop short of performing more complicated calculations without a commensurate consideration of the measurement. Nonetheless, several valuable lessons can be gained from the schematic calculations presented here.

Finally, it should be noted that the isospin fluctuation G^2 was calculated both from the distributions themselves and from the methods described in Subsection 2.3.4. Although the two sets of numerical calculations have little in common aside from the functions used to generate the single-particle levels, the two sets of moments agreed with each other within the numerical accuracy of the computer.

Chapter 3

The Microscopic Evolution Model Gromit

The transient quark-gluon plasma (QGP) is not accessible by direct experiments due to its short lifetime, which is on the order of 10^{-23} s, and its small size, which is on the order of 10^{-14} m. However, direct measurements may not be necessary to answer the most important question at hand. Did the QGP actually exist during some stage of the collision? The existence of the QGP must be established from the information contained in the collision debris recorded by the detectors. An observable that would indicate the presence of a QGP during the collision is usually referred to as a signal of the QGP. Theoretical work on this topic has been marred by the complexity of the underlying theory of QCD and by the large number of produced particles. Typically, around 6000 particles are created in a gold-on-gold collision at the Relativistic Heavy Ion Collider (RHIC).

After research on analytical theories failed to produce firm theoretical predictions for a signal of the QGP, the focus shifted toward numerical modeling of relativistic heavy-ion collisions. The application of such models has proven to be indispensable, particularly for the design of experiments, the analysis of data, and the extraction of detailed predictions. The nature of these models can be statistical, phenomenological, semi-classical, classical, or inspired by field theories. Even a classical description of relativistic heavy-ion collisions

can be justified, given that the thermal wavelength of the system is small compared to the size of the system. Unfortunately, the proposed QGP signals are generally model dependent in the sense can that an observable proposed by one model to be signal of the QGP can often be explained through other mechanisms by one or more other models. These discrepancies stem from the incompatibility of basic assumptions in the different models, which make it difficult, if not impossible, to compare one model to another. Hence, in addition to the search for model-independent signals much effort is spent on identifying the model components that are responsible for the diverging predictions on observables. The different components of currently available models are difficult to study in isolation, since the implementations of the models are generally supplied "as is" with little room for adjustments. In addition, questionable components often cannot be switched off to examine their influence.

In the following, a new modular framework for microscopic transport models based on the BTE, Gromit, is introduced after a brief review of its theoretical foundation. Gromit is developed and written within the RHIC Transport Theory Collaboration (RTTC) in the hope of moving beyond the limitations of current microscopic models. It provides a general framework that could be used for any degrees of freedom and any interaction; it is expandable, modular, transparent, and easy to debug and maintain. The reason for choosing microscopic transport models was their capability of describing nonequilibrium dynamics, which hydrodynamical models fail to describe due to their assumption of local statistical equilibrium [85, 109].

3.1 Transport Equations

Transport theory has a long history dating back to the works of Boltzmann and Maxwell on the kinetic theory of gases in the 1870's. Over time, the original Boltzmann equation has

been modified to incorporate new physical insights like relativity, quantum statistics, and the nuclear mean field.

The classical relativistic Boltzmann transport equation (BTE) describes the evolution of the single-particle distribution $f(x,p)$ in phase space with spacetime coordinate x and momentum coordinate p.

$$p^\mu \partial_\mu f(x,p) = C(x,p), \tag{3.1}$$

where $C(x,p)$ is the Lorentz-invariant collision term

$$C(x,p) = \frac{1}{2}\int \frac{d^3p_1}{p_1^0}\frac{d^3p_1'}{p_1'^0}\frac{d^3p'}{p'^0}\left[f'f_1'W(p',p_1'|p,p_1) - ff_1W(p,p_1|p',p_1')\right], \tag{3.2}$$

with $f_1 = f(x,p_1)$, $f' = f(x,p')$, and $f_1' = f(x,p_1')$. The transition probability W is defined in term of the scattering matrix T as

$$W(p,p_1|p',p_1') = \delta^{(4)}(p+p_1-p'-p_1')|\langle p',p_1'|T|p,p_1\rangle|^2. \tag{3.3}$$

In Eq. (3.2) Boltzmann's *Stoßzahlansatz*, or "assumption of molecular chaos" is used to derive that the number of binary collisions is proportional to the products of phase space densities. The collision term also assumes that interaction are local since all phase space densities in Eq. (3.2) are evaluated at the same spacetime point x.

Uehling and Uhlenbeck modified the transition probability W in the BTE to account for identical particle statistics [149, 148].

$$p^\mu \partial_\mu f(x,p) = \frac{1}{2}\int \frac{d^3p_1}{p_1^0}\frac{d^3p_1'}{p_1'^0}\frac{d^3p'}{p'^0}\left[f'f_1'(1\pm f_1)(1\pm f)\tilde{W}(p',p_1'|p,p_1) - ff_1(1\pm f')(1\pm f_1')\tilde{W}(p,p_1|p',p_1')\right], \tag{3.4}$$

where the negative sign is used for fermions and the positive sign for bosons. The modification in the Boltzmann-Uehling-Uhlenbeck (BUU) equation becomes important only at high phase space densities, which are found for fermions in low-energy heavy ion collisions due to the limited available phase space.

The BTE was further modified by Vlasov, who added a force term to the nonrelativistic form of Eq. (3.1) to account for the nuclear interactions.

$$\left(\frac{\partial}{\partial t}+\mathbf{v}\cdot\nabla_r-\frac{1}{m}(\nabla_r U)\cdot\nabla_p\right)f(x,p)=C(x,p), \tag{3.5}$$

where U an external potential, which is often approximated by a mean field. In the Vlasov equation, interactions between particles are considered to arise from two distinct sources, from the external potential (or mean field) and from cross sections.

3.1.1 Monte Carlo Solution

The BTE, Eq. (3.1), due to its nonlinear nature, cannot be solved exactly by either analytical or numerical methods, except for grossly over-simplified situations. The common approach is, therefore, to get an approximate solution of Eq. (3.1) from a Monte Carlo simulation. Often, the quantity of primary interest is not the phase space density, $f(x,p)$, itself but an observable that is a function of the phase space density $O(f(x,p))$. The following steps are carried out to determine any observable, including $f(x,p)$ itself. First, the phase space density is sampled at randomly chosen points, such that the density of sampling points corresponds to the phase space density. Then, the observable is calculated from this sampled phase space density and, finally, averaged over a large number of samples to obtain an approximation for the observable.

This procedure has rather strong analogies to the experimental determination of many observables. Each sample in the Monte Carlo scheme is can be interpreted as one physical event. The sampling points correspond to the physical particles. In experiments, like in the Monte Carlo simulation, the observable is often calculated from each event and then averaged over all events. For convenience, the analogous physical terms, particles, events, and observable, will be used, when referring to the Monte Carlo technique.

However, not all observables can be determined in the fashion mentioned above. For

example, multi-particle correlations, are destroyed by the assumption of molecular chaos, which introduced the one-particle phase space density into the BTE, and cannot be determined from Boltzmann-type models. Another class of observables, fluctuations, are lost in the Monte Carlo approach, as observables are averaged and smoothed out. However, the technique can be adjusted to simulate fluctuations [31].

The time evolution of the phase space density can be modeled by moving the particles on trajectories consistent with the mean field, if one is present, between points of interaction. Collisions are determined to sample the transition probability from the transport equation by prescribing that two particles interact if they get within a certain distance of each other. This interaction range is determined from the cross section

$$r = \sqrt{\frac{\sigma}{\pi}}. \tag{3.6}$$

In an elastic interaction, particles merely change their momenta, whereas in inelastic collisions particles from the incoming channel are replaced by other particles.

3.1.2 Scaling Properties of the Boltzmann Equation

The momentum change described in the previous subsection is generally executed instantaneously. In most cases information about a particle's existence is transferred to another with infinite speed as the particles are likely to be separated by a finite distance

$$d \leq \sqrt{\frac{\sigma}{\pi}}. \tag{3.7}$$

This breaks special relativity and leads to a wide range of complications, fundamental problems like the violation of causality [103] as well as practical problems with collision prescriptions like those that will be discussed in Subsection 3.2.5. However, the impact of these violations can be minimized by taking advantage of a scaling property of the Boltzmann Equation, which remains invariant under simultaneous transformation of transition

probability and phase space density [157, 32, 161]

$$W \longrightarrow W' = \frac{W}{\lambda}, \tag{3.8}$$

$$f \longrightarrow f' = \lambda f. \tag{3.9}$$

The scaling factor, or sampling factor, λ could be any positive real number. However the sampling factor is usually constrained to be integer so that the the scaling of the phase space density can then be implemented by multiplying the number of particles by λ. The most common way to implement the scaling of the transition probability is through reducing the cross section by a factor λ. This transformation leaves the mean free path, $l = 1/n\sigma$, and the scattering rate constant, thus preserving the thermodynamic properties of the system. The interaction range from Eq. (3.6) vanishes in the Boltzmann limit, $\lambda \to \infty$, leading to entirely local interactions. This restores Lorentz covariance and causality and removes the problems that come along with their violation. Examples of these effects will be discussed in Chapters 4.

Yet, there is a potential caveat to the preceding approach. Although the covariance problems can be solved by choosing a large sampling factor λ, it must be studied whether ignoring the finite interaction range has affected the results. More realistically, particles do interact at a finite range through mutually coupling to classical fields or through the quantum exchange of particles. A variety of ideas have been discussed in the literature for including such interactions in ways which preserve covariance and are consistent with the uncertainty principle [39]. However, due to an assortment of technical challenges, all such approaches remain in the development stage. The effect of finite-range interactions can be incorporated into a Boltzmann treatment with the following prescription. The probability of scattering, not the cross section, is reduced by a factor of λ, i.e. not all particles passing within a distance $\sqrt{\sigma/\pi}$ of one another would scatter. The effects of finite-range interaction will be investigated in detail in Chapter 5.

The use of a large sampling factor has an important advantage for the Monte Carlo solution. As mentioned previously in (3.1.1), the sampling density in the Monte Carlo calculation corresponds to the phase space density. Increasing the phase space density by a factor λ implies that the number of sampling points in the Monte Carlo method must be multiplied by a factor λ. This allows a denser and a more accurate sampling of the phase space density $f(x,p)$, hence, the Monte Carlo result is exact in the Boltzmann limit.

Nevertheless, an exact solution is not generally required for practical purposes, especially given the uncertainties in the experimental data to which model predictions are compared. As a consequence a finite value for the sampling factor λ can be sufficient for extracting observables from Boltzmann-type transport models. The challenge, however, remains to show that computed observables indeed converge in the Boltzmann limit and to identify a lower bound for the sampling factor that still yields satisfactory results.

3.2 The Framework

Gromit has the potential for being employed for partonic as well as hadronic transport models. One application of Gromit for a model with partonic degrees of freedom was demonstrated in [115]. This thesis, however, will be limited to the discussion of a particular hadronic transport model and will mention only those features of the framework that pertain to hadronic degrees of freedom and their interactions.

In addition to its flexibility in the selection of degrees of freedom and interactions between those, Gromit offers the possibility of running simulations in two different coordinate systems. Cartesian coordinates are generally sufficient for simulations at lower-energy heavy ion collisions but their use becomes inefficient and numerically unstable at ultra-relativistic energies such as RHIC energies. The reasons for this will be pointed out in 3.2.5.4. When using a Bjorken coordinate system, the time t and the coordinate along the

beam axis, z, are replaced by

$$\tau = \sqrt{t^2 - z^2}, \text{ and} \tag{3.10}$$

$$\eta = \frac{1}{2} \log \frac{t+z}{t-z}, \tag{3.11}$$

respectively. The coordinate η coincides with the rapidity of an observer who has moved from the origin at $t = 0$ to the spacetime point (t, z) at constant velocity. This observer will be referred to as "co-moving". The transverse coordinates, x and y, remain the same as in the Cartesian coordinate system. Bjorken coordinates are very useful at ultra-relativistic energies, particularly so if the system is boost-invariant along the beam axis. Details will be presented in 3.2.5.4.

3.2.1 Hadrons

By default, Gromit contains all hadrons and their properties tabulated by the Particle Data Group in the *Review of Particle Physics* [81]. However, Gromit is a general framework for arbitrary degrees of freedom and is not limited to these particles or their properties. It may be desirable to define hypothetical particles with simple properties, when studying some schematic system; to deliberately alter certain particle properties; or to select only a subset of known particles, when studying the influence of particular particles or properties. Gromit facilitates these studies through a simple initialization file, in which the degrees of freedom and their specific properties can be specified. An example of such a definition with arbitrary particles is shown in Appendix A.1. To select a subset of known particles it is sufficient to specify the names of multiplets as illustrated in Appendix A.2.

3.2.2 Initial Particle Distribution

Gromit offers the choice of several initial conditions for the transport model in order to provide the greatest flexibility . In addition, the framework permits the introduction of user-

provided initial conditions as new modules. Among the currently available schemes for the initial condition are the Heavy Ion Jet INteraction Generator (`Hijing`), reading a file with a list of initial particles, and boost-invariant initial distributions with simple geometries.

Boost-invariant initial distributions, f_i, for a certain particle type i are usually generated by sampling their momenta according to the Jüttner distribution [96] for a canonical ensemble

$$f_i = \frac{1}{(2\pi)^3(\hbar c)^3} \exp\left(\frac{\mu_i - p^\nu n_\nu}{T}\right), \tag{3.12}$$

where p^ν is the momentum of the particle, n_ν is the velocity of the reference frame, in which the thermodynamic temperature T is measured, and μ is the chemical potential. The particle's spin projection is sampled uniformly over all possible values. In case the number of particles N_i to be produced is unknown, they can be determined from a grand-canonical ensemble.

$$N_i = \int dx^3\, dp^3\; g_i f_i = V \frac{g_i}{2\pi^2(\hbar c)^3} T e^{\mu/T} \int dm\, m^2 K_2(m/T) A_i(m), \tag{3.13}$$

where V is the system volume, m and g_i are, respectively, the mass and the spin degeneracy of the particle, and K_2 is the second-order modified Bessel function of the second kind. The spectral function, $A_i(m)$, is equal to $\delta(m - m_0)$ for stable particles and Eq. (3.14) for resonances. There are several possible choices for the distribution in coordinate space, including: uniform over an ellipse, Gaussian, and a binary collision profile.

The grand-canonical ensemble mentioned above does not conserve quantum number in each event, although it does conserve quantum numbers when averaged over many events. An initial condition based on the algorithm in 2.2.3 conserves quantum numbers as well as total isospin and can be easily added to the framework. Such an initial condition would be especially useful for studies of fluctuations and balance functions, when generating particles either at the interface to a hydrodynamical model or in a boost-invariant distribution.

3.2.3 Resonances

When a resonance is created, its mass is Monte Carlo sampled according to a Breit-Wigner distribution

$$A(m) = \frac{1}{N}\frac{\Gamma(m)}{(m_R - m)^2 + \Gamma(m)^2/4}\Theta(m - m_{\min}), \tag{3.14}$$

where N is the normalization constant, which in the case of mass independent width equals 2π, m_R is the pole mass of the resonance according to [81], and $m_{\min}$ is the threshold mass for the resonance production.

Gromit contains a loadable table of all known decay branches for resonances from the *Review of Particle Properties* [81] as long as the final state contains two or three particles. However, decays will be generated only for those particles that were explicitly included in the simulation. Currently, decays into three particles violates detailed balance (see 3.2.4.6) in this framework as the inverse process $3 \to 1$ has not yet been included. Gromit offers two options for the partial decay width, but it was ensured that additional functions for the decay width could be easily incorporated into the model. The simplest choice for the partial width is a constant, where kinematically allowed, and zero otherwise. The other option for the partial width implements a parameterization for a mass and momentum dependent width suggested by [99, 156].

$$\gamma^{(l)}(s, m_r, m_1, m_2) = \frac{m_r}{\sqrt{s}}\left(\frac{k(s)}{k(m_r^2)}\right)^{2l+1}\left(\frac{k^2(m_r^2)+\beta^2}{k^2(s)+\beta^2}\right)^{l+1}, \tag{3.15}$$

where the parameters l and β denote angular momentum and a cut-off value, respectively. The width is set to zero, where kinematically prohibited.

The width has to be related to the lifetime of a resonance τ in a manner consistent with the ergodic theorem [54]. The lifetime for a usual Breit-Wigner-type resonance is

$$\tau = \frac{1}{\Gamma} \tag{3.16}$$

At the end of its lifetime, the resonance is decayed into the final-state particles. A widespread practice, when modeling resonance decays in microscopic models, is to place the decay products at the spacetime point where the resonance was located. This is also adopted in Gromit. This procedure, however, moves particles closer together, on average over the entire evolution of the system, thus contributing a negative pressure. An alternative to this practice could be to remember the spacetime separation of the particles forming the resonance and to assign this separation to the decay products when the resonance decays. The effects of the different decay product placement on the pressure should be studied in the future.

The assignment of outgoing momenta is straight forward, when there are only two particles in the final state. In the rest frame of the resonance, each daughter particle is assigned a momentum according to Eq. (3.18), such that the total momentum in the center of mass frame of the resonance vanishes and the direction of the relative momentum is distributed to match s-wave scattering. Other implementations for the angular distribution of the relative momentum are readily accepted by Gromit. The case of three particles in the decay final state will be treated next.

3.2.3.1 3-Body Final State

The case of three particles in the decay final state is more complicated. According to [81] the 3-body phase space is

$$d\Gamma = \frac{1}{(2\pi)^5}\frac{1}{16M^2}\,|\mathcal{M}|^2\,|\mathbf{p_1^*}|\,|\mathbf{p_3}|\,dm_{12}\,d\Omega_1^*\,d\Omega_3, \tag{3.17}$$

where M is the mass of the decaying particle, $(|\mathbf{p_1^*}|, \Omega_1^*)$ is the momentum of final state particle 1 in the rest frame of 1 and 2, and Ω_3 is the angle of final state particle 3 in the rest frame of the decaying particle. The momenta $|\mathbf{p_1^*}|$ and $|\mathbf{p_3}|$ can be expressed using the general form for the particle momenta in the center-of-mass frame of two particles with

momenta p_1 and p_2 and masses m_1 and m_2

$$|\mathbf{p}_1| = |\mathbf{p}_2| = k(\sqrt{s}, m_1, m_2) = \frac{1}{2\sqrt{s}}\sqrt{[s-(m_1+m_2)^2][s-(m_1-m_2)^2]}, \tag{3.18}$$

where $s = (p_1 + p_2)^2$. Then $|\mathbf{p_1^*}| = k(\sqrt{s}, m_1, m_2)$ and $|\mathbf{p_3}| = k(M, \sqrt{s}, m_3)$. The matrix element $\mathcal{M}$ is generally assumed to be independent of m_{12}, Ω_1^*, and Ω_3. Therefore, the 3-body phase space can be sampled by sampling m_{12}, Ω_1^*, and Ω_3 according to the the bounded weight $|\mathbf{p_1^*}||\mathbf{p_3}|$. This can be incorporated into a keep-or-reject algorithm that compares $|\mathbf{p_1^*}||\mathbf{p_3}|$ for a given set of sampled parameters, m_{12}, Ω_1^*, and Ω_3, to an upper bound, which is ideally an absolute maximum. As this absolute maximum is difficult to find, an upper bound of $|\mathbf{p_1^*}|_{\max}|\mathbf{p_3}|_{\max}$, is used, where $|\mathbf{p_1^*}|_{\max} = k(M - m_3, m_1, m_2)$ and $|\mathbf{p_3}|_{\max} = k(M, m_1 + m_2, m_3)$.

3.2.4 Cross Sections

In a Monte Carlo simulation of the BTE, cross sections are needed in three distinct ways. The total cross section σ_{tot} is used to decide whether two particles are going to interact, which they do if their relative distance is less than $\sqrt{\sigma_{\text{tot}}/\pi}$. Once it has been established that the interaction in going to happen, the partial cross sections σ_i serve to choose the specific reaction channel, i.e., what kind of reaction will occur and what the final state particles will be. The probability of a certain reaction channel equals $\sigma_i/\sigma_{\text{tot}}$. An angular distribution, or the differential cross section, is then needed to assign the directions of the momenta in the final state.

Several functions have been implemented in Gromit for each of these, total, partial, and differential cross sections. Among the options presently offered for the total and partial cross sections are, for example, a constant cross section and a tabulated cross section that reads in a file with cross section data. Files of experimentally measured cross sections are supplied for a variety of hadron interactions and can be used at the user's discretion.

3.2.4.1 Total Cross Section

Unless otherwise determined, the total cross section is obtained by addition of all partial cross sections,

$$\sigma_{\text{tot}} = \sum_i \sigma_i. \tag{3.19}$$

When some total cross section is very well known, it might be desirable, instead, to use tabulated values, a parameterization, or a combination of these two. Gromit supplies loadable files with experimentally measured total cross sections for a variety of hadron interactions as well as a customizable cross section function for any user-specified parameterization.

In case a specific total cross section is requested, discrepancies can arise between that cross section and the sum of partial cross sections. The default choice in Gromit is to ignore this discrepancy as the two values are used for different purposes. The specified total cross is only used for the determination of an interaction, while the sum of partial cross sections is only used for the probability of finding a certain reaction channel.

A different scheme can be used to remove the discrepancy entirely: If $\Delta\sigma = \sigma_{tot} - \sum\sigma_i > 0$, a default inelastic channel with partial cross section $\Delta\sigma$ is added. On the other hand, if $\Delta\sigma < 0$, the uncertain partial cross sections are rescaled to match the total cross section. Most partial cross section earn the designation of "uncertain" since experimental data are available for only a few reactions and theoretical predictions lack sophistication. The drawback of this rescaling of partial cross sections is its inconsistency with detailed balance (which is described in 3.2.4.6). For instance, in reactions involving well-measured cross sections for the forward reaction but unknown cross sections for the reverse process, e.g. $np \to XY$, rescaling would take place only for the forward, but not the the reverse, reaction.

3.2.4.2 Additive Quark Model

Nucleon-nucleon experiments in the 1970's and 1980's demonstrated that, except for the effects of the usual conservation laws, particle production in high energy jets is largely independent of the incoming hadron [116, 57, 20]. This concept is usually referred to as hadron universality and it suggests that interactions between hadrons are mainly governed by similar mechanisms. Hadron universality provides, therefore, the basis for the additive quark model that parameterizes unknown hadron-hadron cross sections by the quark content of the hadrons [80]. In this model the total and elastic cross section are given, respectively, by

$$\sigma_{\text{tot}} = 40 \left(\frac{2}{3}\right)^{m_1+m_2} \left(1 - 0.4\frac{s_1}{3-m_1}\right)\left(1 - 0.4\frac{s_2}{3-m_2}\right) \tag{3.20}$$

and

$$\sigma_{\text{el}} = 0.039\sigma_{\text{tot}}^{3/2}, \tag{3.21}$$

where the cross sections are given in units of 10^{-3} barns, s_i is the number of strange quarks in particle i, and $m_i = 1$, if particle i is a meson, $m_i = 0$ otherwise. This approximation of constant cross sections is good only for very high energies.

3.2.4.3 Resonance Formation

In this model, a resonant scattering process, $A_1 + A_2 \xrightarrow{R} B_1 + B_2$, is modeled as two distinct processes, a resonance formation process, $A_1 + A_2 \rightarrow R$, followed by a resonance decay, $R \rightarrow B_1 + B_2$. The resonance formation is assigned a Breit-Wigner cross section, that is consistent with the measured resonant elastic and inelastic cross sections, when folded with the decay branching ratio. The spin-averaged Breit-Wigner cross section for a collision of two particles with spin S_1 and S_2 to produce a spin-J resonance is

$$\sigma_{AB\rightarrow R}(s) = \frac{\pi}{[k(\sqrt{s}, m_A, m_B)]^2} \frac{\Gamma_{R\rightarrow AB}\Gamma_R}{(M_R - \sqrt{s})^2 + \Gamma_R^2/4} \frac{2J+1}{(2S_1+1)(2S_2+1)}, \tag{3.22}$$

where M_R is the pole-mass of the resonance, m_A and m_B are the respective masses of the incoming particle, $k(\sqrt{s}, m_A, m_B)$ is the momentum of one particle in the center of mass frame given in Eq. (3.18), Γ_R is the total width, and $\Gamma_{R\to AB}$ is the partial width of the resonance decay.

The cross section given in Eq. (3.22) might diverge at the threshold, as the momentum k in the denominator vanishes, unless the mass-dependent width in the numerator goes to zero faster than the momentum. In case a constant width is used, the divergence in the cross section has to be removed. One possible scheme is to introduce a cut-off in the momentum $k_{\text{cut}} = 10$ MeV, below which the cross section vanishes. This scheme is presently implemented in Gromit but may be changed in the future. Another alternative is to replace the mass dependent momentum in the pair rest frame $k(\sqrt{s}, m_A, m_B)$ by a constant momentum $k = k(M_R, m_A, m_B)$ to eliminate of the singularity.

Equation (3.22) is only valid for stable incoming particles because of the mass dependence in the momentum $k(\sqrt{s}, m_A, m_B)$. This can be remedied by replacing the momentum in the numerator by an averaged value, as suggested in [23],

$$\langle k(\sqrt{s})\rangle = \int_{M_1^{min}}^{\sqrt{s}-M_2^{min}} dm_1\, A_1(m_1) \int_{M_2^{min}}^{\sqrt{s}-m_1} dm_2\, A_2(m_1)\, k(\sqrt{s}, m_1, m_2). \tag{3.23}$$

3.2.4.4 *NN*-excitations

Nucleon-nucleon excitations (*NN*-excitations) are much more important at AGS and SPS energies than at RHIC energies because nucleons make up less than 10% of the particles at the higher energies. *NN*-excitations are included in the model to extend its range of validity, however, it is anticipated that the main focus in the research of relativistic heavy-ion collisions is increasingly shifting to RHIC energies. The following approximate parame-

terization is used for the various $NN \to XY$ cross sections [23]

$$\sigma_{12\to 34} \approx (2S_3+1)(2S_4+1)\frac{k_{34}}{k_{12}}\frac{1}{s}\left|\mathcal{M}(s,m_3,m_4)\right|^2 \tag{3.24}$$

where k_{12} and k_{34} are the momenta of the particle pair $\{1,2\}$ and $\{3,4\}$, respectively, in the center of mass frame given in Eq. (3.18). The matrix element $\mathcal{M}(s,m_3,m_4)$ depends on the particle types in the outgoing channel.

For $NN \to N\Delta$ the matrix element is given by

$$|\mathcal{M}|^2_{NN\to N\Delta} = 40000\frac{m_\Delta^2\Gamma_\Delta^2}{(s-m_\Delta^2)^2+m_\Delta^2\Gamma_\Delta^2}, \tag{3.25}$$

where $m_\Delta = 1.232\,\text{GeV}$, $\Gamma_\Delta = 0.12\,\text{GeV}$. The corresponding matrix element for $NN \to \Delta\Delta$ is

$$|\mathcal{M}|^2_{NN\to\Delta\Delta} = 2.8, \tag{3.26}$$

and for the other NN-excitation the matrix element is

$$|\mathcal{M}(s,m_3,m_4)|^2 = \frac{A}{(m_3-m_4)^2(m_3+m_4)^2}, \tag{3.27}$$

where $m_{N^*} = 1.44\,\text{GeV}$, $m_{\Delta^*} = 1.6\,\text{GeV}$ and the values for the parameter A are given in Table 3.1. [1]

Excitation	A [GeV^4]
$NN \to NN^*$	6.3
$NN \to N\Delta^*$	12
$NN \to \Delta N^*$	3.5
$NN \to \Delta\Delta^*$	3.5

Table 3.1: Parameter A for NN-excitation matrix elements.

3.2.4.5 Baryon-Anti-Baryon Annihilation

Rapp and Shuryak [134, 135] found that in relativistic heavy-ion collisions the proton–anti-proton annihilation with several pions in the final state, $p\bar{p} \to \bar{n}\pi$, where $\bar{n} = 5-6$, is

[1] Whereas the other A parameters are determined to best fit the experimentally available data, no such data are available for $NN \to \Delta\Delta^*$. Its parameter is, therefore, taken to be the same as in $NN \to \Delta N^*$

substantially counterbalanced by its inverse reaction. This effect is believed to be relevant at RHIC energies, albeit less than that at SPS energies. It would, therefore, violate time reversal invariance, if $B\bar{B}$-annihilation were included in a microscopic simulation without accounting for the inverse many-body processes $n\pi \rightarrow B\bar{B}$ with $n \geq 2$.

However, including such many-body collisions explicitly into a microscopic model is presently difficult. Besides the practical problems involved with numerical simulations, it remains unclear how many-body collisions can be included in the theoretical framework of Boltzmann-type models because the Boltzmann transport equation and its modifications only describe binary collisions. One possibility of including many-body collisions implicitly in future models is to subtract the cross section of the many-body process from the cross section of the inverse binary collision. Of course, this would be possible only, if the population of the incoming channel was overpopulated relative to the outgoing channel.

3.2.4.6 Detailed Balance

Detailed balance is a consequence of time reversal invariance of the scattering matrix and relates the cross section of a reaction to that of its inverse. This relation can be derived starting from a time-dependent Hamiltonian $H(t)$ that is essentially time-independent (given by H_0) with a small time-dependent perturbation $H'(t)$

$$H(t) = H_0 + H'(t). \tag{3.28}$$

Fermi's golden rule then states the transition probability per unit time as

$$W_{fi} = \frac{2\pi}{\hbar} |\langle \phi_f | H' | \phi_0 \rangle|^2 \rho(E_f), \tag{3.29}$$

where the ϕ's are eigenfunctions of the time-independent Hamiltonian H_0 and the density of states $\rho(E_f)$ is given by

$$\rho(E_f) = 4\pi g_f \frac{V}{h^3} \mathbf{p}_f^2 \frac{d\mathbf{p}_f}{dE_f}. \tag{3.30}$$

If the matrix element $\mathcal{M}_{fi} = \langle \phi_f | H' | \phi_0 \rangle$ is time reversal invariant, i.e. $|\mathcal{M}_{fi}|^2 = |\mathcal{M}_{if}|^2$, then

$$\frac{W_{fi}}{\rho(E_f)} = \frac{W_{if}}{\rho(E_i)}. \tag{3.31}$$

The transition probability is related to the cross section by $W_{fi} = \sigma_{fi}\mathbf{v}_i/V$, where $\sigma_{fi}\mathbf{v}_i$ is the volume "probed" by the particle per unit time. Substituting the transition probabilities in Eq. (3.31) by the cross section leads to

$$\sigma_{fi}\mathbf{v}_i\rho(E_i) = \sigma_{if}\mathbf{v}_f\rho(E_f). \tag{3.32}$$

Finally, the cross section for the inverse process can be written in terms of the cross section of the forward process

$$\sigma_{if} = \frac{g_i}{g_f}\frac{\mathbf{p}_i^2}{\mathbf{p}_f^2}\sigma_{fi}. \tag{3.33}$$

Eq. (3.33) is strictly only valid for stable particles. In case there are resonances in the incoming or outgoing channels, the corresponding momentum in Eq. (3.33) has to be replaced by the average momentum given in Eq. (3.23).

3.2.4.7 Differential Cross Section

At this point, Gromit provides two different expression for the differential cross section but more functions can be added easily, if desired. The differential cross section are given in the center of mass frame of the binary collision. The choices for the function include the s-wave distribution

$$\frac{d\sigma}{d(\cos\theta)} = const \tag{3.34}$$

and the forward-peaked screened Rutherford scattering, or "gluonic", distribution [163]

$$\frac{d\sigma}{dt} = \frac{9\pi}{2}\frac{\alpha_s^2}{(t-\mu^2)^2}. \tag{3.35}$$

Here, $t = (p_1 - p_3)^2$ is one of the usual Mandelstam variables, $\alpha_s = \sqrt{2/9}$, and the screening mass μ is chosen to match the cross section, such that

$$\sigma = \frac{9\pi\alpha_s^2}{2\mu^2}. \tag{3.36}$$

3.2.5 Collision Handling

It has become apparent that arbitrary algorithmic choices in transport models constitute themselves major model assumptions that alter the extracted results. It is, therefore, imperative that such algorithmic choices are thoroughly documented and studied. Several such studies will be discussed in Chapter 4.

3.2.5.1 Invariant Impact Parameter

The impact parameter between two particles, 1 and 2, is defined as the distance of closest approach in the pair's center of mass frame,

$$b = \min\left(|\mathbf{x}_2(t) - \mathbf{x}_1(t)|\right). \tag{3.37}$$

Boosting into the pair's center of mass frame can be avoided by writing this impact parameter only in terms of Lorentz invariant scalars, i.e. in a manifestly invariant form. The following quantities will prove useful in the calculation of this invariant impact parameter for two particles at spacetime positions x_1 and x_2 with 4-momenta p_1 and p_2 in an arbitrary reference frame,

$$x = x_2 - x_1, \tag{3.38}$$

$$P = p_1 + p_2, \tag{3.39}$$

$$q = p_2 - p_1 - \frac{P\cdot(p_2 - p_1)}{P^2}P, \tag{3.40}$$

$$b = x - \frac{P\cdot x}{P^2}P - \frac{q\cdot x}{q^2}q. \tag{3.41}$$

The impact parameter vector b is defined in Eq. (3.41) such that it is perpendicular to the relative momentum, i.e., $b\cdot q = 0$. With the above definitions, the square of the invariant impact parameter is given by

$$\mathrm{b}^2 = -b^\mu b_\mu = -x^2 + \frac{(P\cdot x)^2}{P^2} + \frac{(q\cdot x)^2}{q^2}, \tag{3.42}$$

or expressed in terms of the original momenta,

$$\mathrm{b}^2 = -x^2 + \frac{p_2^2(p_1\cdot x)^2 + p_1^2(p_2\cdot x)^2 - 2(p_1\cdot p_2)(p_1\cdot x)(p_2\cdot x)}{p_1^2p_2^2 - (p_1\cdot p_2)^2}. \tag{3.43}$$

This expression for the invariant impact parameter can be substantially simplified if the particles are massless particles,

$$\mathrm{b}^2 \equiv -x^2 + \frac{2(p_1\cdot x)(p_2\cdot x)}{(p_1\cdot p_2)}. \tag{3.44}$$

3.2.5.2 Collision Times and Ordering

The points on the particles' trajectories, x_1' and x_2', where they reach the point of closest approach in the center of mass frame are given by

$$x_1' = x_1 + \frac{p_2^2(p_1\cdot x) - (p_1\cdot p_2)(p_2\cdot x)}{p_1^2p_2^2 - (p_1\cdot p_2)^2}p_1, \tag{3.45}$$

$$x_2' = x_2 - \frac{p_1^2(p_2\cdot x) - (p_1\cdot p_2)(p_1\cdot x)}{p_1^2p_2^2 - (p_1\cdot p_2)^2}p_2 \tag{3.46}$$

where the same notation is used as in the previous subsection. The time components coincide, $t_1' = t_2'$, in the pair's center of mass frame. However, since the two particles are generally separated by a finite distance, these two times are not necessarily simultaneous in another reference frame, which must be adopted in the numerical simulation for ordering the interactions in time.

It is impossible to honor the individual collision times for each particle as this would lead to acausalities in the ordering of collisions. For example, consider three particles that are going to interact pairwise and inelastically. The time in particle i's frame, at which particle i collides with particle j, is denoted by t_{ij}. A possible situation that could arise for the relationship between the various collision times is: $t_{13} < t_{12}$, $t_{32} < t_{31}$, and $t_{21} < t_{23}$. In order to determine which particle pair should be collided first, the following constraints

have to be considered. Particles 1 and 3 should be collided before 1 and 2 as the former inelastic collision removes particle 1, thus rendering the latter collision invalid. However, before 1 and 3 can be collide, particle 3 has to be collided with particle 2. Finally, before colliding with particle 3, particle 2 has to interact with particle 1 first. In this circular deadlock, it impossible to decide which pair of particles to collide first.

Therefore, a strategy needs to be devised for assigning a unique time to a collision for the purpose of time-ordering the pairwise interactions. In principle, any function that takes those two individual times and computes a unique collision time for the pair is permissible. Obvious choices include

$$T_{\rm col}^{av} = \frac{t_1 + t_2}{2}, \tag{3.47}$$

$$T_{\rm col}^{min} = \min(t_1, t_2), \tag{3.48}$$

$$T_{\rm col}^{max} = \max(t_1, t_2). \tag{3.49}$$

Because this is an arbitrary algorithmic choice, the results of the model must be independent of the selected prescription. This will be demonstrated for several Boltzmann-type models in Chapters 4 and 5.

When using Bjorken coordinates, there is an additional choice for obtaining an unique collision time for collision ordering. Either, the individual τ's are combined to a collision τ

$$\tau_{\rm col}^{arith} = \frac{\tau_1 + \tau_2}{2}, \tag{3.50}$$

$$\tau_{\rm col}^{geo} = \sqrt{\frac{\tau_1^2 + \tau_2^2}{2}} \tag{3.51}$$

or the t's and z's are combined first and then used to calculate a collision τ

$$\tau_{\rm col}^{tz} = \sqrt{\left(\frac{t_1 + t_2}{2}\right)^2 - \left(\frac{z_1 + z_2}{2}\right)^2}. \tag{3.52}$$

3.2.5.3 Collision Prescription

Although for the purpose of collision ordering the two individual times, t_{12} and t_{21}, have to be combined to a unique collision time, there is still the option of propagating the particles to a time other than the collision ordering time when the interaction is processed. For example, particle 1 could be propagated to t_{12} and particle 2 to t_{21}. This might move a particle back in time, perhaps even to a period before they were created. The evidently illogical situation could be avoided by simply rejecting any such collision. However, there is another serious problem with moving the particles to their individual times t_{12} and t_{21}. The particles do not collide at the distance of closest approach in this scheme, which means that the actual interaction range can be greater than $b_{max} = \sqrt{\sigma/\pi}$.

To demonstrate this problem, the particle separation in the center of mass frame is calculated,

$$r_{\text{sep}} = \left| \mathbf{x}_2(t_2^{\text{col}}) - \mathbf{x}_1(t_1^{\text{col}}) \right|, \tag{3.53}$$

where $t_{1,2}^{\text{col}}$ are the times and $\mathbf{x}_{1,2}$ the positions in the center of mass frame, at which the particles receive a momentum kick. The particle separation r_{sep}^2 needs to be compared to d^2, the squared distance of closest approach from Eq. (3.42), which is always bounded by $d^2 < \sigma/\pi$. An analytic solution is presented here for massless particles, while the case of massive particles is treated numerically.

The first prescription to be examined assumes that massless particles are moved to their individual collision times, t_{12} and t_{21}, then

$$r_{\text{sep}}^2 - b^2 = \left[\frac{t(1 - \mathbf{v_1} \cdot \mathbf{v_2}) + \mathbf{x} \cdot (\mathbf{v_1} - \mathbf{v_2})}{(1 - \mathbf{v_1} \cdot \mathbf{v_2})} \right]^2, \tag{3.54}$$

where $\mathbf{x} = \mathbf{x}_2 - \mathbf{x}_1$ and $\mathbf{v_1}$ and $\mathbf{v_2}$ are the particles velocities. This means that the particle separation at the time of interaction is larger than the impact parameter. What is even worse, there is no upper bound to the particle separation. In case, the prescription propagates both

particles in the collision to a common time $t_{\text{col}} = (t_{12} + t_{21})/2$, it is found that

$$b^2 - r_{\text{sep}}^2 = \frac{\left[\mathbf{x} \cdot (\mathbf{v_1} + \mathbf{v_2}) - t(1 + \mathbf{v_1} \cdot \mathbf{v_2})\right]^2}{2(1 - \mathbf{v_1} \cdot \mathbf{v_2})}. \tag{3.55}$$

The denominator is always nonnegative as $\mathbf{v_1} \cdot \mathbf{v_2} < 1$. Therefore, the particle separation is bounded

$$r_{\text{sep}} \leq b \leq \sqrt{\frac{\sigma}{\pi}}. \tag{3.56}$$

Numerical studies with massive particles confirm the analytical findings for massless particles. They also show that the average-τ prescription yields no collisions where the particle separation exceeds $\sqrt{\sigma/\pi}$. As a result of this discussion, particles are generally propagated to the common collision ordering time in the Gromit framework.

3.2.5.4 Collision Mesh in Cartesian and Bjorken Geometries

To find all collisions between every particle pair in a system with N particles requires an $O(N^2)$ algorithm. At initialization the collisions have to be determined this way and stored. However, after a collision has taken place, particles pairs, where neither particle was involved in the collision, do not need to be checked again for collisions. New collisions could only result from the changes to the reacting particles between those and the other particles. The scaling of this search is $O(N)$ and cannot be fundamentally improved. However, the number of checks can be significantly reduced because a particle can only collide with other particles within its range of interaction.

This interaction range cannot correspond to a specific cross section because the potential reaction partners are unknown until after an interaction range was determined and the adjacent cells searched for collision partners. Instead, the interaction range has to be determined form a overall maximum cross section. There is, however, no analytical or numerical way to determine this maximum cross section in a general framework, where any function

could be used for the cross section. Therefore, the maximum total cross section are determined through a Monte Carlo scheme. They are initially estimated for each particle and then updated as larger cross sections are found. The information about the maximum cross sections are stored across events and yield satisfactory upper bounds for the cross sections after a few simulations. Since cross sections for the different particles vary greatly, the collision finding algorithm can be further sped up by recording the maximum individually for each particle type.

To optimize the search for collisions, particle are placed into cells within a mesh. The particle-cell assignment have to be updated continuously, such that it is accurate at any point in time. This requires additional computational overhead but is generally justified by the speed-up in the collision finding algorithm. After an interaction has taken place, the modified particles need to be checked for collisions only with other particles that are in its own cell or in adjacent cells within its maximum interaction range. The optimal size of cells sensitively depends on the density and is determined by the trade-off between increasing the number of updates of particle-cell assignment and decreasing the number of neighboring cells searched after a collision. Often times, yet, it may not be feasible to use the optimal cell size since the number of computational cells is limited by the available memory. This restriction becomes serious particular when a high sampling factor λ is chosen along with a reduction in the interaction range.

Gromit can be run with meshes in either Cartesian coordinates (t, x, y, z) or Bjorken coordinates (τ, x, y, η). The latter is required if one is to implement periodic boundary conditions in rapidity. Bjorken coordinates are also recommended if the system covers a large spread in rapidity, e.g. at RHIC or LHC energies. In these case, the Bjorken mesh naturally expands along with the system and, hence, maintains a more even distribution of particles across the mesh.

A collision finding mesh as described above can be useful only if the particle separations are truly bounded by the interaction range. It was shown in 3.2.5.3 that the particle separation are bounded only if certain collision prescriptions were used. Yet another complication might arise from a collision prescription that allows collisions in a particle's past. For instance, consider a particle for which a collision time is determined in its past. At the time when the collision is inspected the particle will have passed the point of closest approach and might be a great distance away from it. Hence, this collision would not be registered when using a collision finding mesh where only neighboring cells are searched for potential collision partners. Consequently, use of a collision mesh is inconsistent with particle propagation backward in time. Since not all collision prescriptions are consistent with the use of a collision finding mesh, care is required when choosing the collision prescription.

Another benefit of using a collision mesh is that it facilitates implementation of periodic boundary conditions. When using Bjorken coordinates the following transformation are required to move a particle at one end by $\Delta\eta$ to the other end,

$$\tau' = \tau, \tag{3.57}$$

$$\eta' = \eta \pm \Delta\eta, \tag{3.58}$$

$$m_t' = m_t, \tag{3.59}$$

$$y' = y \pm \Delta\eta, \tag{3.60}$$

where $\Delta\eta$ is the system's extend in the η-direction, the sign depends on the direction of motion, the transverse mass $m_t = \sqrt{E^2 - p_z^2}$, and y is the rapidity. This transformation is chosen to preserve the energy in the comoving frame, $m_t'(\eta' - y') = m_t(\eta - y)$.

3.2.5.5 Run-time Estimates

The use of a collision mesh as described above greatly reduces the run-time required for the simulation of one event. This facilitates faster testing of new ideas but even more importantly, it improves the quality of the results obtained from the Monte Carlo simulations in two ways. First, more samples can be computed to increase the reliability of the Monte Carlo solution and to reduce the statistical error bars associated with the results. Second, numerical calculations with higher values of the sampling factor λ become feasible, which are required to extract correct predictions from the simulations. The latter point has been mentioned in Subsection 3.1.2 and will be studied in more detail in Chapter 4.

The run-time required for one event depends greatly on the details of the model implemented within the Gromit framework and can range from fractions of a second to several minutes. On a system with a Pentium 4 processor rated at 2.2 GHz, the simulation of one gold-on-gold event at an energy of $\sqrt{s_{NN}} = 200$ GeV, as described in Chapter 7, requires about 40 seconds. However, more important than the absolute run-time is the scaling of the run-time as the parameters of the models change. For typical simulations, the run-time of models based on the Gromit framework are found to scale as

$$O(\lambda n^2 V), \tag{3.61}$$

where n is the density and V the volume of the system. This scaling is approximate but deviations are relatively small. The linear scaling with the sampling factor is only valid if the cross sections are scaled by $1/\lambda$, which allows cell sizes to be adjusted to match the smaller interaction range. This, however, comes at the expense of using more cells in the collision finding mesh and, accordingly, more computer memory.

As a consequence of the linear scaling with the sampling factor, most calculations with larger sampling factors do not require more run-time if the statistical errors are to be kept constant. Although the run-time for one event increases by a factor λ, the event also in-

volves a factor λ more particles. Therefore, in a given amount of time, the same number of particles can be processed, keeping the statistical errors constant independent of the sampling factor.

3.2.5.6 Secondary Scattering

Particles that have just scattered attractively, as displayed in Figure 3.1, are very likely to

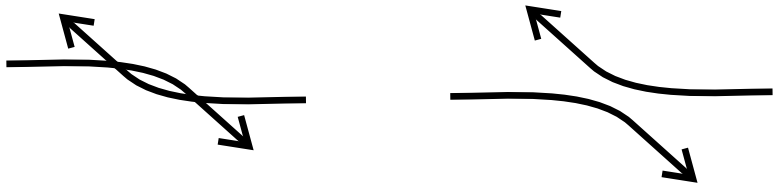

Figure 3.1: Illustration of attractive vs. repulsive scattering.

scatter again within a very short time due to their proximity. If attractive, this second scattering, might lead to a third, and so on, until one scattering is repulsive. In fact, if the density is high in some region, particles within this region scatter among each other so many times that it effectively halts the simulation. More seriously, this kind of attractive scattering has been shown to modify the thermodynamic properties of the system by effectively reducing the pressure [54]. The cause for this unphysical behavior of the secondary collisions are the short time separations between collisions. This, in turn, is a consequence of the instantaneous collisions that were introduced in 3.1.1. Instantaneous collisions, though, are not found in nature where finite time scales are associated with interactions.

Such interaction time scales can be mimicked in the Monte Carlo simulation by requiring that particles involved in an interaction do not interact within a certain dead time t_{dead}. This time would allow the particles to separate from each before colliding again. This prescription, however, reduces the overall collision rate.

An alternative to blocking all interactions within a certain dead time, is to restrict par-

ticles involved in an interaction from colliding with each other until either of them has interacted with a third particle ("weak blocking") or until they have both interacted with other particles ("strong blocking"). Gromit implements both these possibilities and offer the choice between weak and strong blocking.

3.2.5.7 Conservation Laws

Conservation of energy and momentum is relevant for Boltzmann-type models on two scales, the macroscopic and microscopic scale. On the macroscopic scale, the fundamental conservation of energy and momentum throughout the evolution of the collision crucially affects the thermodynamic properties of the system like temperature and pressure. Since the goal of modeling relativistic heavy-ion collisionsis to discern bulk properties of the collision, it is important for any model to conserve energy and momentum on the macroscopic scale.

This, though, does not necessarily imply that energy and momentum have to be conserved microscopically, i.e., in each interaction between the individual particles in the simulation. In fact, some Boltzmann-type models choose to model the average effect of collisions and, therefore, only conserve energy and momentum on average. In the Gromit framework, energy and momentum are exactly conserved in each microscopic interaction as well as macroscopically across the entire evolution of the collision. This is numerically ascertained for every individual interaction in the Gromit framework and has been verified for the macroscopic evolution of the model.

Preservation of the reaction plane has previously been implicated to affect calculations of another important observable, elliptic flow discussed in Section 4.2, in the cascade limit ($\lambda = 1$) [97]. The Gromit framework facilitates the investigation of this possible effect by providing the possibility of preserving the reaction plane in each binary collision. The stricter conservation of angular momentum in each microscopic collision cannot, even for

nonrelativistic cases, be implemented consistently with scattering at the distance of closest approach.

Furthermore, it should be noted that due to the finite range of interactions in microscopic simulations, charges are generally not locally conserved. In an inelastic collision, the incoming charges are removed when they reach their point of closest approach. These charges are then replaced by the outgoing particles that have the same net charge but different individual charges. In addition, the outgoing charges might not emerge from the same points, at which the incoming charges were removed. As a consequence of moving the charges across finite distances charges are not locally conserved, although charges are conserved overall.

Chapter 4

Results and Tests of Microscopic Models

The search for the quark-gluon plasma with relativistic heavy-ion collisions is mainly hampered by the lack of firm theoretical predictions of QGP signals. Theoretical predictions are frequently made for the early stages of the collision where novel phenomena are expected to take place. The predicted effects are then followed through the collision dynamics with transport models to arrive at a prediction for the final state of the collision. Besides disagreements between different models, there are considerable uncertainties about the dynamics contained in the models. It is, therefore, imperative to thoroughly study the contributions of model assumptions, arbitrary or not, and their effects on extracted observables.

In microscopic models based on the Boltzmann equation, the most important unconstrained model parameter is the sampling factor λ discussed in Subsection 3.1.2. It determines how densely the phase space distribution is sampled. The exact solution of the Boltzmann equation is obtained with Monte Carlo methods only in the Boltzmann limit, $\lambda \to \infty$. Nevertheless, calculations have to be performed with a finite sampling factor λ, which introduces instantaneous interaction across finite distances. This leads to issues involving Lorentz covariance [103, 163], which have to be resolved by arbitrary prescriptions.

A number of these arbitrary prescriptions were mentioned in this thesis. For instance, a prescription is needed for ordering collisions in time. Each collision can be assigned a

point in space time. However, since many points would have space-like separations, time ordering is frame dependent. Another aspect of arbitrariness derives from the collision prescription for altering the trajectories of the two particles. Since the particles are separated by a finite distance the notion of simultaneously changing the momenta is inherently frame dependent. This finite distance is dependent on the scheme chosen to implement the scaling of the transition probability as the sampling factor λ changes. In one scheme, the cross section is scaled by $1/\lambda$ to account for the change in the transition probability, whereas in the other scheme, the appropriate number of collisions is rejected while leaving the interaction range constant. Preservation of the reaction plane in each scattering is another algorithmic choice that has been shown to affect elliptic flow in the cascade limit ($\lambda = 1$) [97]. Finally, even in the nonrelativistic limit, scattering at the point of closest approach violates conservation of angular momentum.

Furthermore, there are other issues with scattering algorithms that are mentioned but will not be addressed here. For example, particles might scatter with an impact-parameter-dependent probability that has a more complicated form than a simple step function. Also, scattering need not occur instantly. Delaying the particles a certain time, before they emerge with their asymptotic momenta, can effectively alter the pressure [54]. Such time delays must be coordinated with in-medium modifications and knowledge of the phase shifts in order to be ergodically consistent with thermodynamic properties at the level of the second virial coefficient [54].

Despite this multitude of arbitrary algorithmic choices, results extracted from Boltzmann-type models should converge in the Boltzmann limit. In the following, this will be ascertained for particle spectra and elliptic flow by studying their sensitivities to some of the above mentioned prescriptions in a schematic model. Calculations of elliptic flow in another simplified model with only elastic collisions are then compared to experimental data to verify the dynamics contained in the Gromit framework. The same model is also utilized

to study the effect of elliptic flow in the initial condition on the elliptic flow in final state. Finally, a more realistic model with mesonic and baryonic resonances as well as inelastic collisions is applied to explore the regeneration of ρ mesons in the collision dynamics.

4.1 Particle Spectra

To illustrate the sensitivity of results to algorithmic choices, we compare results from four numerical approximations to the Boltzmann equation which are realized in four separate models, each arising from a different author. All the algorithms discussed here scatter particles instantaneously at the point of closest approach, and all the models assume a simple $s-$wave form to the cross section. Each algorithm is executed using the same initial conditions, and each is executed both in the cascade limit ($\lambda = 1$) and with a high sampling factor, $\lambda = 16$. Due to the arbitrariness inherent to algorithms with finite-range interactions it should not be surprising for results to vary between codes with $\lambda = 1$, but it is expected that results from the four approaches should converge in the large λ limit.

The four models differ in their definition of "simultaneous", in their time-ordering prescriptions and in whether they preserve the scattering plane in two-particle scattering. The four algorithms compared here represent the following choices:

1. ZPC: A parton cascade code authored by B. Zhang [159]. Particles scatter at the point of closest approach, simultaneous in a fixed reference frame. This time is determined by first finding the spacetime points x_1' and x_2', where the two particles would scatter should they alter their trajectories simultaneously in the two-particle center-of-mass frame, as given in Eqs. (3.45) and (3.46). In a designated laboratory frame, a time is determined by averaging t_1' and t_2'. The trajectories of both particles are simultaneously altered at this average time. The reaction plane is preserved in each two-body scattering, and scattering between the same partners is allowed after

one particle has scattered with a third particle.

2. Gromit-*t*: A generic scattering engine developed for the RHIC Transport Theory Collaboration (RTTC) [137]. This should be identical to ZPC.

3. MPC(0.4.0): A Boltzmann description authored by D. Molnár [109]. The principal difference with the codes above is that the reaction plane is not preserved in the two-body scattering. Another difference is that scattering between collision partners is not allowed until both particles have scattered with other particles. It should be noted that MPC has switches which make it possible to reproduce the choices described in ZPC and Gromit-*t*.

4. Gromit-τ: Another version of cascade/Boltzmann engine developed by the RTTC collaboration with collisions ordered by τ to be appropriate for ultra-relativistic collisions [137]. The spacetime points at which the two particles would scatter had the particles scattered simultaneously in the two-particle rest frame, x_1' and x_2', are used to generate two proper times, τ_1' and τ_2'. The average $\tau' = (\tau_1' + \tau_2')/2$ is then used for ordering. Both trajectories are altered when their proper time equals τ'. The reaction plane is preserved in the scattering and scattering between the same pair of particles is allowed after one of the particles has scattered with a third particle.

The initial condition is chosen to be a boost-invariant particle distribution as described in Subsection 3.2.2. The initial particles are confined to $|\eta| \leq 2$ and a circle of radius 5 fm in the transverse spatial coordinates. The simulation involved 2400 pions and 240 protons at a temperature of $T = 180$ MeV and $T = 165$ MeV, respectively, to roughly achieve consistency with spectra resulting from heavy ion collisions. The initial particle densities are 7.64 pions and 0.764 protons per fm^3. To be as simple as possible, constant cross sections are imposed independent of the species involved.

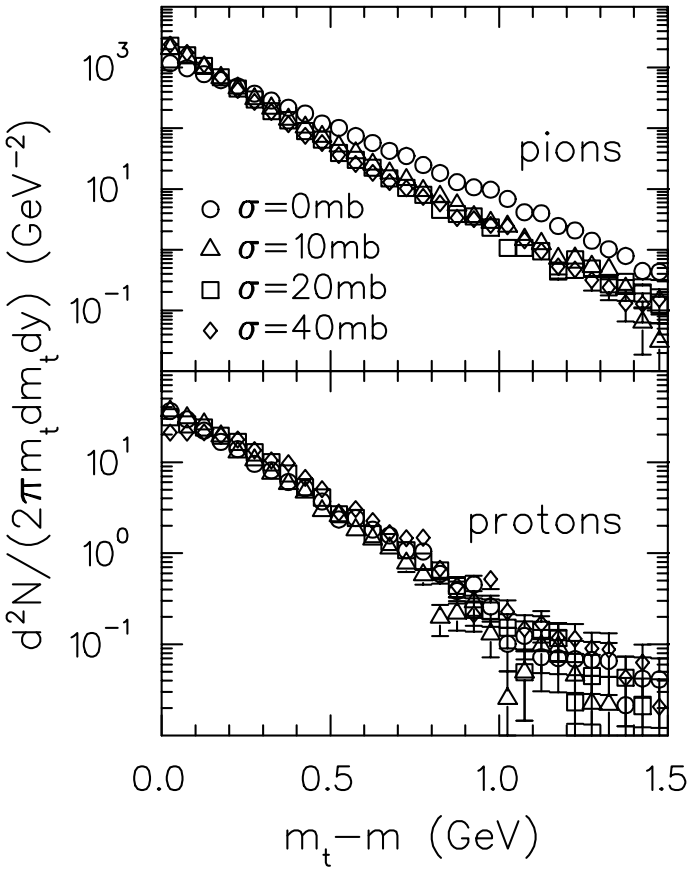

Figure 4.1: Transverse Mass Spectra from Gromit-τ are displayed for four cross sections.

The resulting transverse mass, $m_t = \sqrt{E^2 - p_z^2}$, spectra at mid-rapidity as calculated with Gromit-τ are shown in Figure 4.1 for four different cross sections, 0, 10, 20 and 40 mb. These calculations are performed with a sampling factor $\lambda = 32$. For larger cross sections, the pion spectra are cooler while the proton spectra are hardly altered. The difference would be more if the pion and proton distributions were initialized with identical temperatures.

Figure 4.2 displays spectra from Gromit-τ with σ =40 mb for four different sampling factors, $\lambda = 1, 2, 8$ and 32. The sensitivity to λ is remarkable. For small λ it appears that both the pion and proton spectra become hotter. Results converge for $\lambda \longrightarrow \infty$ as the $\lambda = 8$ and $\lambda = 32$ results are already barely distinguishable. In all the models investigated here, the final-state transverse energies are higher for small sampling factors. This reduction in cooling is attributed to viscous effects arising from finite-range interactions, as will be

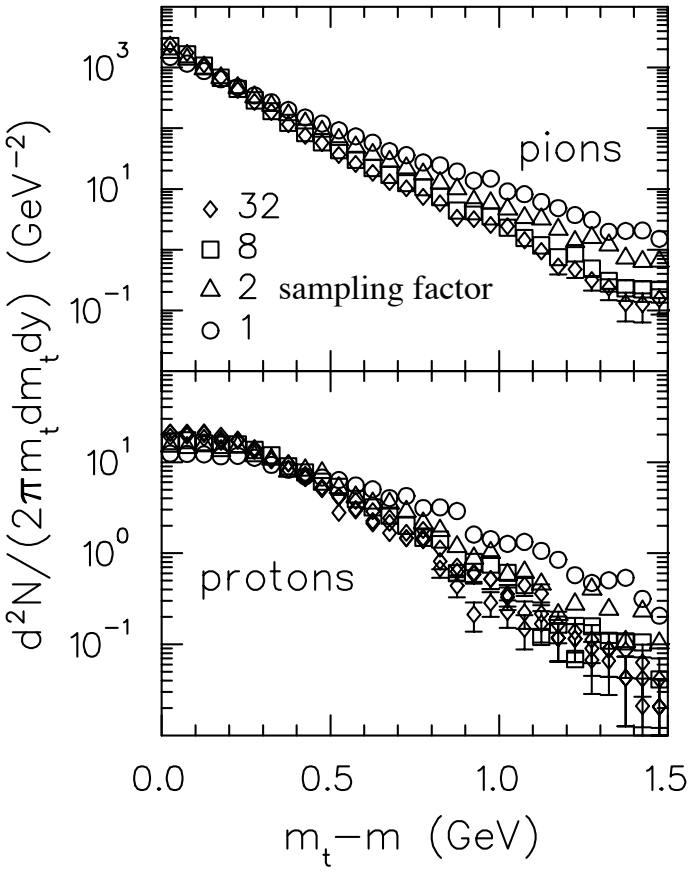

Figure 4.2: Spectra for pions and protons resulting from Gromit-τ with 40 mb cross sections for four sampling factors, $\lambda = 1, 2, 8, 32$.

discussed in Chapter 5.

In the upper panel of Figure 4.3 the resulting spectra from the four algorithms are displayed in the cascade limit. The slopes vary by approximately 20 MeV. Since the hadrons are initially separated by approximately 1/3 fm, while the interaction range is 1.1 fm, it is not surprising that the $\lambda = 1$ result is sensitive to the scattering algorithm. The same results are displayed in the lower panel of Figure 4.3 but with a high sampling factor, $\lambda = 16$. The various algorithms have converged.

For each algorithm the spectra fall significantly more steeply when produced with a higher sampling factor λ. This is especially true for the proton spectra, which suggests that radial flow is stronger in the cascade limit. Since the average transverse energy for pions

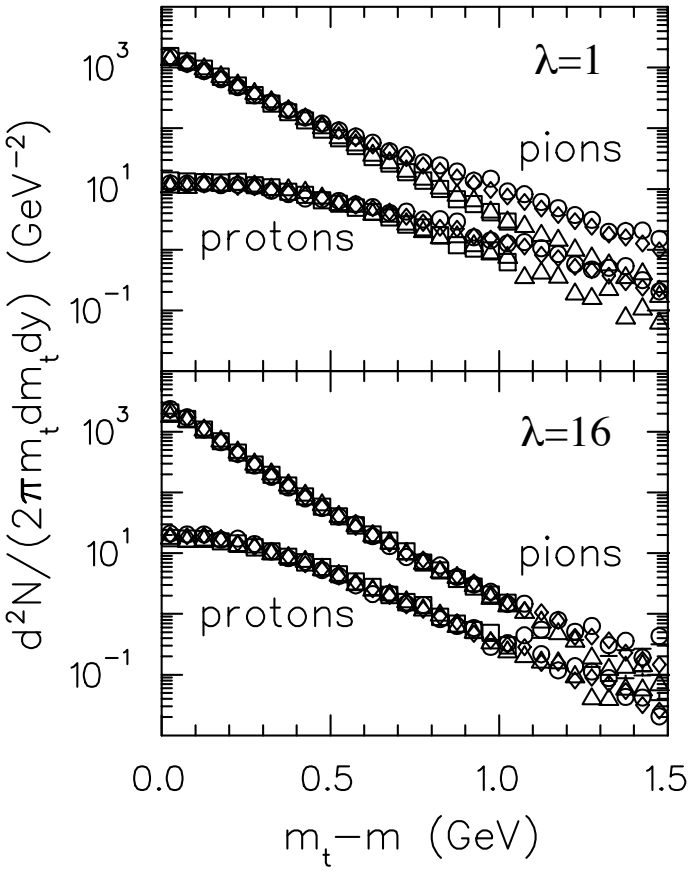

Figure 4.3: Spectra for pions and protons resulting from four models run with $\sigma = 40$ mb: (ZPC – squares, MPC – diamonds, Gromit-t – triangles, Gromit-τ – circles). In the upper panel calculations are performed with a sampling factor of 1, while in the lower panel each model used a sampling factor $\lambda = 16$. Due to different scattering algorithms, the models generated different results for $\lambda = 1$, while generating identical results for larger λ.

is also larger in the cascade limit, one can infer that longitudinal cooling is significantly suppressed through particles interacting at a finite range.

4.2 Elliptic Flow

The elliptical shape resulted in elliptic flow which is parameterized by the observable v_2.

$$v_2 = \langle \cos(2(\phi - \phi_0)) \rangle, \tag{4.1}$$

where ϕ_0 specifies the direction of the reaction plane which contains the short axis of the ellipse. Elliptic flow has been proposed as a means for determining the equation of state of

the matter at early times of a relativistic heavy-ion collision [117, 53, 121, 123, 142, 160, 4] and is, therefore, one of the most important observables in the research of relativistic heavy-ion collisions.

Recently, the inability of traditional microscopic models to reproduce the experimental elliptic-flow results from gold on gold collisions at $\sqrt{s_{NN}} = 130$ GeV [4] has stirred much recent theoretical research activity [145, 108, 18, 158, 147]. Some authors matched the experimentally measured elliptic flow with a Boltzmann-type model by increasing the model cross sections beyond physically conceivable values, which effectively mimics a hydrodynamical description [110, 111]. Other authors could produce an agreement to experimentally data by using a hydrodynamical model for the early stages of the collision and a microscopic transport model for the later stages [102, 93, 101].

4.2.1 Sensitivity to the Sampling Factor λ

Given the interest in elliptic flow, it is important to obtain an accurate calculation of elliptic flow from microscopic simulation. Of foremost importance is the study of sensitivities of elliptic flow to the sampling factor. For this study, the same model is adopted as in the previous section. The initial condition differs from that used previously in that the particles here are confined to an ellipse in the transverse direction with a major semi-axis of 5 fm and minor semi-axis of 2.5 fm to crudely account for the initial spatial anisotropy in a relativistic heavy-ion collision. In addition, cyclic boundary conditions in η are employed to simulate a truly boost-invariant system.

Both schemes for incorporating the sampling factor into a Monte Carlo simulation, which were introduced in Subsection 3.1.2, will be used when extracting the elliptic flow. In one scheme, the increase in the sampling factor by λ is countered by scaling the cross sections by $1/\lambda$ to maintain a constant collision rate, which is proportional to the product of density and cross section. Extracted elliptic flows are illustrated in Figure 4.4 for two cross

sections, 10 mb and 40 mb, and for four sampling factors. The results for 40 mb confirm both expectations about the effects of the sampling factor. First, observables, elliptic flow

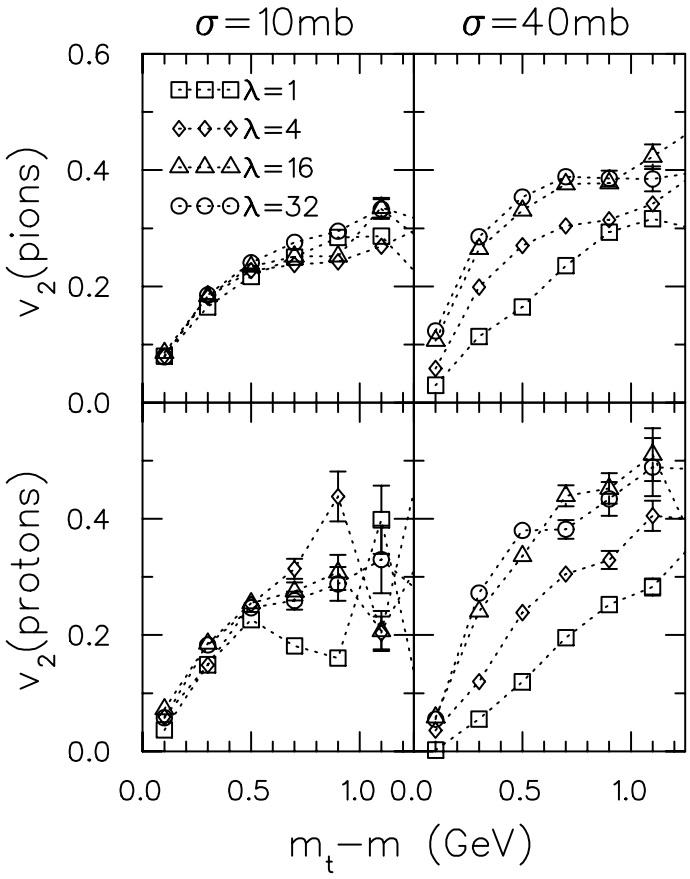

Figure 4.4: Elliptic flow is shown as a function of transverse energy for both pions and protons for several sampling factors. In this case the cross sections are scaled by a factor $1/\lambda$ to account for the over-sampling. The reduced flow resulting for calculations with small λ (larger cross sections) is attributed to viscous effects arising from the finite interaction range.

in this case, are sensitive to the sampling factor. This effect can be seen from Figure 3.2.2, where larger sampling factors lead to pronounced increases in elliptic flow. Second, the observables converge for large sampling factors. In this case, the results do not change significantly from $\lambda = 16$ to $\lambda = 32$, so that a sampling factor of $\lambda = 32$ already approaches the Boltzmann limit. The minimal change in the elliptic flow for 10 mb as a function of the sampling factor suggest that the source for the sensitivity to the sampling factor are linked to the range of the interaction. The interaction range decreases as the cross sections are

scaled by $1/\lambda$ in this scheme. Small sampling factors λ correspond to the largest interaction range, which may lead to a reduction in elliptic flow by homogenizing the collision region across larger distances.

This hypothesis is further examined by comparing the above results to the elliptic flow extracted with the second scheme for modeling the sampling factor. In this scheme, the cross section, and thus the interaction range, is left constant as λ is varied. Instead, only a fraction of $1/\lambda$ of all possible scatterings are executed to maintain a constant reaction rate. The elliptic flow extracted from this simulation proves to be insensitivity to λ as demonstrated in Figure 4.5. This result shows that the finite range of the interactions is

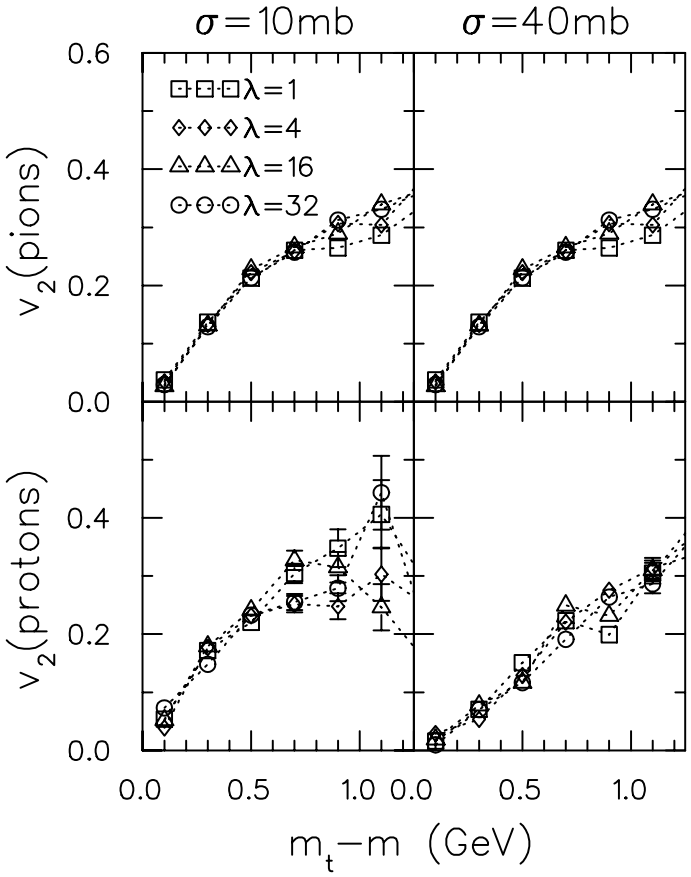

Figure 4.5: Elliptic flow is shown as a function of transverse energy for both pions and protons for several sampling factors, λ. The cross sections is not varied as λ is varied, but instead only a fraction $1/\lambda$ of the particles are scattered. The insensitivity to λ demonstrates that the Boltzmann limit is effectively realized, even for $\lambda = 1$.

indeed responsible for the sensitivity of the elliptic flow to the sampling factor, when the cross sections are scaled with $1/\lambda$. The explicit incorporation of finite-range interactions into a Boltzmann treatment and their link to viscous effects will be pursued further in Chapter 5.

4.2.2 Comparison to Experimental Data

Gromit is able to reproduce elliptic flow measured by the STAR collaboration [4] with a simplified model. The goal is not to provide a physically accurate description of a relativistic heavy-ion collision, but to examine whether the model assumptions in Gromit are consistent with physical principles. The simplified model includes only gluons that interact elastically with different energy-independent cross sections. Each gluon is converted to a pion via parton-hadron-duality with π^+, π^-, and π^0 being equally probable. The initial condition is obtained by a Glauber-type model [77, 101], in which the particle distribution is taken to be boost-invariant along the beam axis with the following transverse profile.

$$\frac{dN(\mathbf{x}_\perp)}{d\eta d\mathbf{x}_\perp^2} = \sigma T_A(\mathbf{x}_\perp + \mathbf{b}/2)\, T_A(\mathbf{x}_\perp - \mathbf{b}/2), \tag{4.2}$$

where σ is chosen to fit the required multiplicities and the thickness functions are defined as

$$T_A(\mathbf{x}_\perp) = \int dz\, \rho_A\left(\sqrt{z^2 + \mathbf{x}_\perp^2}\right). \tag{4.3}$$

The nuclear density distribution $\rho_A(r)$ is modeled by a Woods-Saxon (or two-parameter Fermi) form

$$\rho_A(r) = \frac{\rho_0}{1 + \exp\{(r-a)/b\}}, \tag{4.4}$$

where for any nucleus $\rho_0 = 0.16\text{fm}^{-3}$ and $a = (1.12A^{1/3} - 0.86A^{-1/3})$ fm and for the gold nucleus $A = 197$ and $b = 0.54$ fm .

This theoretical initial condition uses the impact parameter, whereas the STAR collaboration parameterizes the centrality of the collision by the particle multiplicity in the event,

The transverse profile in 4.2 has to be integrated over $\mathbf{x}_\perp$ to obtain a relation between mul-

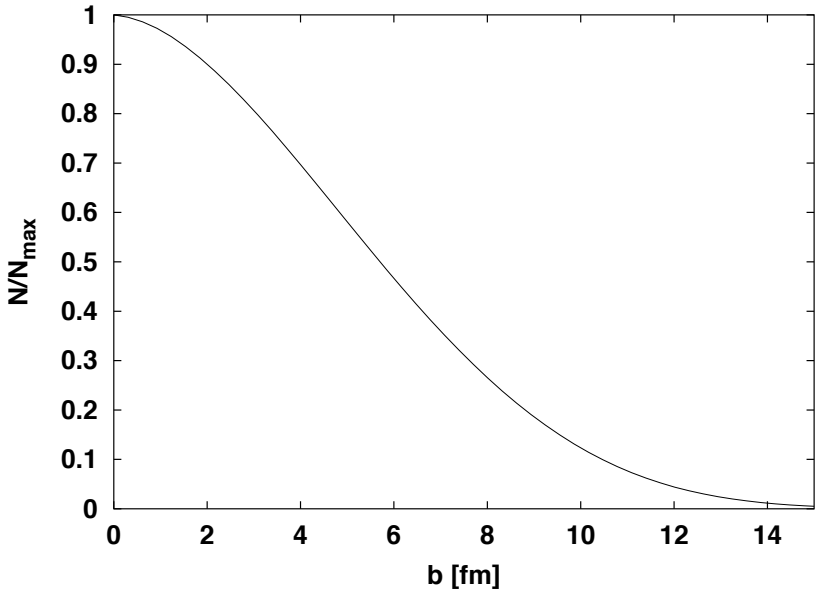

Figure 4.6: Relative multiplicity distribution as a function of impact parameter according to a Glauber-type model.

tiplicity and impact parameter, which is shown in Figure 4.6.

Monte Carlo simulations are performed with different values for the energy-independent cross section as well as different distributions for the differential cross section. A selection of these calculations are shown in Figure 4.7 with cross sections of 8 mb, 10 mb, and 40 mb and either s-wave or screened Rutherford differential cross section. Despite the simplicity of the employed model, the elliptic flow from the simulation with 8 mb, s-wave cross section describes the experimental data reasonably well. However, the purpose of this study is not to *fit* experimental data but rather to gain insight into the applicability of the Gromit framework introduced in the previous chapter.

It should be noted that the experimental values for the elliptic flow shown in Figure 4.7 are in the process of being revised [5]. This new analysis became necessary after novel theoretical insight by Borghini, Dinh, and Ollitrault indicated that nonflow effects contribute substantially to the elliptic flow determined experimentally and have to be removed

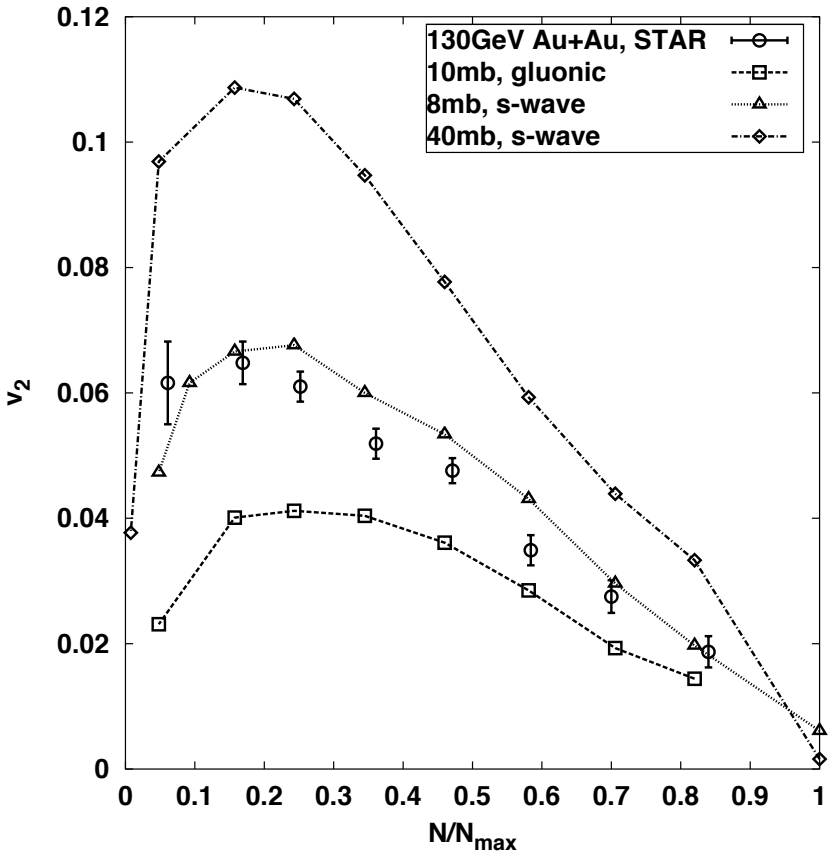

Figure 4.7: Comparison of elliptic flow from a Gromit model to experimental data from Au+Au at 130 A GeV measured by the STAR collaboration for some choices of cross sections. The experimental results are shown without systematic errors. The calculation were performed with a sampling factor of $\lambda = 32$.

[36, 35, 34]. The new results have not been published yet, but the improved analysis are expected to yield slightly smaller values for the elliptic flow for peripheral collisions. The changes would have little impact on the discussion presented here.

4.2.3 Elliptic Flow in the Initial State

So far, theoretical studies on elliptic flow generally assumed for simplicity that the momentum distribution in the initial state was isotropic, or in other words, that there was no elliptic flow in the initial condition. This, however, need not be the case in a relativistic heavy-ion collision and will be examined with a Glauber-type model as explained previ-

ously in Subsection 4.2.2.

In a Glauber-type model, the nucleus-nucleus collision is assumed to be a superposition of many nucleon-nucleon collisions. A certain angular momentum is associated with each such collision between a pair of nucleons. The sum of the angular momenta would vanish if the distance vector between the two initial nucleons at positions $\mathbf{x}_1$ and $\mathbf{x}_2$,

$$\Delta\mathbf{r} = \mathbf{x}_1 - \mathbf{x}_2, \tag{4.5}$$

were distributed isotropically. This condition can be inspected by examining the orientation of the distance vector, which can be quantified by the angle between the distance vector and the x-axis, $\angle(\Delta\mathbf{r}, \mathbf{e}_x)$. The average over the cosine of twice the orientation angle

$$\left\langle \cos\left(2\,\angle(\Delta\mathbf{r}, \mathbf{e}_x)\right)\right\rangle, \tag{4.6}$$

would vanish if the distance vector was distributed isotropically. Figure 4.8 displays that average for the adopted model as a function of impact parameter. As expected, the distri-

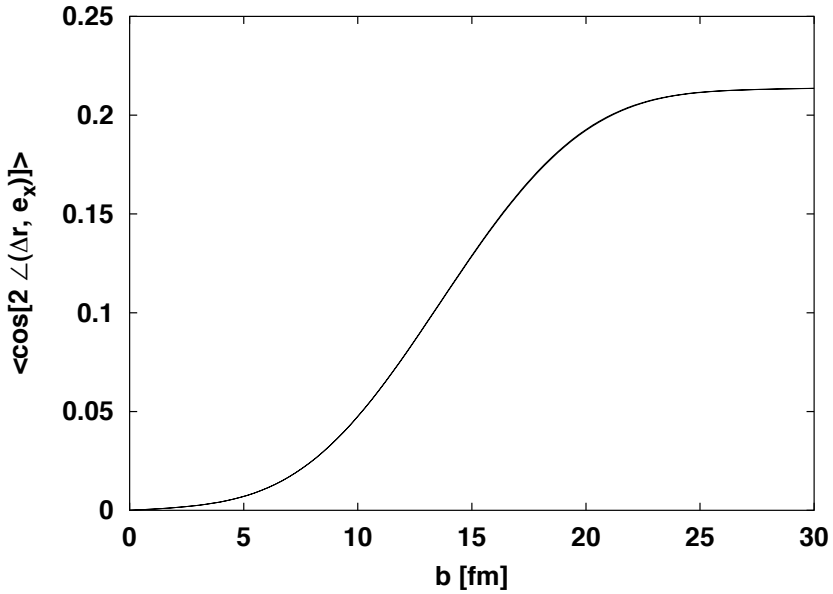

Figure 4.8: Anisotropy in the distribution of the distance vector in the initial condition according to a Glauber-type model of a relativistic heavy-ion collision.

bution of the distance vector is isotropic for central collisions, however, that distribution

becomes more anisotropic as the impact parameter increases. The anisotropy in the distribution of the distance vector yields a net angular momentum that might lead to momentum anisotropy in the initial state of relativistic heavy-ion collision.

In addition, the elementary nucleon-nucleon collision employed in the model for the initial state might contain elliptic flow. This aspect has neither been addressed theoretically nor experimentally up to this point. Yet, rather than seeking to establish the existence or source of elliptic flow in the initial state of a relativistic heavy-ion collision, this study will investigate whether and how the elliptic flow in the initial state affects the elliptic flow in the final state.

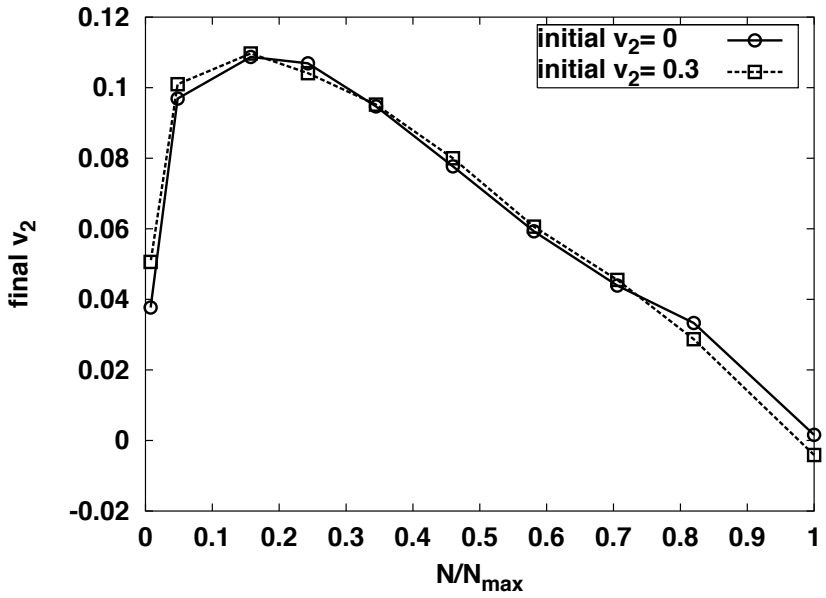

Figure 4.9: Elliptic flow in the final state as a function of centrality with and without elliptic flow in the initial state. The initial condition and dynamics of these simulations are described in the text in Subsection 4.2.2. The sampling factor is $\lambda = 32$, the cross section 40 mb.

The elliptic flow is calculated from a simulation similar to the one specified in Subsection 4.2.2 with and without initial elliptic flow. The calculations are carried out for a range of values for cross sections and initial elliptic flow and show a consistent picture. For simplicity only the calculation with those parameters will be presented that promise the most

visible effect. The results demonstrate that even with exaggerated, large values, 40 mb for the cross sections and 30% for the initial elliptic flow, the elliptic flow in the final state is not affected significantly, as shown in Figure 4.9.

4.3 Regeneration of ρ Mesons

So far in this thesis, the Gromit framework has been employed only for simple models that included one or two particle types and elastic collisions with energy-independent cross sections. To move further toward a more realistic model, the particles that are most commonly found in a relativistic heavy-ion collision are included. The following particles and resonances are included: the meson pseudo-scalar and vector octets and singlets as well as the baryon octet and decuplet along with their anti-particles. These particles are allowed to scatter elastically with cross sections according to the additive quark model (AQM). For the included resonances the known decays are incorporated, as are the corresponding inverse resonance formations. This model is then used to gain insight into the regeneration of ρ mesons in the collision dynamics. This insight can be used in the search for the chiral restoration phase transition.

A possible signature of chiral restoration and rebreaking are anomalous isospin fluctuations, which were mentioned in Chapter 2. Another indicator for the restoration of chiral symmetry is derived from a predicted consequence of this phase transition. Resonance mass distributions are believed to broaden and shift toward lower invariant mass. The ρ meson is a candidate for a probing this effect. It has a lifetime on the order of 1 fm/c and is, therefore, sensitive to the rapidly changing environment in a relativistic heavy-ion collision, which is though to last on the order of 10 fm/c at RHIC energies.

The ρ meson has a dominant decay branch into two pions. These are not able to escape the collision region without further collisions, when emitted during an early stage

when hadron densities are high. Subsequent collisions erase the information that the pions stored about the decayed ρ, which suppresses the experimental signatures of the ρ mesons. Nonetheless, at later stages of the collision, when densities are significantly lower, the pions from ρ meson decays are able to exit the collision region without further interactions. These pions can then be used to deduce the properties of ρ mesons at lower densities.

There are other ρ decay channels into electron and muon pairs with respective branching ratios of 4.5×10^{-5} and 4.6×10^{-5}. Electrons and muons have a high probability of leaving the early, high-density phase unscathed, as their cross section with hadrons is relatively small. It is, therefore, possible to experimentally determine properties of the ρ meson at high densities from decay leptons. The small numbers of leptons produced in ρ mesons decays complicate their use in the experimental extraction of ρ signatures. This task, however, may be more feasible as there are indications that the branching ratios of the ρ meson decay into leptons are enhanced under the conditions found in the core of the collision region. Consequently, the properties of the ρ meson under different conditions like temperature and density can be inferred from analyses of the different decay channels. Consequently, the properties of the ρ meson under different conditions like temperature and density can be inferred from analyses of the different decay channels.

The short lifetime of the ρ meson that makes it possible for it to probe a small range of temperature in the collision region might also pose a problem. The ρ mesons from the early stages of the collision decay exponentially, leaving few surviving resonances to probe the later stages of the collision. This depletion might, however, be compensated for by the formation of new ρ mesons in the $2\pi \rightarrow \rho$ reaction. This process is referred to as regeneration. The above-described model is employed to investigate this regeneration quantitatively. The simulations will be performed with collisions included and blocked to illustrate the effect of the ρ meson regeneration.

The parameters of the model are chosen to provide realistic conditions. In the initial condition, the particles are distributed according to the boost-invariant Jüttner distribution, given in Eq. (3.12), with initial local temperature $T_{\rm local} = 278$ MeV at $\tau_0 = 1$ fm/c. The initial temperature is determined such that in a grand-canonical ensemble $dN/dy|_{y=0} \approx 750$, the value measured at RHIC. In coordinate space the particles are uniformly distributed over a cylinder with radius 5 fm and $|\eta| < 1$. To make maximum use of boost-invariance, the mesh in Bjorken coordinates are employed with periodic boundary conditions in η. The simulations are performed with a sampling factor of $\lambda = 10$.

In the absence of interactions, the initial ρ mesons follow the usual exponential decay law, as shown in Figure 4.10. The decay rate tail off after $\tau \approx 5$ fm/c and is insufficient to

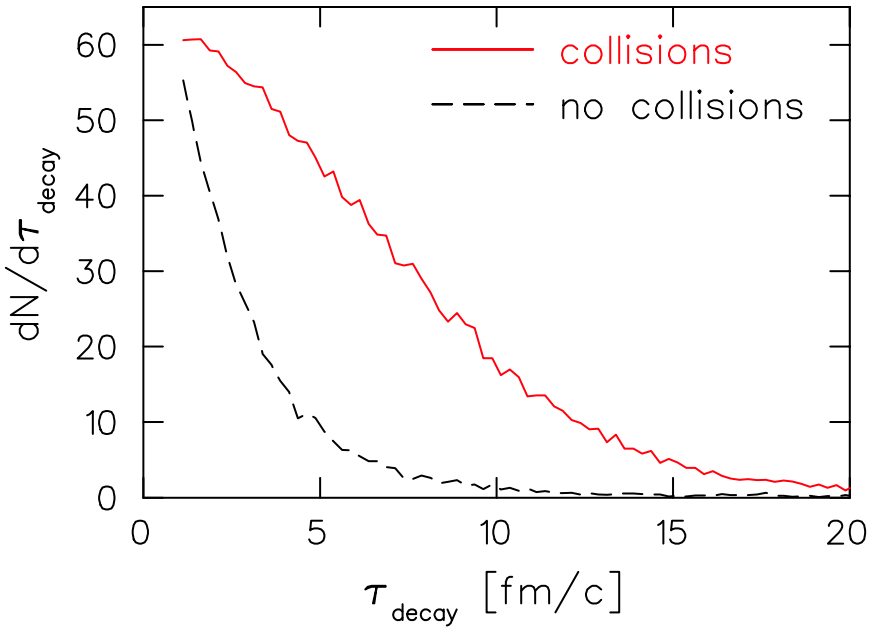

Figure 4.10: Distribution of τ's at which the ρ's decayed with and without collisions.

sample the entire evolution of the collision. On the other hand, inclusion of the $2\pi \to \rho$ reaction among other interactions leads to creation of ρ's throughout the evolution of the collision. The decay of these collision-produced ρ mesons take place at a later time and alter the exponential decay rate, demonstrated in Figure 4.10. The decay rate remains sufficiently high even at times well past 10 fm/c and supplies sufficient probes for the latest

stages of the collision. This shows conclusively that the ρ meson can be used as a probe for all stages of the collision. Experimental work is under way to extract in-medium resonance properties.

The model can also be used to gain insight about how the regeneration of ρ mesons might help in the search for the QGP. If no QGP was formed in the early, hot and dense phase of the relativistic heavy-ion collision, the collision region would mainly consist of hadrons. In this case, more ρ mesons would be regenerated than in a cocktail of overlapping nucleon-nucleon collisions due to the larger number of collisions between hadrons. As mentioned before, the number and properties of ρ mesons in the early stage of the collision can be experimentally determined from the leptonic decay branch of the ρ meson. To investigate whether indeed more ρ mesons are regenerated through hadronic rescattering in a relativistic heavy-ion collision, the same model as above is used to calculate the mass distribution of all ρ mesons that were created throughout the event. The calculation without collisions shown in Figure 4.11 represents the result expected for a cocktail of nucleon-

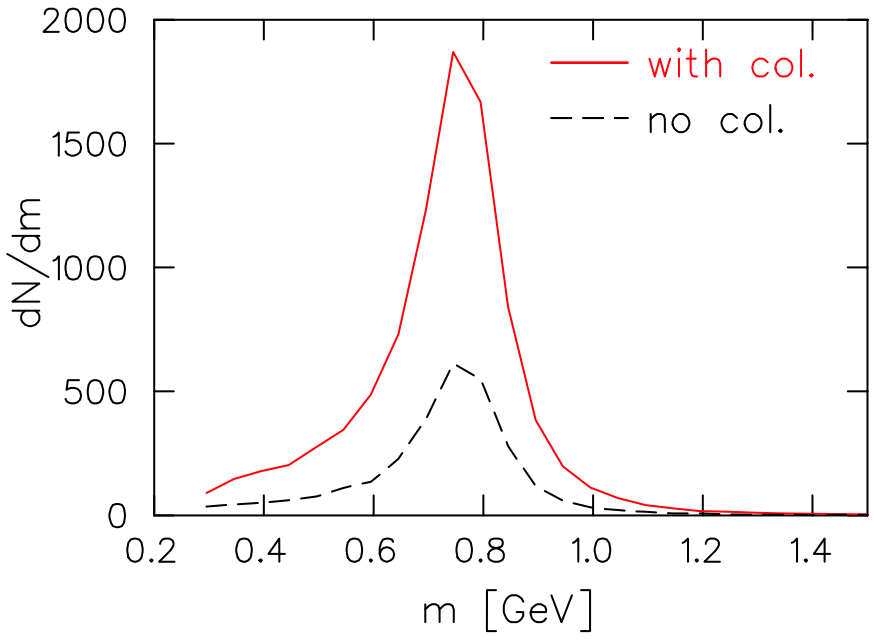

Figure 4.11: Distribution of ρ masses integrated over the entire collision history with and without collisions.

nucleon collisions. The distribution is entirely determined by the Breit-Wigner form of the spectral function for the resonance mass given in Eq. (3.14). As expected, the mass distribution receives significant contributions from $2\pi \rightarrow \rho$ formation processes, when collisions are included. In the Gromit framework, the resonance formation cross sections explicitly contain a Breit-Wigner distribution to reproduce the resonance production correctly, which is confirmed by the mass distribution displayed in Figure 4.11. The resonance formation cross sections, however, do not account for in-medium modifications to the resonances and, therefore, lack the shifts and broadening effects referred to earlier in this discussion.

Evidently, inclusion of collisions in the system affects other particles as well. For instance, light particles in the final state are colder when there are collisions, as can be inferred from the pion spectra shown in Figure 4.12. The temperature can be extracted from

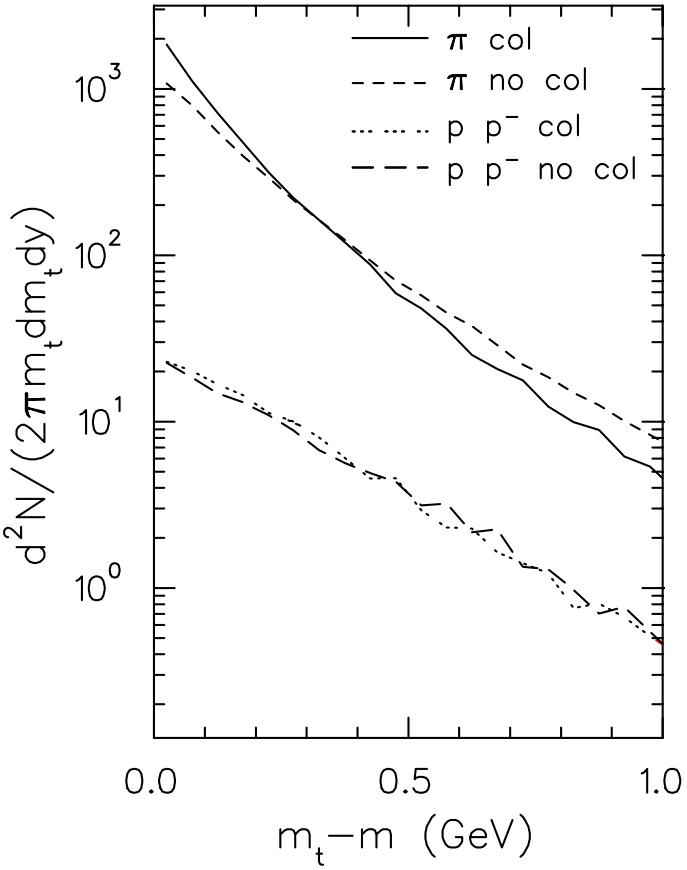

Figure 4.12: Transverse mass distribution for pions and combined proton and anti-protons with and without collisions.

the slopes of the particle spectra as they are proportional to the inverse temperature. Figure 4.12 also indicates that the temperatures of heavier particles like protons are not affected as much by the inclusion of binary collisions. This is a result of the increase in the average transverse energy of protons relative to that of the pions due to the transverse expansion. This increase compensates for the decrease due to the work performed on the longitudinal expansion, which affects all particles.

Chapter 5

Viscosities from Finite-Range Interactions

A principal goal of relativistic heavy ion collisions is to experimentally discern bulk properties of the excited vacuum. To accomplish this aim it is imperative that the implications of the finite size and lifetime of the global reaction are understood. Two microscopic length scales govern the importance of finite-size effects, the mean free path and the range of interaction. Microscopic models based on the Boltzmann equation, easily incorporate the effects of a finite mean free path. Such effects can be linked to viscous terms in analogous hydrodynamic descriptions.

In intermediate-energy collisions, where excitation energies are tens of MeV per nucleon, the role of the finite range to the strong interaction has been studied in its relation to the surface energy of nuclear matter. In such Boltzmann descriptions the binding energy of nuclear matter is introduced via the mean field, with the coarseness of the mean field mesh being adjusted so that the effect of the interaction range is effectively tuned to reproduce the surface energy of nuclear matter. In nonrelativistic molecular dynamics, the effects of hard-sphere interactions have also been investigated. In this case the size of the spheres represents a length scale which can strongly affect bulk properties of the matter at high density. However, in the context of a Boltzmann description, where n-body correlations are

explicitly neglected, the effects of a finite range inherent to the scattering kernel have not been analyzed for their impact on final-state observables.

It is the goal of this study to ascertain the importance of this second length scale in high-energy collisions. By varying the interaction range in the scattering kernel, while leaving the mean free path unchanged, the consequences of a nonzero interaction range are studied. It is demonstrated that a finite interaction range contributes to viscous terms in a manner similar to the finite mean free path, but with different dependencies with respect to density and temperature. The finite range of the interaction is found to affect the evolution of heavy-ion reactions and to alter final-state observables, especially elliptic flow.

After formally reviewing the collision kernel in the Boltzmann equation, it is shown how viscosities arise from the interaction range. the finite range. Viscous heating is then explained by analyzing the collision kernel. In particular, a comparison is presented between the heating derived from analysis of the collision kernel and the heating observed in a simple simulation.

5.1 Connecting Viscosities to Finite-Range Interactions

5.1.1 The Role of the Collision Kernel in Boltzmann Descriptions

The Boltzmann equation can be expressed,

$$\begin{aligned}\frac{\partial}{\partial t}f(\mathbf{p},\mathbf{r},t)+\mathbf{v}_p\cdot\nabla f(\mathbf{p},\mathbf{r},t)+\mathbf{F}(\mathbf{r},t)\cdot\nabla_p f(\mathbf{p},\mathbf{r},t)=\int d^3q d^3q' d^3p' d^3r' dt' \\ \times\{f(\mathbf{q},\mathbf{r},t)f(\mathbf{q}',\mathbf{r}',t')\mathcal{K}(\mathbf{r}-\mathbf{r}',t-t';\mathbf{q},\mathbf{q}';\mathbf{p},\mathbf{p}') \\ -f(\mathbf{p},\mathbf{r},t)f(\mathbf{p}',\mathbf{r}',t')\mathcal{K}(\mathbf{r}-\mathbf{r}',t-t';\mathbf{p},\mathbf{p}';\mathbf{q},\mathbf{q}')\},\end{aligned} \tag{5.1}$$

where f is the phase space density and $\mathbf{F}$ is the force $d\mathbf{p}/dt$ felt by a particle at position $\mathbf{r}$. The collision kernel $\mathcal{K}(\mathbf{r}-\mathbf{r}',t-t';\mathbf{q},\mathbf{q}';\mathbf{p},\mathbf{p}')$ describes the differential probability for scattering a pair of particles separated in spacetime by $x-x'$ with initial momenta $\mathbf{q}$ and

$\mathbf{q}'$ into final states with momenta $\mathbf{p}$ and $\mathbf{p}'$. The range of the collision kernel in coordinate space is the subject of this study.

Integrating over the collision kernel should yield the cross section,

$$\int d^3r'dt'\mathcal{K}(\mathbf{r}-\mathbf{r}',t-t';\mathbf{q},\mathbf{q}';\mathbf{p},\mathbf{p}') = \frac{1}{(2\pi)^3}\frac{d\sigma}{d^3p_{\rm rel}}v_{\rm rel}\delta^3(\mathbf{p}+\mathbf{p}'-\mathbf{q}-\mathbf{q}'), \qquad (5.2)$$

where $\mathbf{p}_{\rm rel}$ is the relative momentum of the outgoing pair $(\mathbf{p}-\mathbf{p}')/2$. By inspection of Eq. (5.2), it can be seen that the coordinate-space dependence of $\mathcal{K}$ appears rather arbitrary as long as it integrates to the free-space cross section. Indeed, results at low density, where particles interact only pairwise, are unaffected by the form of $\mathcal{K}$ as long as the range is much less than the mean free path and much less than the characteristic dimensions of the reaction volume.

Any nonzero extent of the collision kernel leads to problems with super-luminar transport. However, these problems are easily defeated by restricting the kernel to being local, i.e.,

$$\mathcal{K}(\mathbf{r}-\mathbf{r}',t-t';\mathbf{q},\mathbf{q}';\mathbf{p},\mathbf{p}') = \frac{1}{(2\pi)^3}\delta^3(\mathbf{r}-\mathbf{r}')\delta(t-t')\cdot\frac{d\sigma}{d^3\mathbf{p}_{\rm rel}}v_{\rm rel}\delta^3(\mathbf{p}+\mathbf{p}'-\mathbf{q}-\mathbf{q}'). \quad (5.3)$$

The Boltzmann equation can now be written in a manifestly covariant form.

$$\left(u^\mu_{\mathbf{p}}\partial_\mu + F^\mu\frac{\partial}{\partial p^\mu}\right)f(\mathbf{p},\mathbf{r},t) = \frac{1}{(2\pi)^3}\int\frac{d^3q'}{E_{q'}}\frac{d^3q}{E_q} \qquad (5.4)$$

$$\left\{\sqrt{(q\cdot q')^2-m^4}\frac{d\sigma}{d^3\tilde{\mathbf{p}}_{\rm rel}}f(\mathbf{q},\mathbf{r},t)f(\mathbf{q}',\mathbf{r},t) - \sqrt{(p\cdot p')^2-m^4}\frac{d\sigma}{d^3\tilde{\mathbf{q}}_{\rm rel}}f(\mathbf{p},\mathbf{r},t)f(\mathbf{p}',\mathbf{r},t)\right\}$$

Here, $u_{\mathbf{p}}$ is the four-velocity of a particle with momentum $\mathbf{p}$, F^μ is the force $dp^\mu/d\tau$, and $\tilde{\mathbf{p}}_{\rm rel}$ is the relative momentum of the outgoing particles in the center of mass.

5.1.2 Effective Viscosities from Finite-Range Interactions

The interaction over a finite range contributes to the shear viscosity, η, the bulk viscosity, ζ, and the thermal conductivity, χ. The range of the interaction is related to all three

coefficients. In order to make this connection, two particles are considered which scatter from one another, separated by a distance $\mathbf{r} = \mathbf{r}_2 - \mathbf{r}_1$. Combining this finite separation with the velocity gradient, it can be seen that the first particle interacts with particles which have a higher average energy. By evaluating the rate at which energy is transferred to the first particle from colliding with more energetic particles, an expression is found for the rate at which heat is deposited to the region defined by $\mathbf{r}_1$. By comparing to analogous expressions from hydrodynamics, expressions can be derived for all three viscous terms in terms of the interaction range, $r = |\mathbf{r}_1 - \mathbf{r}_2|$, the density n, and the collision rate Γ.

Choosing a reference frame such that the velocity of bulk matter at the location of the first particle is zero, the collective velocity at $\mathbf{r}_2$ is

$$v_i = A_{ij} r_j, \;\; A_{ij} = \frac{\partial v_i}{\partial r_j}. \tag{5.5}$$

For an elastic collision where two particles of identical mass simultaneously change their momenta, the radial components of the momenta must be interchanged by the collision if energy, linear momentum and angular momentum are to be conserved. Physically, this corresponds to the scattering from the interior or exterior surface of a hard sphere. The average energy change of the first particle is then

$$\langle \delta E_1 \rangle = \langle E_{2,r} \rangle - \langle E_{1,r} \rangle = \frac{m}{2} \langle (\mathbf{v} \cdot \hat{r})^2 \rangle. \tag{5.6}$$

The mass term m is not to be taken literally as the mass of the particles, since the averaging may include factors of the velocity to account for the flux or it may have a complicated form to accommodate a desired differential cross section. For relativistic motion, the mass might incorporate the lateral motion of the particles. Writing $\langle \delta E_1 \rangle$ in terms of A,

$$\langle \delta E_1 \rangle = \frac{m}{2r^2} \langle (r_i A_{ij} r_j)^2 \rangle. \tag{5.7}$$

The average over the directions of $\mathbf{r}$ can be performed using the identity,

$$A_{ij} A_{kl} \langle r_i r_j r_k r_l \rangle = A_{ij} A_{kl} \frac{r^4}{15} \left(\delta_{ij}\delta_{kl} + \delta_{ik}\delta_{jl} + \delta_{il}\delta_{jk} \right). \tag{5.8}$$

Then, $\langle \delta E_1 \rangle$ can be expressed in terms of A and r.

$$\langle \delta E_1 \rangle = \frac{mr^2}{30}\left((\mathrm{Tr}A)^2 + \frac{1}{2}\sum_{ij}(A_{ij}+A_{ji})^2 \right) \tag{5.9}$$

$$= \frac{mr^2}{30}\left[(\nabla \cdot v)^2 + \frac{1}{2}\sum_{ij}\left(\frac{\partial v_i}{\partial r_j} + \frac{\partial v_j}{\partial r_i} \right)^2 \right].$$

The rate at which the entropy increases due to these interactions is given by the density multiplied by the rate at which collisions deposit energy nonlocally,

$$\partial \cdot S = \frac{n\Gamma}{T}\langle \delta E_1 \rangle \tag{5.10}$$

$$= \frac{n\Gamma m r^2}{30T}\left[(\nabla \cdot v)^2 + \frac{1}{2}\sum_{ij}\left(\frac{\partial v_i}{\partial r_j} + \frac{\partial v_j}{\partial r_i} \right)^2 \right].$$

Here, Γ is the collision rate experienced by a single particle and n is the density.

It is notable that only the symmetric part of A contributes to $\langle \delta E_1 \rangle$. This owes itself to conservation of angular momentum which forbids rotational motion from being transferred between particles. In fact, if an expression for $\langle \delta E_1 \rangle$ had been derived using v^2 instead of v_r^2, the resulting expression would have included the odd parts of A which would correspond to rotational motion, $\nabla \times \mathbf{v}$. These terms would have no hydrodynamical analog as they would have reflected a violation of angular momentum conservation.

Analogous expressions for Eq. (5.10) are now provided in the language of hydrodynamics. The expression for entropy production [152, p. 55] in terms of velocity gradients is

$$\partial \cdot S = \frac{\eta}{2T}\sum_{ij}\left(\frac{\partial v_i}{\partial x_j} + \frac{\partial v_j}{\partial x_i} - \frac{2}{3}\delta_{ij}\nabla \cdot \mathbf{v} \right)^2 + \frac{\zeta}{T}(\nabla \cdot \mathbf{v})^2 + \frac{\chi}{T^2}(\nabla T)^2. \tag{5.11}$$

The coefficients can be extracted by comparing Eq. (5.10) to the first two terms in 5.11.

$$\eta = \frac{mn\Gamma r^2}{30} \tag{5.12}$$

$$\zeta = \frac{mn\Gamma r^2}{18}. \tag{5.13}$$

Applying similar reasoning, an expression for the thermal conductivity can be derived as well. First, the temperature gradient is related to the energy flow. Again, particles are considered to be separated by $\mathbf{r}$. If collisions occur between two particles at locations with different temperatures, the average energy exchanged is

$$\delta E_1 = \frac{1}{2} C_r \mathbf{r} \cdot \nabla T. \tag{5.14}$$

Here C_r represents the change in radial kinetic energy per particle per change in temperature,

$$C_r = \frac{\partial}{\partial T} E_r. \tag{5.15}$$

In the nonrelativistic limit, $C_r = 1/2$.

Since the exchange corresponds to moving an energy a finite distance over an effective time given by the collision rate, the average momentum density can be defined in terms of the energy flow.

$$M_i = -\frac{n\Gamma C_r}{4} \langle r_i r_j \rangle \frac{\partial T}{\partial x_j}. \tag{5.16}$$

$$\mathbf{M} = -\frac{n\Gamma C_r r^2}{12} \nabla T \tag{5.17}$$

An extra factor of $1/2$ was added to correct for double counting the collisions.

The energy flow can be related to the entropy production,

$$\frac{dS}{dt} = \int d^3x \frac{1}{T} \frac{\partial \varepsilon}{\partial t} \tag{5.18}$$

$$= -\int d^3x \frac{1}{T} \nabla \cdot \mathbf{M} \tag{5.19}$$

$$= \int d^3x \frac{n\Gamma C_r r^2}{12T^2} (\nabla T)^2, \tag{5.20}$$

where the continuity equation has been applied. This can be compared with the last term in Eq. (5.11) to obtain the thermal conductivity χ.

$$\chi = \frac{n\Gamma C_r r^2}{12}. \tag{5.21}$$

The forms for the three coefficients, η, ζ and χ, fundamentally differ from the forms that result from considering a nonzero mean free path ℓ. The viscous coefficients that result from finite ℓ are independent of density and scale inversely with the cross section [152]. The coefficients arising from a nonzero interaction range r scale as the square of the density and are proportional to the cross section. Thus, nonlocal interactions provide viscosities that are important in wholly different conditions than those where the finite mean free path plays an important role. For a rapidly expanding system, finite-range interactions play an important role when the interaction range multiplied by the velocity gradient provides velocities of similar magnitudes to local thermal velocities. Such conditions exist in the first one fm/c of highly relativistic hadronic collisions.

The expressions here derive from a very specific picture, nonrelativistic particles moving on straight-line trajectories punctuated by sharp collisions when the separation equals r. However, all interaction at a finite distance should result in viscous behavior. Relating the distance r to the cross section might involve a detailed microscopic evaluation of the collision kernel. This is especially true for relativistic motion. Despite the complications, the distance r^2 can indeed be expected to be of similar magnitude to collision cross sections. It would be interesting to discern whether the ratio between the shear and bulk viscosities varies for different scattering models.

5.2 Analyzing the Collision Kernel

In Subsection 5.1.2 a finite range of interaction, characterized by a length scale, r, was shown to generate viscous behavior. This length scale is determined by the cross section, $r^2 \sim \sigma/\pi$, but the constant of proportionality is not trivially determined and can depend on seemingly arbitrary aspects of scattering algorithms. In the following subsection, we illustrate how viscous heating can also be directly related to the collision kernel by considering

a simple example of one-dimensional expansion with a Bjorken spacetime geometry. In the subsequent subsection predictions based on the form of the scattering kernel are compared with results from simulations based on the same kernel.

5.2.1 Viscous Heating in a Bjorken Expansion

As a simple example, a one-dimensionally boost-invariant system of infinite extent in all dimensions is considered again. The number of particles is kept fixed such that the density scales inversely with τ,

$$n(\tau) = \frac{1}{\tau} d^2N/(dA d\eta). \tag{5.22}$$

where the number of particles per area per rapidity interval, $d^2N/(dA d\eta)$, is fixed. To simplify matters particles are considered massless.

Here, the rate at which a particle at $\eta = 0$ has collisions with other particles, $dN_c/d\tau$, and the rate at which it gains or loses energy from such collisions, $d\langle E_1\rangle/d\tau$, are calculated. The particles are assumed to be in local thermal equilibrium, and the collision kernel is analyzed to determine the rates.

Referring to the colliding partners with the subscript '2', the collision and heating rates per particle are

$$\frac{dN_c}{d\tau} = 2\pi \frac{d^2N}{dA\, d\eta} \int d\eta_2\, r_2\, dr_2\, d^3p_2\; \delta(\tau_c - \tau)\; \Theta\left(\frac{\sigma}{\pi} - b^2\right) \frac{d^3N}{d^3p_2}, \tag{5.23}$$

$$\frac{d\langle E_1\rangle}{d\tau} = 2\pi \frac{d^2N}{dA\, d\eta} \int d\eta_2\, r_2\, dr_2\, d^3p_2\; \delta(\tau_c - \tau)\; \Theta\left(\frac{\sigma}{\pi} - b^2\right) \delta E_1 \frac{d^3N}{d^3p_2}. \tag{5.24}$$

Here, δE_1 is the average change in energy of the particle '1' due to the collision and r_2 and η_2 describe the position of the second particle. The impact parameter for the two-particle collision is b and τ_c is the collision time.

The strategy employed here is to calculate the collision time, τ_c. The first particle is at a position $x_1 = (\tau, 0, 0, 0)$ with four momentum p_1. The second particle is at a position

$x_2 = (\tau\cosh\eta_2, r_2, 0, \tau\sinh\eta_2)$, with a four-momentum p_2. Once τ_c is understood in terms of r_2, η_2, p_1 and p_2, the delta function can be replaced in the expression above,

$$\delta(\tau_c - \tau) \rightarrow \delta(r_c - r_2)\frac{\partial r_c}{\partial \tau_c}, \tag{5.25}$$

where r_c is the position required to make the collision occur at τ. By substituting the delta function with r_c for the delta function with τ_c, the integrals in Eq. (5.23) and Eq. (5.24) can be simplified and solved numerically.

The first step that must be performed is to find τ_c in terms of r. The prescription for finding τ_c is somewhat arbitrary due to covariance issues as discussed in 3.2.5.2. A prescription must be arbitrarily chosen to find τ_c in terms of x_1' and x_2'. For the purposes of this study, the prescription according to Eq. (3.51) is employed to simplify the algebra. Using this choice,

$$\begin{aligned}
\tau_c^2 &= \tau^2 + \frac{C_0 r'^2 + 2C_1 r' + C_2}{2} \\
C_0 &= \gamma_1^2 p_{1\perp}^2 + \gamma_2^2 p_{2\perp}^2 \\
C_1 &= \gamma_1\alpha_1 + \delta_1\gamma_1 p_{1\perp}^2 + \gamma_2\alpha_2 + \delta_2\gamma_2 p_{2\perp}^2 \\
C_2 &= \delta_1^2 p_{1\perp}^2 + 2\delta_1\alpha_1 + \delta_2^2 p_{2\perp}^2 + 2\delta_2\alpha_2
\end{aligned} \tag{5.26}$$

The coefficients are defined

$$\begin{aligned}
\alpha_1 = E_1 t - p_{1,z} z\ ,\ \alpha_2 = E_2 t + p_{2,z} z \\
\delta_1 = 2z p_{2,z}/(p_1 \cdot p_2)\ ,\ \delta_2 = -2z p_{1,z}/(p_1 \cdot p_2) \\
\gamma_1 = 2p_{2,x}/(p_1 \cdot p_2)\ ,\ \gamma_2 = -2p_{1,x}/(p_1 \cdot p_2)
\end{aligned} \tag{5.27}$$

Here t, r and z are the positions describing the first particle in a frame where the particles are centered about $\eta = 0$ and $r = 0$.

$$\eta' = \frac{\eta_2}{2},\ t = \tau\cosh\eta',\ z = -\tau\sinh\eta',\ r' = \frac{r_2}{2}. \tag{5.28}$$

In terms of these new variables, the rates above can be rewritten,

$$\frac{dN_c}{d\tau} = 16\pi \frac{d^2N}{dA\,d\eta} \int d\eta' r' dr' d^3p_2 \frac{d^3N}{d^3p_2} \delta(\tau - \tau_c) \Theta\left(\frac{\sigma}{\pi} - b^2\right) \tag{5.29}$$

$$= 16\pi \frac{d^2N}{dA\,d\eta} \int d\eta' r' dr' d^3p_2 \frac{d^3N}{d^3p_2} \delta(r' - r_c) \frac{2\tau}{C_0 r' + C_1} \Theta\left(\frac{\sigma}{\pi} - b^2\right), \tag{5.30}$$

$$\frac{d\langle E_1 \rangle}{d\tau} = 16\pi \frac{d^2N}{dA\,d\eta} \int d\eta' r' dr' d^3p_2 \frac{d^3N}{d^3p_2} \delta(r' - r_c) \frac{2\tau}{C_0 r' + C_1} \Theta\left(\frac{\sigma}{\pi} - b^2\right) \delta E_1. \tag{5.31}$$

When solving for r_c, there are two solutions to Eq. (5.26). If solutions for both positive and negative r_c are used, the factor 16π should be reduced to 8π.

These results can be expressed as averages over p_1 and p_2

$$\frac{dN_c}{d\tau} = 32\pi\tau \frac{d^2N}{dA\,d\eta} \int d\eta' \left\langle \frac{r_c}{C_0 r_c + C_1} \right\rangle \Theta\left(\frac{\sigma}{\pi} - b^2\right), \tag{5.32}$$

$$\frac{d\langle E_1 \rangle}{d\tau} = 32\pi\tau \frac{d^2N}{dA\,d\eta} \int d\eta' \left\langle \frac{r_c}{C_0 r_c + C_1} \delta E_1 \right\rangle \Theta\left(\frac{\sigma}{\pi} - b^2\right). \tag{5.33}$$

If scattering angles are chosen with equal probability forwards and backwards, the average change in the two energies is

$$\delta E_1 = \frac{E_2 - E_1}{2}. \tag{5.34}$$

The nonlocal aspect of the collision kernel should contribute to heating the particles in their local frame. From physical arguments, the nonlocal contribution to heating is expected to scale with temperature, density, time and cross section in a simple manner.

$$\frac{dE_\perp}{d\tau} = \frac{3}{4\pi} \frac{d\langle E_1 \rangle}{d\tau} \beta \frac{d^2N}{dA d\eta} \frac{\sigma^2 T}{\tau^3}, \tag{5.35}$$

where E_t is the mean transverse energy per particle and β is a dimensionless constant.

The simple scaling derives from the hydrodynamically motivated Eqs. (5.11) and (5.12). The collision rate is expected to scale proportional to the density, which requires the factor $d^2N/(dAd\eta)$ and one inverse power of τ, and the cross-section. The squared-velocity gradient suggests an extra factor of τ^{-2}, and the range of the interaction requires

an extra factor of σ. The constant β is determined by the form of the differential cross section, e.g., *s*-wave scattering would result in a higher β than a highly forward-peaked form. Since one power of σ comes from the range of interaction, β should scale inversely with the sampling factor λ. Finally, the effective mass should be proportional to the temperature.

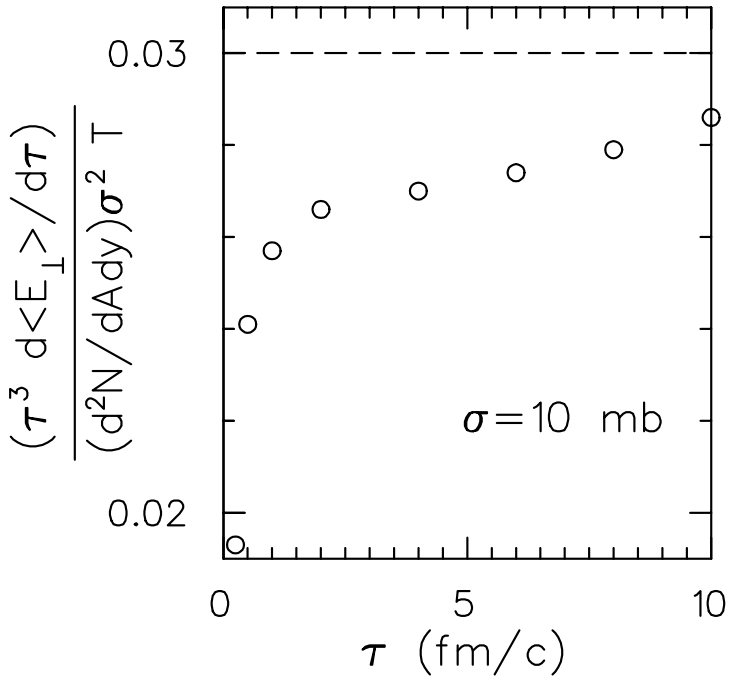

Figure 5.1: The heating due to nonlocal interactions as calculated numerically from the collision kernel (circles) is scaled in such a way that it would be constant if the simple hydrodynamic scaling arguments were valid. The dashed line represents the asymptotic value.

The heating rate due to nonlocal interactions is calculated from Eq. (5.33) by numerically analyzing the collision kernel and is displayed in Figure 5.1 after being scaled by the temperature, time and cross section. Had the simple scaling argument been correct the ratio would have been a constant β. However, due to higher order corrections in $1/\tau$, the ratio varies as a function of τ. The ratio approaches a constant for large τ, $\tau^2 >> \sigma$. The scaling fails when τ becomes less than the range of the interaction, which for this example is ~ 1.0 fm due to the cross section of 10 mb. The departure of the ratio from a straight line illustrates the limitation of simple hydrodynamic arguments to describe the viscous heating

from nonlocal interactions.

5.2.2 Comparison to Numerical Results

Finally, numerical results are presented from a model based on the Gromit framework. A boost-invariant and in the transverse directions closed system are simulated with cyclic boundary conditions in η and in the transverse coordinates, respectively. The viscous heating rate observed in the numerical calculation are compared with the viscous heating rate expected from the scaling arguments expressed in Eq. (5.35), where the coefficient β was determined from analyzing the collision kernel from the last section. The temperature was set to 400 MeV at a time $\tau = 0.1$ fm/c, and the cross section was chosen to be 10 mb. A simple *s*-wave form was used for the angular dependence of the cross section.

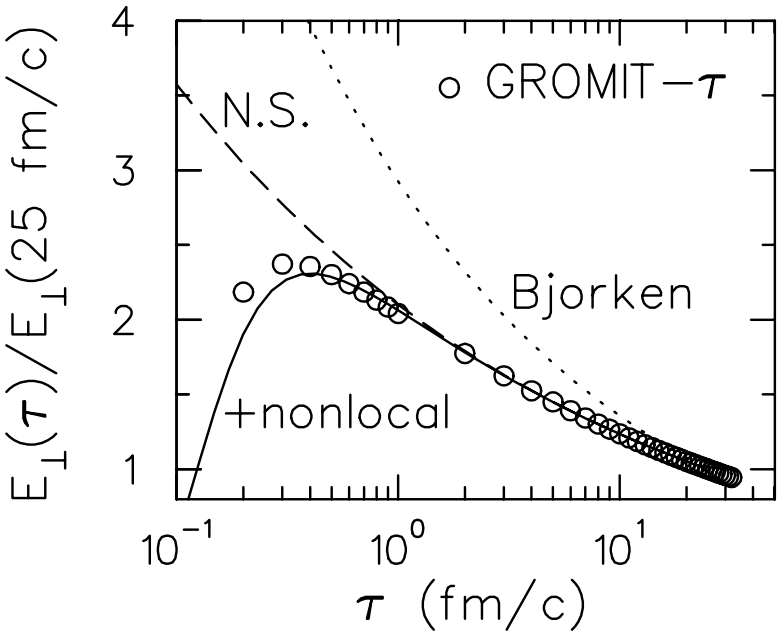

Figure 5.2: The mean transverse energy for particles participating in a boost-invariant Bjorken expansion is displayed as a function of the proper time (circles). Also displayed are the Bjorken hydrodynamic result (dotted line), the Navier-Stokes correction which accounts for viscous shear arising from a finite mean free path (dashed line) and the correction due to nonlocal interactions as expected from simple scaling arguments (solid line). Nonlocal interactions are important at small times when the velocity gradients and collision rates are high.

The resulting mean transverse energy is displayed in Figure 5.2 as a function of τ. The initial heating derives from the nonlocal nature of the interactions. Longitudinal cooling ultimately dominates the behavior as the nonlocal contribution to the heating falls roughly at τ^{-3}.

The dotted line in Figure 5.2 describes the evolution of the transverse energy in the limit of ideal (nonviscous) hydrodynamics. In that limit, the stress-energy tensor has a simple form,

$$T^{\alpha\beta} = \varepsilon u^{\alpha} u^{\beta} + P(u^{\alpha} u^{\beta} - g^{\alpha\beta}). \tag{5.36}$$

In the Bjorken limit, $\partial v/\partial z = 1/\tau$ and the evolution of the energy density becomes

$$\frac{\partial}{\partial t}\varepsilon = -\frac{P+\varepsilon}{\tau}. \tag{5.37}$$

For the massless case, $P = \varepsilon/3$, which gives the result,

$$\varepsilon(\tau) = \varepsilon(\tau_0)\left(\frac{\tau}{\tau_0}\right)^{-4/3} \tag{5.38}$$

The velocity gradient generates a shear which contributes an additional term to the stress-energy tensor.

$$T_{\eta}^{\alpha\beta} = \eta\left(-g^{\alpha\gamma} - u^{\alpha}u^{\gamma}\right)\left(\frac{\partial u_{\gamma}}{\partial x_{\beta}} + \frac{\partial u_{\beta}}{\partial x_{\gamma}} - \frac{2}{3} g_{\gamma}^{\beta}\partial\cdot u\right). \tag{5.39}$$

In a simulation, η_{NS} can be determined by evaluating the stress-energy tensor.

$$\frac{T^{xx} + T_{yy}}{2} - T^{zz} = 2\frac{\eta_{NS}}{\tau}. \tag{5.40}$$

The components of the stress-energy tensor are extracted by analyzing the momenta of particles as measured in the local rest frame.

$$T_{ij} = \frac{1}{V}\sum \frac{p_i p_j}{E_p}. \tag{5.41}$$

The Navier-Stokes evolution of the energy density is governed by the equation,

$$\frac{\partial}{\partial\tau}\varepsilon = -\frac{P+\varepsilon}{\tau} + \frac{4}{3}\frac{\eta_{NS}}{\tau^2}. \tag{5.42}$$

For massless particles interacting with a constant cross section, dimensional arguments force the viscosity to rise linearly with τ since the mean free path should grow with τ due to the density falling as $1/\tau$.

$$\eta_{NS} = C_{NS}\varepsilon\tau, \tag{5.43}$$

where C_{NS} is a constant, determined only by the form of the cross section. The energy density then follows the Navier Stokes form [85]. This form should be valid unless the viscous contribution to the stress energy tensor approaches the same order as the equilibrated pressure [52].

$$\varepsilon(\tau) = \varepsilon(\tau)\left(\frac{\tau}{\tau_0}\right)^{-(4/3)(1-C_{NS})}. \tag{5.44}$$

The Navier Stokes result is represented by a dashed line in Figure 5.2. The value of C_{NS} was determined by evaluating the asymmetry of the stress-energy tensor in the simulation at large times. Running simulations with a large sampling ratios generated results in excellent agreement with the Navier Stokes result.

The inclusion of nonlocal effects is responsible for the discrepancy between the simulation results in Figure 5.2 and the Navier-Stokes results. Eq. (5.12) suggests that the nonlocal correction to the viscosity should scale proportional to τ^{-2},

$$\eta_{nl} = C_{nl}\varepsilon/\tau, \tag{5.45}$$

where C_{nl} is independent of τ and scales with σ^2 as explained in the previous section. Now, the evolution of the energy density can be determined by solving the hydrodynamical equations of motion,

$$\frac{\partial}{\partial\tau}\varepsilon = -\frac{4}{3}(1-C_{NS})\frac{\varepsilon}{\tau} + \frac{4}{3}C_{nl}\frac{\varepsilon}{\tau^3} \tag{5.46}$$

This equation has a simple solution.

$$\varepsilon(\tau) = \varepsilon(\tau_0)\left(\frac{\tau}{\tau_0}\right)^{4/3(1-C_{NS})}\exp\left(\frac{2C_{nl}}{3}\left(\frac{1}{\tau_0^2}-\frac{1}{\tau^2}\right)\right). \tag{5.47}$$

This form is shown with the solid lines in Figure 5.2. The constant C_{nl} was determined by the asymptotic limit of Figure 5.1. The effect of nonlocal interactions is somewhat overestimated at small times by Eq. (5.47) as would be expected by considering Figure 5.1 which shows that that growth of the viscous heating at small τ is somewhat slower than the naive expectation that it scales as τ^{-3}.

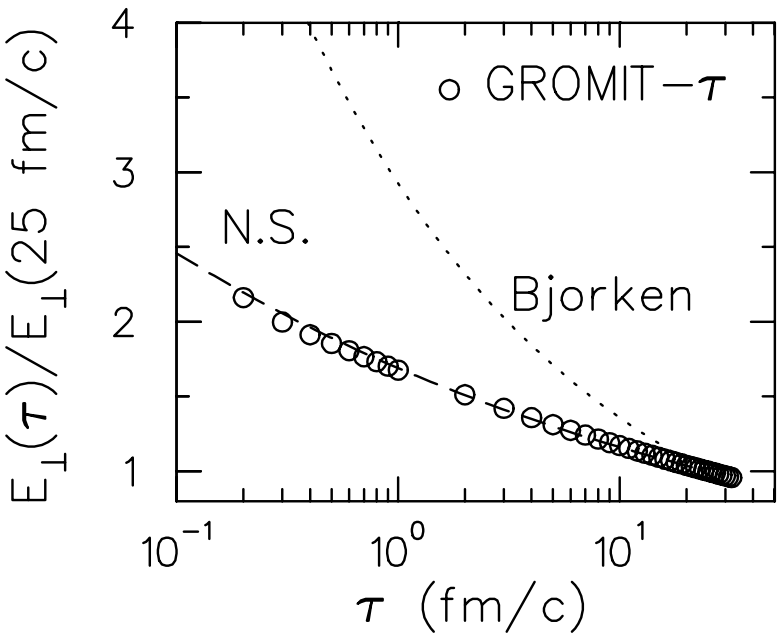

Figure 5.3: The mean transverse energy is plotted as a function of time for the case where a forward-peaked cross section as described in Eq. (3.35) is implemented. The results from Gromit-τ (circles) are well described by the Navier-Stokes (dashed line) correction to the Bjorken solution (dotted line). As compared to *s*-wave scattering, the Navier-Stokes viscosity is increased while the nonlocal contribution to the viscosity becomes negligible.

The effect of nonlocal interactions is lessened for scatterings that are more forward peaked. Figure 5.3 illustrates the behavior of E_t as a function of τ for a screened Rutherford scattering as given in Eq. (3.35). Here, the screening mass μ is chosen to provide a cross section of 10 mb. As compared to the *s*-wave scattering result in Figure 5.2, the effect of nonlocal interactions is diminished while the Navier-Stokes viscosity is increased. This is expected since the mean free path is effectively increased while the energy transfer inherent to collisions is decreased.

Finally, the effect of nonlocal interactions that might be expected in the earliest moments of the big bang should be mentioned. In that case cross sections should become perturbative and particles should be approximately massless. In this case cross sections should scale as α^2/T^2, where α is the unified coupling constant. Since T would scale as $1/\tau$, the Navier-Stokes viscosity and the nonlocal viscosity should both scale identically with τ. Since the nonlocal terms scale as σ^2 while the Navier-Stokes terms scale as σ^{-1}, the terms would differ in importance by a constant proportional to α^6. Thus, if the system becomes perturbative, the nonlocal terms are expected to be negligible compared to the Navier-Stokes terms. However, the physics of high-energy hadronic collisions is far from perturbative, and the large coupling constants magnify the importance of the nonlocal terms relative to Navier-Stokes terms.

Chapter 6

Correlation Function for Particles from Resonance Decays

The Hanbury Brown–Twiss (HBT) effect was first proposed in 1954 as a means to measure the angular size of distant stars by exploiting the quantum correlations of photons [88]. The same authors then demonstrated their technique in 1956 by determining the angular size of the star Sirius [89]. Independently in the early 1960's, the HBT effect was discovered in proton–anti-proton collisions, by Goldhaber *et al*. [79].

Since then, analyses of two-boson correlations have provided tangible information regarding the spacetime development of hadronic reactions [91, 155]. Pions, kaons, and photons have all been exploited for their bosonic nature which results in a positive correlation at small relative momentum. Numerous other correlations, involving nucleons [90, 21, 70, 75] or light nuclei [25, 26] that are correlated due to the strong or Coulomb interaction as well as identical-particle statistics, have also been analyzed and have given further information regarding collision dynamics. Source sizes and time scales have been extracted from collisions covering a wide assortment of reactions, from heavy-ion collisions at a few MeV per nucleon, where time scales of thousands of fm/c have been determined, to e^+e^- annihilations, where lifetimes of a fraction of 1 fm/c have been observed [78, 19, 47, 3].

The comparison of theoretically predicted correlation functions with experimental re-

sults provides an important test of the dynamical properties of reaction models. Most models provide semi-classical information about the source function $S(\mathbf{p},x)$, the probability of emitting a particle of momentum $\mathbf{p}$ from the spacetime point x. By convoluting the source functions for particles of momenta $\mathbf{p}_1$ and $\mathbf{p}_2$ with the squared relative wave function $|\phi_{\mathbf{q}}(x_1 - x_2)|^2$, one is able to predict the correlation function $C(\mathbf{p}_1,\mathbf{p}_2)$. Source functions are usually obtained from semi-classical simulations, where the source points are associated with the last point of interaction [126]. Particles from resonances are usually assumed to be emitted according to an exponential decay law, with the characteristic time usually chosen to be independent of the energy of the resonance. Quantum considerations have been explored by Lednicky and Progulova [106] and by Bertsch, Danielewicz and Herrmann [30].

In this chapter, two goals are pursued. First, the importance of quantum treatments is quantified by comparing to semi-classical forms for a simple thermal model. Although the presented formalism is not much different from that discussed previously in the literature [106, 30], the differences with semi-classical treatments have not previously been studied quantitatively. Quantum corrections are found to become important when kinematics constrain the resonances to be off mass shell. Second, an alteration is proposed to the methods for extracting correlations from classical simulations to better account for quantum effects. This modification is shown to be able to account for the quantum corrections by incorporating information regarding the off-shell energy of the decaying resonance. In this study, any interaction between the particles aside from the constraints imposed by symmetrization is neglected.

6.1 Derivation of Corrections to the Correlation Function

6.1.1 Correlations from Direct Sources

The two-particle correlation function for particles with momenta $\mathbf{p}_1$ and $\mathbf{p}_2$ is usually [91, 155] defined as

$$C(\mathbf{p}_1,\mathbf{p}_2) \equiv \frac{dN^{(2)}/(d^3p_1 d^3p_2)}{(dN^{(1)}/d^3p_1)\,(dN^{(1)}/d^3p_2)}. \tag{6.1}$$

The one-particle probabilities in the denominator can be determined by matrix elements $T_f(x)$ where f describes the remainder of the system, and x is the point at which the particles had the final interaction with the system. Without loss of generality

$$2E_p\frac{dN^{(1)}}{d^3p} = \sum_f \left| \int d^4x\, T_f(x) e^{ip\cdot x} \right|^2. \tag{6.2}$$

The definition of the source function is

$$S(p,x) \equiv \sum_f \int d^4\delta x\, T_f^*(x+\delta x/2) T_f(x-\delta x/2) e^{-ip\cdot\delta x}, \tag{6.3}$$

which leads to the simple relation

$$2E_p\frac{dN^{(1)}}{d^3p} = \int d^4x\, S(p,x)\Big|_{p_0=E_p}. \tag{6.4}$$

The source function can be interpreted as the probability per unit spacetime for creating a particle of momentum $\mathbf{p}$.

Since source functions can be extracted from semi-classical simulations or thermal models, it has proven useful to also express two-particle probabilities from Eq. (6.1) in terms of source functions. The two-particle probability requires a two-particle matrix element $T_f^{(2)}(x_a,x_b)$. With the assumption of independent (or uncorrelated) emission, the two-particle matrix element factorizes [30].

$$T_f^{(2)}(x_a,x_b) \longrightarrow T_{f_a}(x_a) T_{f_b}(x_b), \tag{6.5}$$

where, a and b label independent sources. The two-particle probability then becomes

$$(2E_1)(2E_2)\frac{dN^{(2)}}{d^3p_1 d^3p_2}$$

$$= \sum_{a,b,f_a,f_b} \left| \int d^4x_a d^4x_b \; T_{f_a}(x_a) T_{f_b}(x_b) \frac{1}{\sqrt{2}} \left\{ e^{ip_1\cdot x_a + ip_2\cdot x_b} + e^{ip_2\cdot x_a + ip_1\cdot x_b} \right\} \right|^2$$

$$= \sum_{a,b} \left\{ \int d^4x_a d^4x_b \; S_a(p_1,x_a) S_b(p_2,x_b) + \int d^4x_a d^4x_b \; S_a(\bar{p},x_a) S_b(\bar{p},x_b) e^{i(p_2-p_1)\cdot(x_a-x_b)} \right\},$$

where $\bar{p} = (p_1+p_2)/2$. The expression above can be rewritten conveniently in terms of the Fourier transform of the source function

$$I_{a,b}(p_1,p_2) = \int d^4x \; S_{a,b}\left(\frac{p_1+p_2}{2},x\right) e^{i(p_2-p_1)\cdot x}, \tag{6.6}$$

which leads to

$$(2E_1)(2E_2)\frac{dN^{(2)}}{d^3p_1 d^3p_2} = \sum_{a,b} \left\{ I_a(p_1,p_1) I_b(p_2,p_2) + I_a(p_1,p_2) I_b(p_2,p_1) \right\}. \tag{6.7}$$

The correlation function then takes on a simple form

$$C(\mathbf{p}_1,\mathbf{p}_2) = 1 + \frac{\sum\limits_{a,b} I_a(p_1,p_2) I_b(p_2,p_1)}{\sum\limits_{a,b} I_a(p_1,p_1) I_b(p_2,p_2)}, \tag{6.8}$$

which is similar to that originally mentioned by Shuryak [139].

Simulations typically provide a sampling of the on-shell source function. The application of Eq. (6.6) in simulations is made difficult because the source functions are evaluated at $\bar{p}_0 \neq E_{(p_1+p_2)}/2$ meaning that they require off-shell information. The above formalism can be related to simulations through the smoothness approximation [125, 7],

$$S_a\left(\frac{p_1+p_2}{2},x_a\right) S_b\left(\frac{p_1+p_2}{2},x_b\right) \longrightarrow S_a(p_1,x_a)\, S_b(p_2,x_b). \tag{6.9}$$

For thermal sources, a form for the off-shell behavior of the source function can be justified and the smoothness approximation can be averted. A quantum theory would provide the

T matrices that would also allow off-shell evaluation of the source function. In fact, some formalisms have been developed where classical simulations are augmented by converting the point particles into wave packets [119, 164]. This also allows to forego the smoothness approximation, but at the price of inserting an ansatz for the quantum behavior that has some peculiarities. The issue of the smoothness approximation will be side-stepped in this study, so as to focus on quantum aspects associated with the propagation of off-shell particles.

When calculating correlation functions from simulations, particles from resonances are usually included in the source function by using the spacetime points from which the resonances decay. The lifetime of the resonance affects the correlation function through the exponential decay that is simulated in the transport model. As will be demonstrated below, the exponential decay law is modified if the dynamics emit resonances with a particular mass or range of masses. In this case, the form of the source function becomes nonexponential as will be explained in the following.

6.1.2 Correlations from Resonant Sources

A formalism is presented for calculating two-particle correlation functions from resonance decays given that one or both of the pions might originate from a resonance. The result will depend on the source function that represents the creation of the resonance rather than the source function that represents the points at which the final-state pions are created. The evolution and decay of the resonance will be accounted for through the quantum propagator of the resonance. The spacetime point at which the resonance decayed to produce the final-state pions will be treated as an intermediate quantum step in the evolutionary path between the initial creation of the resonance and the asymptotic momentum states of the decay products. The expressions derived here thus incorporate an integration over all points at which the resonance might have decayed relative to the points at which the resonance is

created.

Three examples will be considered, a hypothetical scalar particle A that decays into two pions, the vector meson ρ, which also decays into two pions, and the vector meson ω, which decays into three pions. The matrix element for creating the pion and a second particle with momentum $\mathbf{k}$ through a scalar resonance A is

$$T_{\pi,f_A,k}(x) = g\int d^4x_A\ \tilde{G}_A(x-x_A)T_{A,f_A}(x_A)e^{ik\cdot x}, \tag{6.10}$$

where $\tilde{G}_A$ is the Fourier transform of the propagator for the resonance and f_A refers to the state of the remainder of the source. Here T_π is effectively the T-matrix element for emission of the pion, while T_A is the T-matrix element that would describe emission of the resonance if the resonance were stable.

Following the same method as in the previous subsection, T_π can be used to create the pion source function using Eq. (6.3) to express $T_A^*(x)T_A(x')$ in terms of the source function of the resonance. The resulting expression for the pion source function can be used to generate I_A, as defined in Eq. (6.6), which is sufficient to calculate correlation functions,

$$I_A(p_1,p_2) = g^2\int\frac{d^3k}{2E_k}\int d^4x_A\ \exp[i(p_2-p_1)\cdot x_A]S_A\left(\frac{p_1+p_2}{2}+k,x_A\right) \times G_A(p_1+k)G_A^*(p_2+k), \tag{6.11}$$

$$G_A(p) = \frac{i}{p^2-M_A^2+i\Pi_A(p^2)}, \tag{6.12}$$

$$\Pi_A(m^2) = M_A\Gamma_A\frac{q}{q_R}\frac{M_A}{m}. \tag{6.13}$$

Here, $m^2 = p_A^2$, M_A and Γ_A are, respectively, the pole mass and width of the resonance. The relative momentum of the outgoing pions in the frame of the resonance is $q^2 = m^2/4 - m_\pi^2$ and q_R^2 is the same quantity for an on-shell resonance. It should be emphasized that the interference term in Eq. (6.11) can be calculated without reference to the direct source of the pions, as the source function of the resonance becomes the required input.

In order to understand the role of the propagators, the emission of a pion pair with momenta p and k through a single, scalar resonance with momentum $p_A = p+k$ is considered

$$2E_p\frac{dN}{d^3p} = I_A(p,p), \tag{6.14}$$

$$dN = \frac{d^3p}{2E_p}\frac{d^3k}{2E_k}d^4x\; S_A(p+k,x)\frac{g^2}{\left|(p+k)^2 - M_A^2 + i\Pi_A\left((p+k)^2\right)\right|^2} \tag{6.15}$$

$$= \frac{d^3p_A}{2E_A}d^4x\; S_A(p_A,x)\; dm^2\frac{1}{\pi}\mathrm{Im}\frac{1}{m^2 - M_A^2 - i\Pi_A(p_A^2)}. \tag{6.16}$$

The spectral function that describes the density of states of resonances of invariant masses m,

$$\frac{1}{2\pi}\mathrm{Im}\frac{1}{m^2 - M_A^2 - i\Pi_A(p_A^2)} = \frac{dn}{dm^2}. \tag{6.17}$$

Thus, it is evident that the source function does not provide any information regarding the mass or width of the resonance. However, combined with the spectral function, which derives from the product of propagators, it provides the probability of creating the resonance at space time point x with momentum p and with invariant mass m. For the direct case considered in the last subsection, the source function was always evaluated on shell, i.e., the spectral function was effectively a delta function.

The same calculation can be performed for vector resonances such as the ρ meson. In that case, the coupling of the pions to the vector meson is

$$\mathcal{L}_{\mathrm{int}} = i\lambda\left(\pi\partial_\mu\pi\right)\rho^\mu. \tag{6.18}$$

The expression for I_ρ is similar to 6.11 with the source function and propagator accounting for the vector nature of the ρ,

$$I_\rho(p_1,p_2) = \lambda^2\int\frac{d^3k}{2E_k}\int d^4x_\rho\; \exp[i(p_2-p_1)\cdot x_\rho](p_1-k)_\alpha G_\rho^{\alpha\beta}(p_1+k)$$

$$\times S^\rho_{\beta\gamma}\left(\frac{p_1+p_2}{2}+k, x_\rho\right) G_\rho^{*\gamma\delta}(p_2+k)(p_2-k)_\delta. \tag{6.19}$$

The propagator for the vector resonance is

$$G_\rho^{\alpha\beta}(p) = i\frac{-g^{\alpha\beta} + p^\alpha p^\beta/p^2}{p^2 - M_A^2 + i\Pi_\rho(p^2)}. \tag{6.20}$$

For the vector case the self-energy scales differently as a function of the resonance mass than in the scalar case,

$$\Pi_\rho(m^2) = M_\rho\Gamma_\rho\frac{q^3}{q_R^3}\frac{M_\rho}{m}, \tag{6.21}$$

where the same notation as in Eq. (6.13) was used.

As a third example, the propagation is considered of an ω meson, which is also a vector resonance, but decays into three pions through

$$\mathcal{L}_{\rm int} = i\kappa\varepsilon_{\mu\nu\xi\psi}\omega^\mu\partial^\nu\pi^+\partial^\xi\pi^0\partial^\psi\pi^-. \tag{6.22}$$

In this case the expression for I_ω becomes even more complicated than the ρ example.

$$\begin{aligned} I_\omega(p_1,p_2) = \kappa^2\int\frac{d^3k}{2E_k}\frac{d^3l}{2E_l}\int d^4x_\omega\ \exp[i(p_2-p_1)\cdot x_\omega] \\ \times\varepsilon_{\alpha\mu\nu\xi}\ p_1^\mu k^\nu l^\xi G_\omega^{\alpha\beta}(p_1+k+l)S_{\beta\gamma}^\omega\left(\frac{p_1+p_2}{2}+k+l, x_\omega\right) \\ \times G_\omega^{*\gamma\delta}(p_2+k+l)\varepsilon_{\delta\mu'\nu'\xi'}\ p_2^{\mu'}k^{\nu'}l^{\xi'}. \end{aligned} \tag{6.23}$$

The expression for the self-energy is also somewhat more complicated.

$$\Pi_\omega(m^2) = B\int\frac{d^3k}{2E_k}\frac{d^3l}{2E_l}\ \delta\left((m-E_k-E_l)^2 - E_{\mathbf{k}+\mathbf{l}}^2 - 2kl\cos\theta\right)m^2|\mathbf{k}\times\mathbf{l}|^2. \tag{6.24}$$

where θ is the angle between **k** and **l** and B is an uninteresting constant fixed by the condition that $\Pi_\omega(M_\omega^2) = M_\omega\Gamma_\omega$, with M_ω and Γ_ω being the mass and the width of ω, respectively. After applying the delta function, there remains a fairly complicated expression, which was evaluated numerically in the subsequent considerations of the ω case.

6.1.3 Correlation Functions from Monte Carlo Simulations

Simulations of heavy-ion collisions usually provide the creation points of pions along with their outgoing momenta. Neglecting other interactions besides symmetrization, correlation

weights for pions of momenta p_1 and p_2 originating from spacetime points x_a and x_b are usually determined by calculating the average symmetrization weight of all pairs satisfying the imposed binning or acceptance [126].

$$C(p_1,p_2) = 1 + \frac{\sum_{a,b} \int d^4x_a d^4x_b \; S_a(p_1,x_a) S_b(p_2,x_b) w_a(p_1,p_2) w_b(p_2,p_1)}{\sum_{a,b} \int d^4x_a d^4x_b \; S_a(p_1,x_a) S_b(p_2,x_b)} \tag{6.25}$$

$$\equiv 1 + \langle w_a(p_1,p_2) w_b(p_2,p_1) \rangle. \tag{6.26}$$

Inspection of Eqs. (6.6), (6.8), and (6.9) reveals the weight for direct sources,

$$w_{\mathrm{d}}(p_1,p_2) = \exp[i(p_1-p_2)\cdot x_d] \frac{S(\frac{p_1+p_2}{2},x_d)}{S(p_1,x_d)}, \tag{6.27}$$

$$w_{\mathrm{d}}^{(\mathrm{sc})}(p_1,p_2) = \exp[i(p_1-p_2)\cdot x_d], \tag{6.28}$$

where the difference between the two forms is the assumption of the smoothness approximation [125, 7] in the Eq. (6.28).

If the particle originates from the decay of a scalar resonance A, the weight takes on a different form as can be seen from inspecting 6.11,

$$w_A(p_1,p_2) = \frac{S_A(\frac{p_1+p_2}{2}+k,x_A)}{S_A(p_1+k,x_A)} \frac{(p_1+k)^2 - M_A^2 - i\Pi_A[(p_1+k)^2]}{(p_2+k)^2 - M_A^2 - i\Pi_A[(p_2+k)^2]} e^{i(p_1-p_2)\cdot x_A}. \tag{6.29}$$

Here the resonance was created at x_A and decayed into pions of momenta p_1 and k. The spacetime coordinate of the decay does not enter the weight as all decay points have been considered. If the decay is of a vector resonance such as a ρ meson, the weights are slightly different,

$$w_\rho(p_1,p_2) = \frac{S_\rho(p_1,p_2,k)}{S_\rho(p_1,p_1,k)} \frac{(p_1+k)^2 - M_\rho^2 - i\Pi_\rho[(p_1+k)^2]}{(p_2+k)^2 - M_\rho^2 - i\Pi_\rho[(p_2+k)^2]} e^{i(p_1-p_2)\cdot x_\rho} \tag{6.30}$$

$$S_\rho\left(p_1,p_2,k,x_\rho\right) = (p_1-k)^\alpha \, S_{\alpha\beta}^\rho \left(\frac{p_1+p_2}{2}+k,x_\rho\right) (p_2-k)^\beta. \tag{6.31}$$

In the derivation of S_ρ the two pions involved in the resonance decay are assumed to have equal mass.

Any sort of resonance can be included in this manner, including resonances that decay into three or more bodies. One such example is ω, which decays into three pions, one of each species. Labeling the momenta of the two pions, whose symmetrization is ignored, as k and l, the weights turn out to be

$$w_\omega(p_1,p_2) = \exp[i(p_1-p_2)\cdot x_\omega] \times \frac{S_\omega(p_1,p_2,k,l)}{S_\omega(p_1,p_1,k,l)} \frac{(p_1+k+l)^2 - M_\omega^2 - i\Pi_\omega[(p_1+k+l)^2]}{(p_2+k+l)^2 - M_\omega^2 - i\Pi_\omega[(p_2+k+l)^2]}, \tag{6.32}$$

$$S_\omega(p_1,p_2,k,l,x_\omega) = \varepsilon^\alpha{}_{\mu\nu\xi}\, p_1^\mu k^\nu l^\xi S^\omega_{\alpha\beta}\left(\frac{p_1+p_2}{2}+k+l, x_\omega\right) \varepsilon^\beta{}_{\mu'\nu'\xi'}\, p_2^{\mu'} k^{\nu'} l^{\xi'}. \tag{6.33}$$

Thus, weights can be used to calculate correlation functions for the decay of any resonance in a rather straightforward manner. The formalism coherently accounts for all points at which the resonance may have decayed, but requires information regarding the points at which the resonances were created as well as information about the accompanying particles in the decay. The only difficulty comes in assigning the ratios of the source functions, i.e., the smoothness problem. For a thermal source, the source functions assume a simple form, in the scalar case

$$S_A(p,x) \sim p_0 e^{-p_0/T} \tag{6.34}$$

and in the vector case

$$S^\rho_{\alpha\beta}(p,x) \sim p_0 e^{-p_0/T}(-g_{\alpha\beta} + p_\alpha p_\beta/p^2). \tag{6.35}$$

The Boltzmann factor cancels out of the ratios. Thus, for the thermal example, the weights become a product of four factors, a phase arising from the points at which the resonance R $(= A, \rho, \omega)$ is created, a ratio of energies, a spin factor, and a ratio of propagator denominators.

$$w_R^{(th)}(p_1,p_2) = \frac{(\frac{p_1+p_2}{2}+k')\cdot n}{(p_1+k')\cdot n} \frac{\chi_R(p_1,p_2)}{\chi_R(p_1,p_1)} \frac{(p_1+k')^2 - M_R^2 - i\Pi_R[(p_1+k')^2]}{(p_2+k')^2 - M_R^2 - i\Pi_R[(p_2+k')^2]} \times e^{i(p_1-p_2)\cdot x_R}, \tag{6.36}$$

where n refers to the frame of the thermal source and k' is equal to either k for a two-body decay, or to $k+l$ for a three-body decay.

The spin factors χ_R depend on the sort of resonance being considered.

$$\chi_A(p_1,p_2) = 1 \tag{6.37}$$

$$\chi_\rho(p_1,p_2) = (p_1-k)^\alpha \left(-g_{\alpha\beta} + \bar{p}_\alpha \bar{p}_\beta/\bar{p}^2\right)(p_2-k)^\beta, \tag{6.38}$$

$$\chi_\omega(p_1,p_2) = \varepsilon^\alpha{}_{\mu\nu\xi}\, p_1^\mu k^\nu l^\xi \left(-g_{\alpha\beta} + \bar{p}_\alpha \bar{p}_\beta/\bar{p}^2\right) \varepsilon^\beta{}_{\mu'\nu'\xi'}\, p_2^{\mu'} k^{\nu'} l^{\xi'}, \tag{6.39}$$

where $\bar{p} = (p_1+p_2)/2 + k'$.

However, this technique cannot be easily applied to nonthermal sources because the off-shell behavior of the source function is not always known. This problem also confronts calculations with direct sources, and forces either the invocation of the smoothness approximation, or the assumption of some form for the off-shell behavior of the source function.

In analogy to the smoothness approximation, the thermal weight $w_R^{(th)}$ might be used assuming a reference frame n^μ or simply neglect the ratio of energies in 6.36. In fact, the ratio $\chi_R(p_1,p_2)/\chi_R(p_1,p_1)$ can also be neglected to a reasonable approximation as the structure of the correlation function derives largely from the last factor in Eq. (6.36), the ratio of propagator denominators.

6.2 The Importance of Proposed Modification

Calculations of the quantum type described in Subsection 6.1.2 should be compared with semi-classical calculations where the resonance is assumed to propagate classically and decay according to an exponential form $\exp(-t/\tau)$. For the purposes of this comparison, two simplified systems are modeled, one of decaying ρ resonances and a second of decaying ω's. For each case resonances are produced and decayed with a Monte Carlo procedure according to a thermal distribution characterized by a temperature of 150 MeV. The mass

of ρ is 770 MeV and the width is chosen to be 150 MeV, while the mass of ω is 783 MeV and the width is 8.4 MeV.

6.2.1 Formalism for Semi-Classical Models

In the semi-classical descriptions, the correlation weights are determined by calculating the expectation value

$$w_R^{(\mathrm{sc})}(p_1,p_2,x_R) = \langle e^{i(p_1-p_2)\cdot x}\rangle \tag{6.40}$$

$$= \exp[i(p_1-p_2)\cdot x_R]\int d^4(x-x_R)\ \delta^3[\mathbf{x}-\mathbf{x}_R-\mathbf{v}_R(t-t_R)]$$

$$\times \exp[i(p_1-p_2)\cdot(x-x_R)]\frac{1}{\gamma_R\tau}\exp[-(t-t_R)/(\gamma_R\tau)]\Theta(t-t_R)$$

$$= \exp[i(p_1-p_2)\cdot x_R]\frac{m_R/\tau_R}{m_R/\tau_R+ip_R\cdot(p_1-p_2)}, \tag{6.41}$$

where γ_R is the Lorentz factor due to the motion of the resonance. Here, $w^{(\mathrm{sc})}$ assumes an exponential form for the pion emission, which is characterized by a lifetime τ. The same form for exponential decays was developed by Padula and Gyulassy [118].

Prescriptions for the energy dependence of the lifetime $\tau(m)$ are arbitrary and can be chosen freely. Three possibilities are investigated: (1) The lifetime is chosen such that $m/\tau = \Pi(m^2)$. This choice would be motivated by the form of the propagator. (2) The lifetime is chosen to correspond to the average emission time as described in Subsection 6.2.3, except that the relativistic generalization of Eq. (6.54) is used $\tau = 2m\ \Im(m^2-M_R^2-i\Pi)^{-1}$. (3) A fixed lifetime $1/\Gamma$ is used.

If the resonance distribution function in coordinate space is independent from that in momentum space, the interference term in the correlation function factorizes into a term stemming from the spacetime extent of the resonance source itself and one that arises from

the decay process.

$$C(p_1,p_2)-1=\Re\left\{\langle\exp[i(p_1-p_2)\cdot(x_A-x_B)]\rangle\left(C'(p_1,p_2)-1\right)\right\} \tag{6.42}$$

Here, x_A and x_B refer to points at which the resonances are created, and $\langle\exp[i(p_1-p_2)\cdot(x_A-x_B)]\rangle$ represents the weighted average using the product of the source functions as the weight:

$$\langle\exp[i(p_1-p_2)\cdot(x_A-x_B)]\rangle=|J_R(p_1-p_2)|^2, \tag{6.43}$$

where

$$J_R(p_1-p_2)=\frac{\sum_A\int d^4x_A S_A[(p_1+p_2)/2+k_A,x_A]\exp[i(p_1-p_2)\cdot x_A]}{\sum_A\int d^4x_A S_A[(p_1+p_2)/2+k_A,x_A]} \tag{6.44}$$

The reduced correlation function, $C'(p_1,p_2)-1$, is similar to the average of the weights $\langle w_a w_b\rangle$ from Subsection 6.1.3, only with the factors of $\exp[i(p_1-p_2)\cdot x_R]$ removed from the weights in Eq. (6.36). Since C' contains all the relevant information about the decay, we will focus on the reduced correlation function for our comparisons.

6.2.2 Numerical Results

To model the uncorrelated emission of pion pairs, thermal particles of momentum k (and l for the ω) are created by Monte Carlo, then a weight is added to the particles

$$z_i=\frac{E_k\{+E_l\}+E_i}{E_k\{E_l\}E_i}\frac{\chi_R(p_i,p_i)}{\left|(p_i+k')^2-M_R^2+i\Pi[(p_i+k')^2]\right|^2}, \tag{6.45}$$

where $i=1,2$ and the braces indicate terms that appear for ω only. This weight accounts for the spectral function of the resonances as described in Eq. (6.17) and for the spin factors χ_R as in Eqs. (6.37)-(6.39). Note that the weights $z_{1,2}$ are merely used to generate resonances and their products, and are not related to the correlation weights. If these weights were included through a keep/reject prescription, they would not need to appear in any of the following expressions.

Once the pions are statistically generated, the average weights described previously are calculated to generate the correlation functions,

$$C(p_1,p_2) = 1 + \Re\left(\frac{\sum_a z_1^a w_R^{(th),a}(p_1,p_2)}{\sum_a z_1^a} \frac{\sum_b z_2^b w_R^{(th),b}(p_2,p_1)}{\sum_b z_2^b} \right). \tag{6.46}$$

For this comparison w_R is either the weight for ρ, w_ρ, or the one for ω, w_ω. Note that a and b label individual resonances.

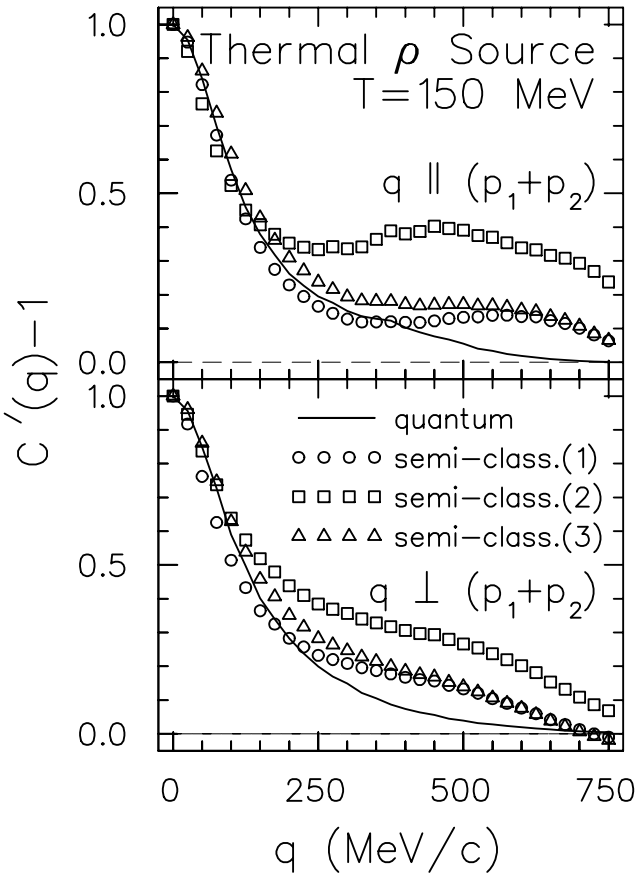

Figure 6.1: Reduced correlation function for a source of ρ mesons at a temperature of 150 MeV. The average momenta of the two pions is fixed at 200 MeV/c. By factoring out the spacetime dependence of the ρ, the manifestation of the ρ lifetime is singled out. The exact quantum treatment is shown to differ from the three semi-classical treatments that are described in the text. The failure of the semi-classical descriptions arises from the fact that the ρ width is sufficiently large for the thermal source to effectively emphasize a specific region of off-shellness.

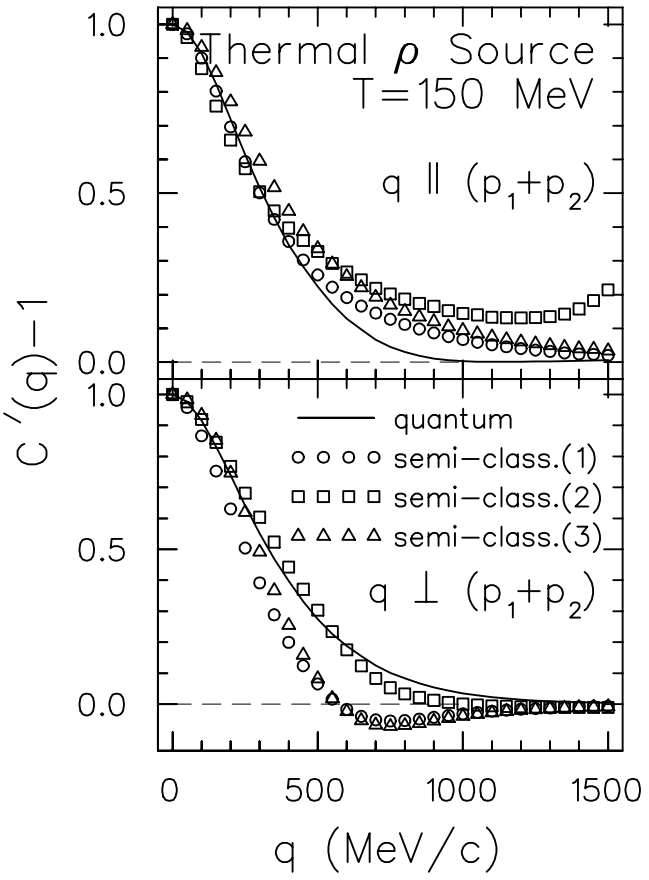

Figure 6.2: Same as Figure 6.1, except that ρ's have average momentum $P = 800$ MeV/c.

Figures 6.1 and 6.2 display the reduced correlation function for the cases where $(p_1 + p_2)/2 = 200$ MeV/c and 800 MeV/c, respectively. The upper panel of each figure displays results for the case where $\mathbf{p}_1$ is parallel to $\mathbf{p}_2$ while the lower panel displays the results for the case where the two momenta are perpendicular. All three semi-classical results exhibit significant deviations from the quantum calculations.

Figures 6.3 and 6.4 display the same information but for a thermal source of ω mesons. In this case, the semi-classical treatments are significantly more accurate. This could be explained by the width of the ω being much smaller than the temperature, which allows the spectral function of the ω to be sampled evenly. This notion will be explored further in Subsection 6.2.3.

The overall width of the correlation functions in the upper panels of Figs. 6.3 and 6.4

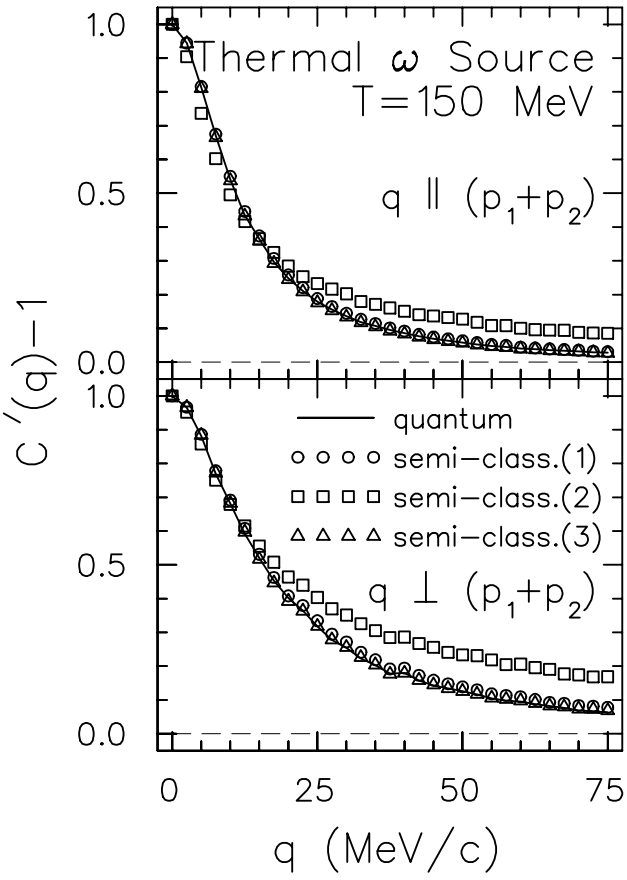

Figure 6.3: Same as Figure 6.1, but using a thermal source of ω's at a temperature of 150 MeV. In this case, since the width of the ω is much less than the temperature, semi-classical treatments work remarkably well.

can be understood by noting that the correlation's width should be determined by the condition $\Delta E\tau = 1$, where $\Delta E \approx v_R q$. The width of the correlation function for the lower panels, where $\mathbf{p}_1 \perp \mathbf{p}_2$, is more complicated since it is more sensitive to the spatial movement of the resonance while it decays. The correlation functions for the ρ in Figs. 6.1 and 6.2 are even more complicated since they extend to large relative momenta where ΔE approaches q. Given the complicated kinematics involved, it is not surprising that the result is sensitive to the exact form for the semi-classical treatment.

In the case of the ρ, none of the three semi-classical prescriptions for $\tau(m)$ provides a consistently good approximation to the quantum result for all scenarios shown in Figs. 6.1 and 6.2. They all exhibit significant deviations from the quantum result for high relative

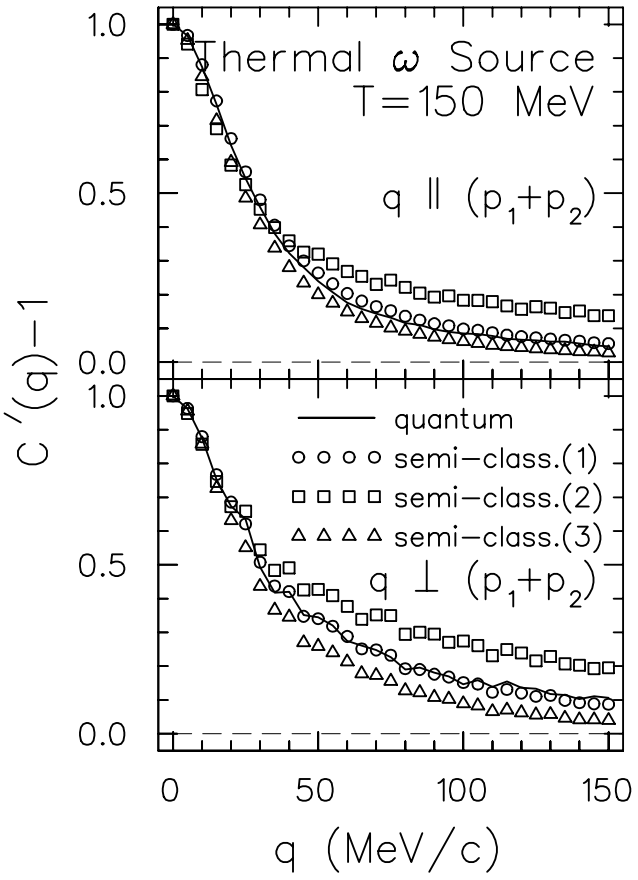

Figure 6.4: Same as Figure 6.3, except that ω's have average momentum $P = 800$ MeV/c.

momentum of the pion pair, above 200 MeV/c. In the case of the ω, where only small relative momenta, $q < 200$ MeV/c, are relevant, prescription (1) seems to best reproduce the quantum result, as can be seen in Figs. 6.3 and 6.4.

It should be emphasized that the correlation from the nonzero extent of the resonance source function has been factored out in this calculation. The deviations of the semi-classical results occur for relative momenta of a hundred MeV/c or more. In a heavy-ion collision the factor $\langle \exp[i(p_1 - p_2)\cdot(x_A - x_B)]\rangle$ in Eq. (6.43) would tend to zero for relative momenta much greater than 50 MeV/c due to the large spatial sizes of the emitting regions. Thus, the form of C' becomes irrelevant for higher relative momenta unless the source sizes are small, e.g., pp collisions.

These findings imply that the semi-classical treatments work quite well for the larger

sources considered with heavy-ion collisions. However, for smaller sources, especially when the resonance widths are comparable to the temperature and resonances are produced far off-shell, the semi-classical treatments significantly deviate from the quantum result. This can be linked to the failure of the usual exponential decay law when off-shell resonances are involved which will be investigated further in the following.

6.2.3 Limit of a Narrow Resonance

In this discussion, the source function is considered for a narrow Breit-Wigner resonance A. Then, according to Eqs. (6.2) and (6.10), the probability of emitting a pion pair with momenta k and p is

$$(2E_k)(2E_p)\frac{dN}{d^3p\,d^3k} = \sum_f \left| g\int d^4x d^4x_A\ \tilde{G}_A(x-x_A)T_{A,f,k}(x_A)e^{i(p+k)\cdot x}\right|^2 \tag{6.47}$$

$$= g^2\int d^4x_A d^4x\ S_A(p+k,x_A)K(p+k,x-x_A). \tag{6.48}$$

Here, K represents the probability of a resonance carrying momentum $p+k$ propagating from x_A to x. It may be expressed in terms of the Wigner transform of the propagators,

$$K(p,x) = \int \frac{d^4\delta q}{(2\pi)^4}\, e^{i\delta q\cdot x}G_A^*(p+\delta q/2)G_A(p-\delta q/2), \tag{6.49}$$

which is in general a complicated function. In the limit of a narrow resonance, the propagators can be expressed in a simplified form,

$$G_A(p) = \frac{1}{2M_A}\frac{i}{p_0-E_p+i\Gamma/2}. \tag{6.50}$$

The narrow resonance limit is adopted here to illustrate the quantum nature of the propagator. In addition, particles are assumed to be emitted with equal and opposite momenta. Integrating Eq. (6.49) over spatial coordinates gives the probability of the resonance propagating for a time t

$$\mathcal{R}(\Delta E,t) \equiv \frac{2\Gamma M_A^2}{\pi}\int d^3x\, K(p,x) = \frac{\Gamma}{\pi}\Theta(t)e^{-\Gamma t}\frac{\sin(2\Delta E t)}{\Delta E}, \tag{6.51}$$

where $\Delta E = E_k + E_p - M_A$ is the off-shellness. When Eq. (6.51) is integrated over the off-shellness, the expected exponential behavior is obtained.

$$\int d(\Delta E)\ \mathcal{R}(\Delta E, t) = \Gamma e^{-\Gamma t}, \tag{6.52}$$

whereas integrating over t describes the preference for emitting the particle with energy close to on-shell.

$$\int dt\ \mathcal{R}(\Delta E, t) = \frac{1}{\pi}\frac{\Gamma/2}{\Delta E^2 + (\Gamma/2)^2}. \tag{6.53}$$

The oscillating term $\sin(2\Delta E t)$, which is responsible for preferentially emitting resonances with small ΔE, also governs the distribution of emission times. Classical simulations, which are typically based on Monte Carlo algorithms, cannot easily incorporate regions with negative probabilities as suggested by this form. The mean propagation time in a transport simulation could be altered to match the mean time of the quantum propagator,

$$\langle t \rangle = \frac{\int dt\ t\ \mathcal{R}(\Delta E, t)}{\int dt\ \mathcal{R}(\Delta E, t)} = \frac{\Gamma/2}{\Delta E^2 + (\Gamma/2)^2}. \tag{6.54}$$

However, the second moment for the time would not correspond to that expected for an exponential decay with the same average time.

$$\langle t^2 \rangle = \frac{1}{8}\frac{3\Gamma^2 - 4\Delta E^2}{\left(\Delta E^2 + \Gamma^2/4\right)^2} \neq 2\langle t \rangle^2. \tag{6.55}$$

Not only is this form inconsistent with exponential decay, $\langle t^2 \rangle$ can even become negative for resonances far off shell. This illustrates, on a formal level, the need for performing the quantum corrections described above.

Chapter 7

Balance Functions — A QGP Signal?

Balance functions were originally proposed to investigate hadronization in jets produced in proton-proton collisions [59, 60]. By studying what Drijard et al. called the "associated charge balance function" in a series of papers, they found that the leading hadrons carry information about the quantum numbers of scattered partons [60]. They further concluded that jet fragmentation is universal, i.e., that the "charge adjustment between the hadronic fragments and the partons is independent of the latter's quark content" [61].

Similar studies were performed with balance functions in the $e^+e^- \rightarrow 2$ jets annihilation processes. Leading particles in opposing jets were shown to be correlated across a long range [38]. These long range correlations were then employed to demonstrate that the primary quark of a jet ends up in the leading hadron [29, 8]. Short range correlations due to local quantum number conservation were used to study jet fragmentation. $K\bar{K}$ strangeness correlations and heavy hadron correlations were found to be a cleaner signal than electric charge correlations because, respectively, much fewer strange quarks are produced [8] and momentum distributions of heavier particles are less smeared [9]. These studies have largely confirmed the fragmentation models.

7.1 Balance Functions for Relativistic Heavy Ion Collisions

7.1.1 Theory

Bass, Danielewicz, and Pratt proposed balance functions as a signal that can distinguish between early-stage and late-stage hadronization [24]. The balance functions are calculated for a charge a and a balancing anti-charge b, which are created pairwise. They are defined as

$$\mathcal{B}(\Lambda_2|\Lambda_1) = \frac{1}{2}\left\{\frac{\langle N(\Lambda_2^b,\Lambda_1^a)\rangle - \langle N(\Lambda_2^a,\Lambda_1^a)\rangle}{\langle N(\Lambda_1^a)\rangle} + \frac{\langle N(\Lambda_2^a,\Lambda_1^b)\rangle - \langle N(\Lambda_2^b,\Lambda_1^b)\rangle}{\langle N(\Lambda_1^b)\rangle}\right\}, \quad (7.1)$$

where Λ_1^a signifies some condition involving particle type a, e.g. "π^+ detected anywhere", $N(\Lambda_1^a)$ is the number of particles of type a that satisfy condition Λ_1 in one event, and $N(\Lambda_2^b,\Lambda_1^a)$ is the number of particle pairs meeting both conditions simultaneously in a single event. The other terms are defined accordingly.

The width of the balance function can be used as an indicator for the average phase-space separation of charge–anti-charge pairs at freeze-out. This information can be used to infer the time scale at which hadronization takes place in a relativistic heavy-ion collision as much of the charge in a relativistic heavy-ion collision is created at hadronization. Early hadronization, at $\tau < 1$ fm/c, [131, 100], would result in a broader balance function because charge–anti-charge pairs that are created close to each other at an earlier time have a longer time to diffuse apart by scattering off other particles. In addition, the velocity gradients in the collision region are higher at early times, $dv/dz = 1/\tau$, which contributes significantly to the separation of the pair. A broad balance function indicating an early hadronization would rule out the possibility that a QGP is formed in relativistic heavy-ion collisions.

Late-stage hadronization is consistent with the formation of a QGP that would exist for some time during the collision before the partons are confined into hadrons. This late-stage creation of charge–anti-charge pairs leaves them less time to separate from each other

with significantly smaller velocity gradients in the collision region. This scenario would, thus, lead to a narrower balance function. However, a narrow balance function does not necessarily constitute a unique signal of delayed hadronization as there might exist some exotic mechanism that constrains charge–anti-charge pairs to stay close to one another.

Besides from the diffusive separation of charge–anti-charge pairs described above, the balance function width receives another contribution from the charge–anti-charge creation mechanism. An example for such a model is the widely-used Lund string fragmentation model [15, 13]. As the string fragments in the model, quark–anti-quark and diquark–anti-diquark pairs are produced and combined with other quarks or diquarks to form hadrons. The balancing charges of the quarks, thus, end up in hadrons separated by a distance on the order of 0.5 fm, when the hadrons are released from the string fragmentation. This initial spatial separation of the charge–anti-charge pair can lead to large separations in phase space in the final state because of the velocity gradients, which are particularly large during the early stages of the collision.

When using a detector with perfect acceptance, the extracted balance function Eq. (7.1) is normalized to unity, even if the multiplicity of the balancing charges a and b differ. Bass, Danielewicz, and Pratt ensured the latter property in the balance function by introducing the second term, which was missing from previous definitions:

$$\int d\Lambda_1\, d\Lambda_1\ \mathcal{B}(\Lambda_2,\Lambda_1) = \frac{1}{2}\left\{\frac{M_b M_a - M_a(M_a-1)}{M_a} + \frac{M_a M_b - M_b(M_b-1)}{M_b}\right\} = 1. \quad (7.2)$$

The normalization is different, when extracting balance functions from experimental data obtained with limited detector acceptance. This and other effects of limited detector acceptance on the balance function can be corrected for as discussed in [95].

7.1.2 Experiment

The STAR experiment at RHIC was the first to determine a balance function for a relativistic heavy-ion collision [27]. The electric charge balance function as well as the $\pi^+\pi^-$ balance function were studied. Condition Λ_1 of Eq. (7.1) was taken to indicate "anywhere in the detector", while Λ_2 signified "separated from the first particle by a pseudo-rapidity gap of $\Delta\eta$", where the pseudo-rapidity is defined as

$$\eta = \frac{1}{2}\log\frac{|\mathbf{p}| + p_z}{|\mathbf{p}| - p_z}. \tag{7.3}$$

In this case, the balance function can be written simply as a function of relative pseudo-rapidity only,

$$\mathcal{B}(\Delta\eta) = \frac{1}{2}\left\{\frac{\langle N_{ba}(\Delta\eta)\rangle - \langle N_{aa}(\Delta\eta)\rangle}{\langle N_a\rangle} + \frac{\langle N_{ab}(\Delta\eta)\rangle - \langle N_{bb}(\Delta y)\rangle}{\langle N_b\rangle}\right\}. \tag{7.4}$$

The STAR collaboration found that the the balance function narrows from peripheral to central collisions [28, 136]. This finding is consistent with the notion that the dynamics in a relativistic heavy-ion collision differs significantly between central and peripheral collisions. The narrow balance function in central collisions and wider balance function in peripheral collisions are consistent with the notion that the production of the QGP is more likely in the former than in the latter. To further substantiate this hypothesis, the experimental balance function width is compared to that extracted from the `Hijing` model [151, 86]. `Hijing` is essentially a Glauber-type model but also incorporates soft, non-perturbative QCD phenomenology. As a model, `Hijing` does not contain the production of a QGP. The balance functions are calculated from the `Hijing` model simulations and compared to the experimental data without further modification. The extracted balance function widths are essentially flat as a function of impact parameter as the dynamics of the superposition of pp collisions does not change from central to peripheral collisions. For peripheral collisions, the experimental data were matched by the model calculations within

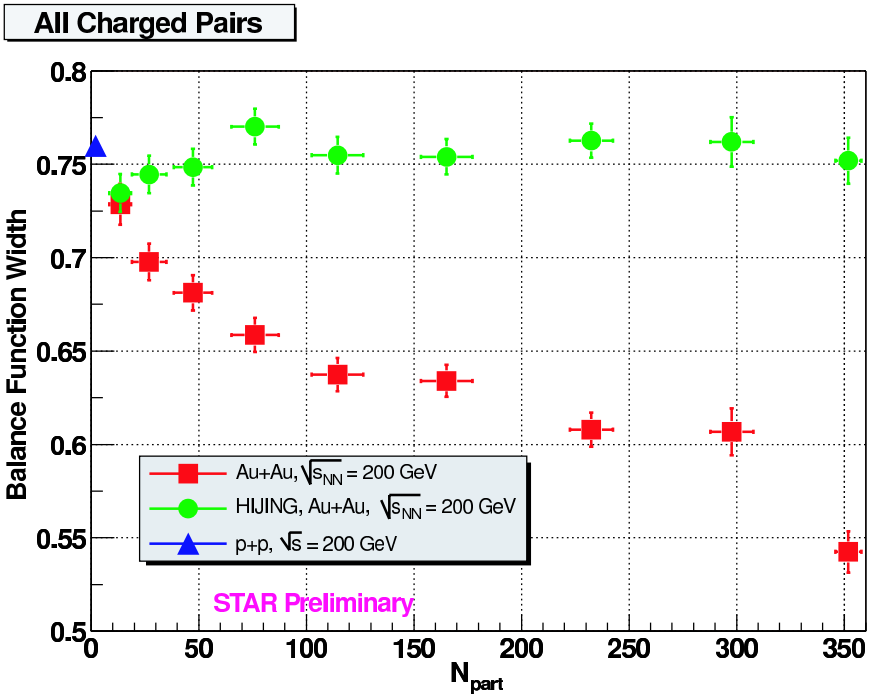

Figure 7.1: Width of the electric charge balance function for gold on gold collisions at $\sqrt{s_{NN}} = 200$ GeV as a function of the number of participants [136]. A peripheral collision involves a small number of participants, whereas a more central collision involves more participants. The narrowing of the balance function with increasing centrality is consistent with an increasingly delayed hadronization.

errors. For central collisions, however, the experimentally determined balance function was significantly narrower than the balance function from `Hijing`.

The result described above indicates that peripheral relativistic heavy-ion collisions follow the dynamics of well-known pp reactions, whereas central collisions of heavy ions create some new phenomena. Yet, there needs to be more certainty in the model calculations to rule out any source, other than late-stage hadronization, for the narrowing of the balance function in central collisions. Such studies are essential to firmly establish signals of the QGP. One issue, to be investigated in the following, is the question how the lack of hadronic rescattering in the `Hijing` model affects the extracted balance function.

7.2 Model Calculations with Hadronic Rescattering

The `Hijing` model, which was used to extract a balance function as theoretical comparison to the experimental balance function, does not include hadronic rescattering and hence does not accurately describe the hadronic evolution of a relativistic heavy-ion collision. The difference noted between the model calculations and the experimentally determined balance function may conceivably be attributed to this deficiency in the model. To move further toward establishing the existence of a QGP, balance functions should be calculated from a simulation, in which `Hijing` is complemented with a simple model for hadronic rescattering. In practice, an event is created first with `Hijing` and then fed into a Gromit model with a set of particle types corresponding to `Hijing`'s and with elastic and resonance interactions between those particles. 24,400 simulated events are used to calculate the $\pi^+\pi^-$ balance function in relative rapidity and in

$$q_{\text{inv}}^2 = (p_1 - p_2)^2 \tag{7.5}$$

as well as the electric charge balance function in relative pseudo-rapidity.

With perfect detector acceptance, the $\pi^+\pi^-$ balance function in relative rapidity turns out to be broader with hadronic rescattering than without, as can be seen in Figure 7.2. The statistical errors in Figure 7.2, which are smaller than the symbols, are calculated according to

$$\delta\mathcal{B}(\Delta y) = \frac{1}{2\sqrt{N_{\text{events}}}}\sqrt{\frac{\langle N_{ba}(\Delta y)\rangle + \langle N_{aa}(\Delta y)\rangle}{\langle N_a\rangle^2} + \frac{\langle N_{ab}(\Delta)\rangle + \langle N_{bb}(\Delta)\rangle}{\langle N_b\rangle^2}}. \tag{7.6}$$

The width of the balance function, shown in Table 7.1, can be quantified with the aid of

$$\langle \Delta y\rangle = \frac{\sum_i \Delta y_i B_i}{\sum_i B_i}, \tag{7.7}$$

where Δy_i is the mid-value in the rapidity difference bin. The statistical error of this balance function width is obtained with

$$\delta\langle \Delta y\rangle = \langle \Delta y\rangle \sqrt{\frac{\sum_i \Delta y_i^2 \delta B_i^2}{(\sum_i \Delta y_i B_i)^2} - 2\frac{\sum_i \Delta y_i \delta B_i^2}{(\sum_i B_i)(\sum_i \Delta y_i B_i)} + \frac{\sum_i \delta B_i^2}{(\sum_i B_i)^2}}. \tag{7.8}$$

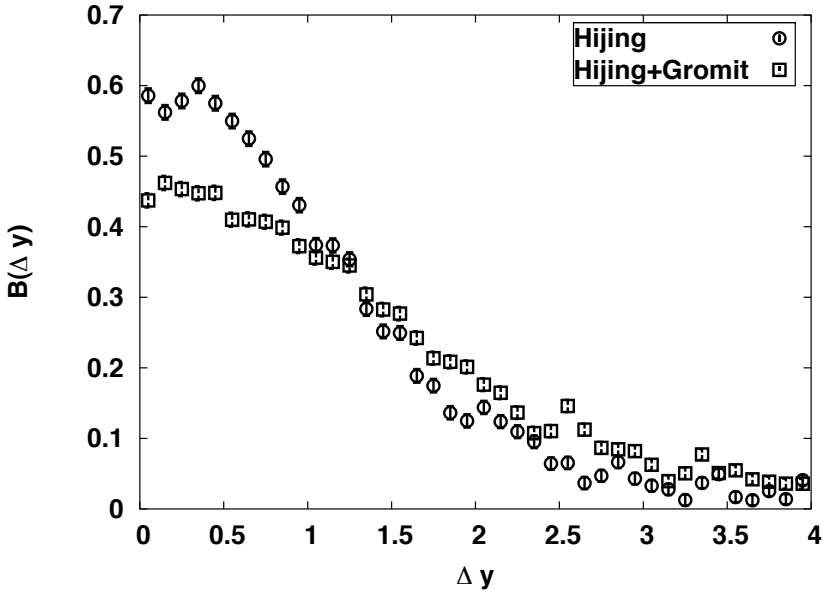

Figure 7.2: Pion balance function in relative rapidity from `Hijing` and `Hijing` + Gromit without acceptance cuts.

Variable	Model	Width
Rapidity	`Hijing`	0.893 ± 0.016
	`Hijing+Gromit`	1.160 ± 0.016
q^2_{inv}	`Hijing`	0.718 ± 0.013 GeV^2
	`Hijing+Gromit`	0.646 ± 0.012 GeV^2

Table 7.1: Summary of balance function widths without acceptance cuts.

Results for the balance function in q^2_{inv} are shown in Figure 7.3 and Table 7.1. They indicate that the width of the balance function decreases by a small amount due the inclusion of hadronic rescattering. This narrowing can be attributed to the cooling induced by the hadronic rescattering. It should be noted that with infinite hadronic rescattering, i.e., vanishing mean free path for hadrons, the width of the balance function in q^2_{inv} would be even narrower. In that case, the diffusive contribution to the width of the balance function would vanish, leaving only the contribution due to the particle creation mechanism.

The pronounced peak in the balance function around $q^2_{\text{inv}} \approx 0.52$ GeV in Figure 7.3 is a manifestations of a strong $\pi^+\pi^-$ correlation due to a resonance decay. The position of the

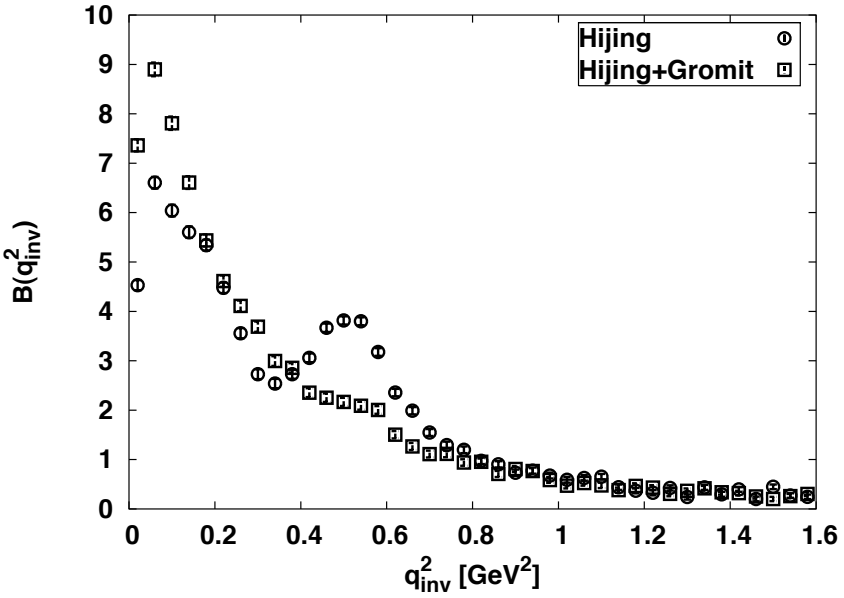

Figure 7.3: Pion balance function in $q^2_{\rm inv}$ from `Hijing` and `Hijing` + Gromit without acceptance cuts.

peak corresponds to an invariant mass of around 773 MeV, close to the pole mass of the ρ mesons. Hence, the correlations in the peak arise from the decay of the ρ^0 meson into a $\pi^+\pi^-$ pair.

In summary, it is found that the balance function as a function of relative rapidity is widened, when hadronic rescattering is included, but slightly narrowed as a function of $q^2_{\rm inv}$. These seemingly contradictory results can be explained as a result of the cooling of the system. For small relative rapidity Δy

$$q^2_{\rm inv} \approx m_t^2 (\Delta y)^2, \tag{7.9}$$

where the transverse mass is defined by

$$m_t = \sqrt{E^2 - p_z^2}. \tag{7.10}$$

Hadronic interactions cool the particles as the system performs work on the longitudinal expansion of the collision region, thus leading to a lower transverse mass. If the average separation of the particle–anti-particle pairs in $q^2_{\rm inv}$ decreases less than the transverse mass,

then, by Eq. (7.9), the separation in rapidity has to increase. This explains the different findings for the balance function widths and implies that the balance function in q^2_{inv} is the cleaner observable.

7.2.1 Accounting for Experimental Acceptance

The discussion in the previous subsection assumed a perfect detector, neglecting the unavoidable limited acceptance of real experiments. The effects of a limited acceptance are studied here by passing particles through a simulated acceptance filter of the STAR detector. One of the main features of this acceptance filter is to reject particles with large pseudo-rapidity $|\eta| \geq 1.3$ and/or high transverse momenta $p_t = \sqrt{|\mathbf{p}|^2 - p_z^2} \geq 700$ MeV. Only particles that pass this filter will then be used in the calculation of the balance functions. These calculations start form the same $24,400$ simulated events as above in order to arrive at comparable results.

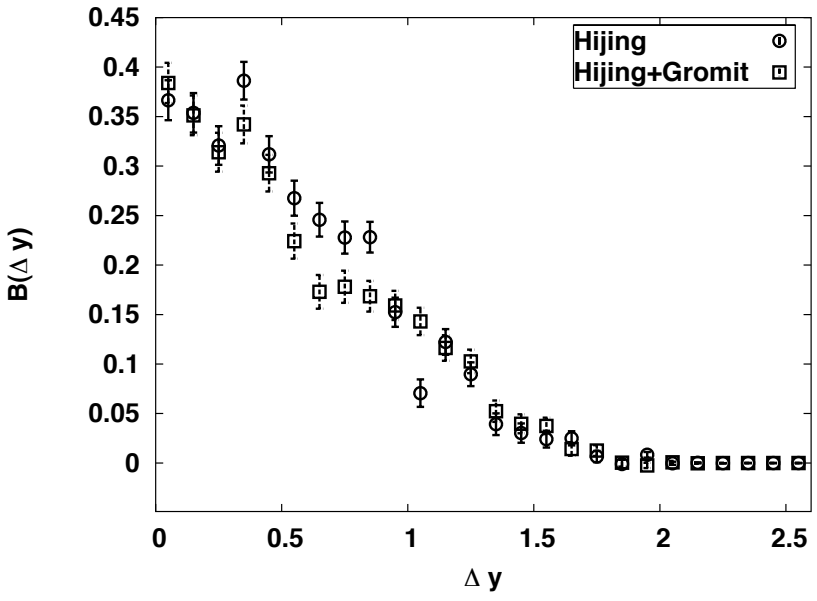

Figure 7.4: Pion balance function in relative rapidity from `Hijing` and `Hijing` + Gromit with STAR acceptance cuts.

When the STAR acceptance cuts are applied, the $\pi^+\pi^-$ balance function in relative

rapidity, shown in Figure 7.4 and Table 7.2), displays nearly the same width, with or without hadronic interactions. This indicates that the same pions that are rejected by the acceptance filter, are also linked to the widening of the balance function in relative rapidity, when a perfect acceptance is assumed. The rejected pions are characterized by high p_t, and/or large pseudo-rapidity and are most affected by the cooling due to hadronic rescattering. This underscores the hypothesis stated in the previous subsection that cooling is responsible for the widening of the balance, when hadronic interactions are included.

Variable	Model	Width
Rapidity	`Hijing`	0.541 ± 0.009
	`Hijing+Gromit`	0.550 ± 0.009
Pseudo-rapidity	`Hijing`	0.628 ± 0.010
	`Hijing+Gromit`	0.675 ± 0.010
q^2_{inv}	`Hijing`	0.262 ± 0.005 GeV^2
	`Hijing+Gromit`	0.163 ± 0.005 GeV^2

Table 7.2: Summary of balance function widths with STAR acceptance cuts.

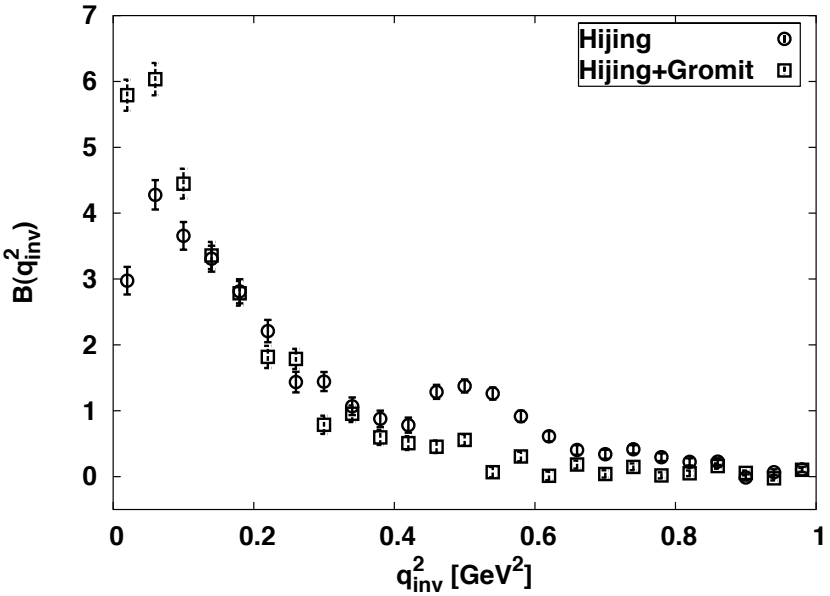

Figure 7.5: Pion balance function in q^2_{inv} from `Hijing` and `Hijing` + Gromit with STAR acceptance cuts.

The balance function in q^2_{inv} for pions filtered by the STAR acceptance confirms the

previous finding that the width of the balance function is not affected by hadronic interactions, as can be seen in Figure 7.5 and Table 7.2. The same is found again when calculating

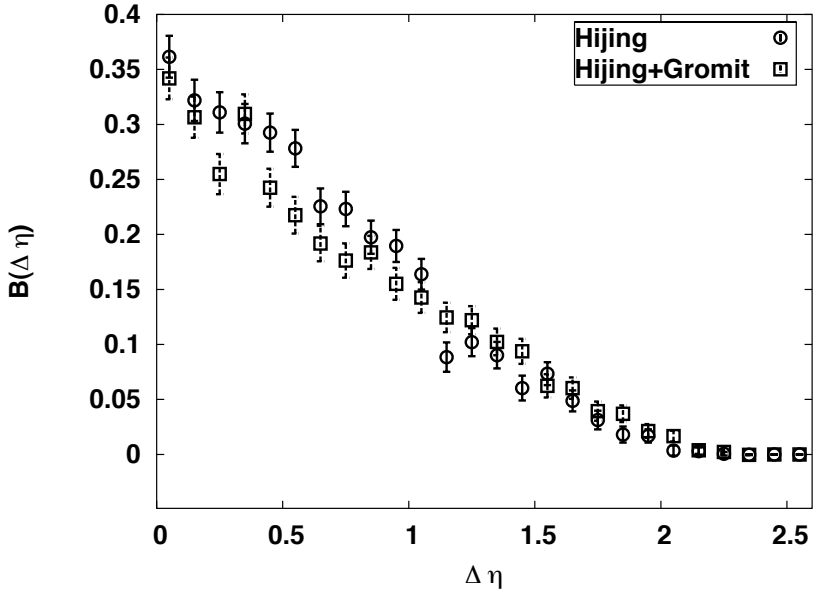

Figure 7.6: Pion balance function in relative pseudo-rapidity from `Hijing` and `Hijing` + Gromit with STAR acceptance cuts.

the electric charge balance function as shown in Figure 7.6.

7.3 Corrections for Net Charge

The definition of the balance function Eq. (7.1) assumes that all charges are produced in pairs, i.e. there is no net charge in the system. Nevertheless, due to the presence of unbalanced protons and neutrons in the colliding nuclei in a relativistic heavy-ion collision, there are net charges like electric charge and baryon number. Much of the quantum numbers of the colliding nuclei in a relativistic heavy-ion collision at RHIC energies are carried by leading baryons. For instance, the ratio of the proton yield to the anti-proton yield in the mid-rapidity region was measured by the STAR collaboration to be $0.65 \pm 0.01_{(\text{stat})} \pm 0.07_{(\text{syst})}$ at RHIC energies [6], indicating that few initial protons are left in the center of the collision region. In a typical experiment with relativistic heavy-ion col-

lision, the detector acceptance does not cover the leading baryons so that those net charges do not affect the balance functions. This can be seen in Figure 7.6, which displays the electric charge balance function that was calculated using the STAR acceptance filter.

Any correlation among the excess charges would dominate the balance function if Eq. (7.1) were used to calculate the balance function with a perfect detector acceptance. This effect is illustrated in Figure 7.7, where the electric charge balance function is shown

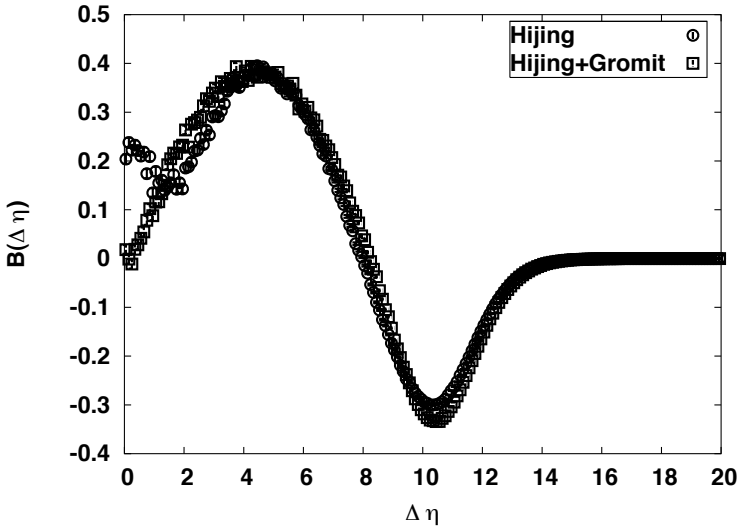

Figure 7.7: Uncorrected balance function in relative pseudo-rapidity from `Hijing` and `Hijing` + Gromit for all electric charges.

to be heavily dominated by the $p\bar{p}$ contribution. These correlation can be seen in isolation in the $p\bar{p}$ balance function shown in Figure 7.8. The $p\bar{p}$ balance function exhibit strong correlations at $\Delta\eta = 0$ and at $\Delta\eta = 10$ as the protons from the incident nuclei are mainly concentrated around $\eta = \pm 5$ at RHIC energies. A balance function such as shown in Figure 7.7 does not reveal the pair correlation of interest and is little use as a signal of late-stage hadronization.

The complication of net charges as pointed out above can amount to a serious impediment for the use of balance functions, even if the acceptance cuts of real detectors effectively removed the leading baryons which carry most of the net charge. After all, there

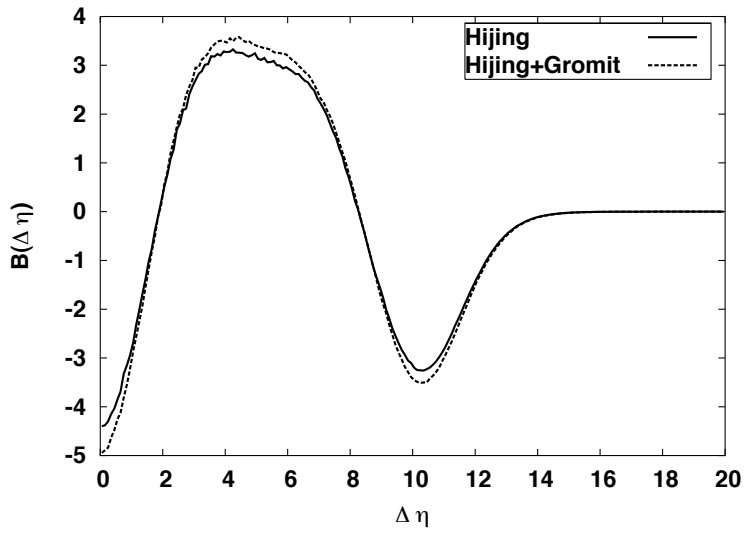

Figure 7.8: Uncorrected balance function in relative pseudo-rapidity from `Hijing` and `Hijing` + Gromit for protons and anti-protons.

still are contributions from net charges in the mid-rapidity region because it is not entirely baryon free, i.e. there are more baryons than anti-baryons, as evident from the ratio of the proton yield to the anti-proton yield. Furthermore, net charges do not only exist for Coulomb charge or baryon number, there is also a small excess of negative pions over positive pions. This discrepancy arises as the initial nuclei contain more neutrons than protons which leads to a negative net isospin. In order to conserve isospin more negative pions are produced than positive pions. Therefore, removing the contributions of excess charges would significantly improve the balance functions as a signal.

To derive such a corrected balance function, it is assumed that there are two independent sources, one source that creates a certain particle type b "unpaired", i.e., individually and independently from other particles, and another source that creates particles in charge–anti-charge pairs ab. It is also supposed that the particles in the final state can be associated uniquely with either source. In this case, the particle numbers from Eq. (7.1) can be written

in term of separate contributions from each source.

$$N_a = N_a^p, \tag{7.11}$$

$$N_b = N_b^p + N_b^u, \tag{7.12}$$

where N_b^u is the number of particles from the unpaired source and $N_b^p = N_a^p$ the number of particles that were created in pairs. The pair counting terms in Eq. (7.1) count pairs irrespective of their origin. However, for the purposed of this discussion, the counted pairs need to be separated into classes based on the original source of the particles. In short notation

$$N_{aa} = N_{aa}^{pp}, \tag{7.13}$$

$$N_{ab} = N_{ab}^{pp} + N_{ab}^{pu}, \tag{7.14}$$

$$N_{ba} = N_{ba}^{pp} + N_{ba}^{up}, \tag{7.15}$$

$$N_{bb} = N_{bb}^{pp} + N_{bb}^{up} + N_{bb}^{pu} + N_{bb}^{uu}, \tag{7.16}$$

where N_{ba}^{up} refers to the number of particle pairs ba, where b originated from the unpaired source and a from the paired source and the other terms are defined accordingly. The goal is to define a balance function that only contains contributions from paired terms, which is, therefore, independent of net charges. In addition, the corrected balance function should yield the same result as in Eq. (7.1) in the case where the unpaired source does not produce any particles.

First, the two different denominators in Eq. (7.1) are replaced by a single denominator N_a^p to remove the particle number from the unpaired source. The combination of the four pair counting terms in Eq. (7.1) should be preserved as closely as possible, since they remove other event correlations like anisotropic flow and jets. Instead of altering the pair counting term, the unwanted terms are subtracted from the numerator $\langle N(\Lambda_2^b, \Lambda_1^a)\rangle - \langle N(\Lambda_2^a, \Lambda_1^a)\rangle + \langle N(\Lambda_2^a, \Lambda_1^b)\rangle - \langle N(\Lambda_2^b, \Lambda_1^b)\rangle$. The contribution of N_{ab}^{pu} equals N_{bb}^{pu} because

paired particles ab are created with the same probability distribution, regardless whether they are of type a or b. The two terms cancel in the balance function. The same holds for N_{ba}^{up} and N_{bb}^{up}, which leaves N_{bb}^{uu} as the sole term that needs to be subtracted. Symbolically, N_{bb}^{uu} can be written as

$$N_{bb}^{uu} = \underbrace{(N_b^u)}_{i} \otimes \underbrace{(N_b^u)}_{j \neq i} \tag{7.17}$$

to signify that unpaired particles are checked against other unpaired particles when building the histogram for the number of pairs. The expression $j \neq i$ is a reminder that a particle must not be correlated with itself. Since the emission of unpaired particles is assumed to be independent, the second set of particles may be taken from a different event with the same multiplicity of particle types a and b

$$N_{bb}^{uu} = \underbrace{(N_b^u)}_{\text{from one event, } i} \otimes \underbrace{(N_b^u)}_{\text{from another event, } j \neq i} \tag{7.18}$$

Practically, it is impossible to discern which source, paired or unpaired, a particle originated from. The distribution of unpaired particles b is equal to the distribution of all particles b minus that of paired particles b or a. Therefore

$$N_{bb}^{uu} = \underbrace{(N_b \ominus N_a)}_{\text{from one event, } i} \otimes \underbrace{(N_b \ominus N_a)}_{\text{from another event, } j \neq i} \quad . \tag{7.19}$$

The event mixing is necessary to avoid reintroducing the pair correlations between particles from the same event. The expression from Eq. (7.19) can be rewritten in term of particle pairs from mixed events

$$N_{bb}^{uu} \longrightarrow \langle N'(\Lambda_2^b, \Lambda_1^b) \rangle - \langle N''(\Lambda_2^b, \Lambda_1^a) \rangle + \langle N''(\Lambda_2^a, \Lambda_1^a) \rangle - \langle N'(\Lambda_2^a, \Lambda_1^b) \rangle \tag{7.20}$$

where $N'(\Lambda_2^b, \Lambda_1^b)$ counts the number of pairs from mixed events that satisfy the two conditions simultaneously, $N''(\Lambda_2^a, \Lambda_1^a)$ means the same, except that particles with the same index

are not counted. Finally, the corrected balance function is given by

$$B(\Lambda_2|\Lambda_1) = \frac{1}{2}\Bigg\{ \frac{\langle N(\Lambda_2^b,\Lambda_1^a)\rangle - \langle N(\Lambda_2^a,\Lambda_1^a)\rangle + \langle N(\Lambda_2^a,\Lambda_1^b)\rangle - \langle N(\Lambda_2^b,\Lambda_1^b)\rangle}{\langle N(\Lambda_1^b)\rangle} \tag{7.21}$$

$$- \frac{\langle N''(\Lambda_2^b,\Lambda_1^a)\rangle - \langle N''(\Lambda_2^a,\Lambda_1^a)\rangle + \langle N'(\Lambda_2^a,\Lambda_1^b)\rangle - \langle N'(\Lambda_2^b,\Lambda_1^b)\rangle}{\langle N(\Lambda_1^b)\rangle} \Bigg\}.$$

To test this new expression, the corrected balance function is calculated for the worst case of $p\bar{p}$ balance functions, where the net charge plays the most important role. The results in Figure 7.9 show a dramatic difference to the balance functions calculated with the original definition in Eq. (7.1), which were shown in 7.8. The effects of proton concentrations at $\eta = \pm 5$ have been removed completely.

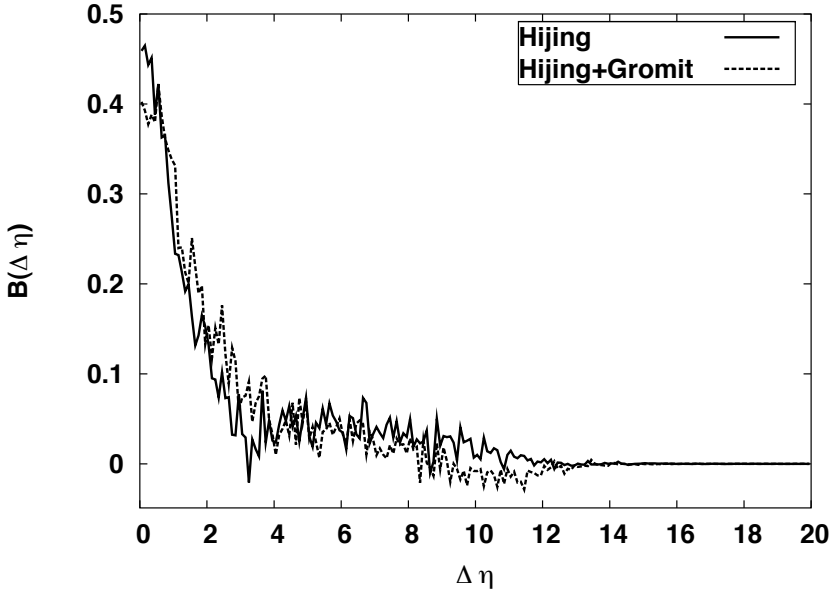

Figure 7.9: Corrected $p\bar{p}$ balance function in relative pseudo-rapidity from `Hijing` and `Hijing` + Gromit.

With this result, the corrected form for the balance function can now be used to calculate the electric charge balance function with a perfect detector acceptance, as illustrated in Figure 7.10. The balance functions are evidently wider under the influence of hadronic rescattering. This is consistent with the similar finding from section 7.2 about the $\pi^+\pi^-$ balance function in relative rapidity.

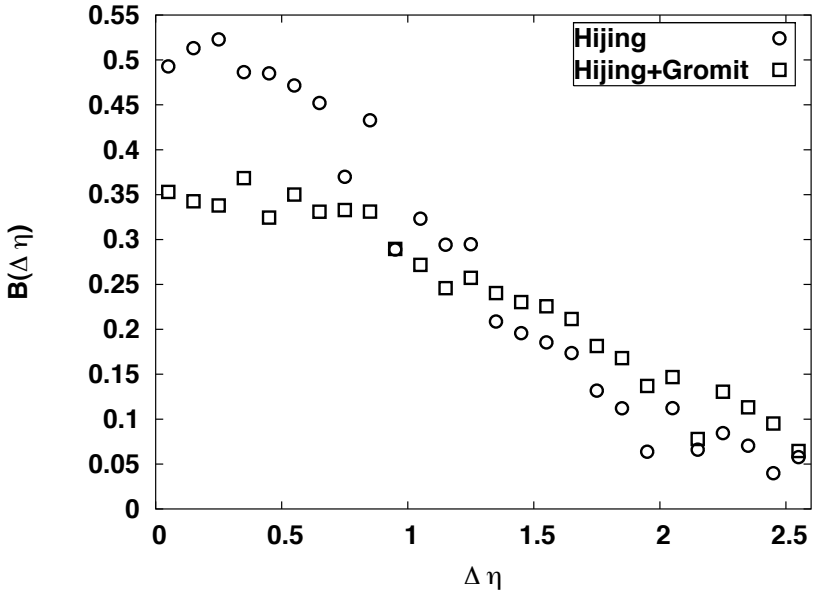

Figure 7.10: Corrected electric charge balance function in relative pseudo-rapidity from `Hijing` and `Hijing` + Gromit.

Since in relativistic heavy-ion collisions, the multiplicity of π^- is greater than π^+, the influence of the net pion charge on $\pi^+\pi^-$ balance function needs to be investigated. The calculations from Section 7.2 are repeated with the expression for the corrected balance function and shown in Figures 7.11 and 7.12. Little change is found in the shape of the $\pi^+\pi^-$ balance function. The calculated widths of the corrected balance functions, $\langle \Delta y \rangle = 1.121$ for `Hijing` and $\langle \Delta y \rangle = 1.379$ for `Hijing` + Gromit, are larger than the widths of the balance functions in the original definition, Table 7.1. However, the absolute width is of little interest in this study. The main focus is the comparison of the relative balance function width with hadronic rescattering to the case without. Even with the corrected balance function, the width is still larger with hadronic scattering than without.

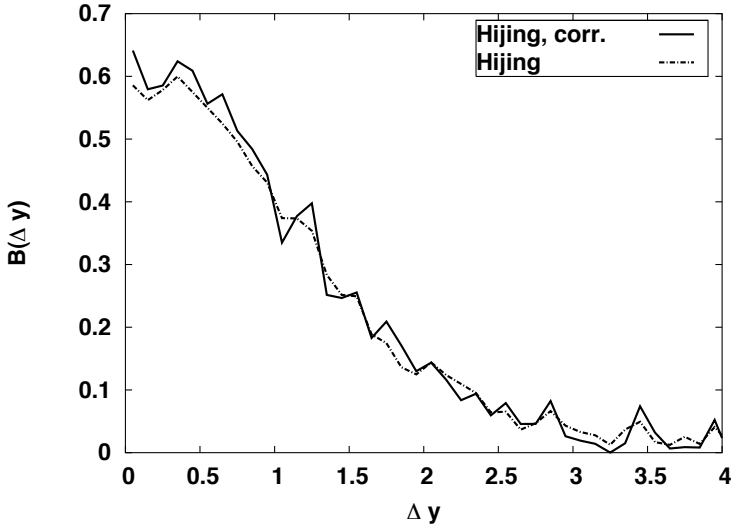

Figure 7.11: Comparison between corrected and original $\pi^+\pi^-$ balance function in relative rapidity from `Hijing`.

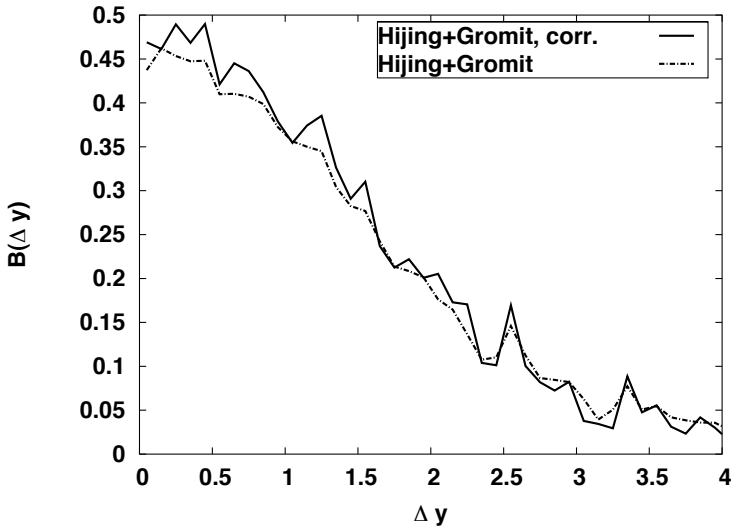

Figure 7.12: Comparison between corrected and original $\pi^+\pi^-$ balance function in relative rapidity from `Hijing` + Gromit.

Chapter 8

Conclusions

Experiments with relativistic heavy-ion collisions offer the possibility of studying some predicted, but difficult to observe, QCD phenomena, two of which were discussed in this thesis: the phase transition from hadronic matter to the quark-gluon plasma (QGP) and the restoration of chiral symmetry. Neither effect is directly accessible by experiments due to the small scale of the collision region in both space and time. Hence, the existence of the phase transitions must be established from the information contained in the collision debris recorded by the detectors. The complexity of both the underlying theory of QCD and the dynamics in relativistic heavy-ion collisions make theoretical treatments from first principles intractable. This difficulty is further compounded by the distortion of any effect, which is predicted to result from the phase transitions, in the collision dynamics. Consequently, much theoretical insight on relativistic heavy-ion collision is deduced from analytical as well as Monte Carlo models. In this thesis, new models were contributed for the study of relativistic heavy-ion collisions and phenomena associated with them.

In Chapter 2, alternative sources for anomalous isospin fluctuations other than disoriented chiral condensates (DCC) were studied by considering the influence of total isospin conservation, quantum symmetrization, and resonance decays. For this purpose, novel expressions were obtained for the multiplicity distributions and the isospin fluctuations for

a canonical ensemble, in which total isospin as well as additive quantum numbers are exactly conserved. The formalism was extended to include both pions and resonances and can account for Bose-Einstein symmetrization of the pion wavefunction. Numerical calculations were then performed to study the effects of total isospin conservation, quantum symmetrization, and resonance decays on the width of the multiplicity distribution, which can be squared to obtain the isospin fluctuations. The widths of the multiplicity distributions are found to be largely dominated by the behavior of the tails, thus making it imperative to perform exact calculations. Such calculations were made possible by recursion relations that circumvent the summation over the immense number of partitions in the partition functions.

It was found that conservation of total isospin and its projection has little effect on the width of the multiplicity distributions, when the systems are larger than a dozen particles. At high phase-space densities, inclusion of Bose-Einstein symmetrization leads to a multiplicity distribution that is much broader than a random distribution. However, addition of resonances more than compensates for this broadening and narrows the multiplicity distribution below the width of the random distribution. Both effects are small when the phase space density is below 0.1 fm^{-3}.

Another indicator for the restoration of chiral symmetry was studied in Section 4.3. Resonance mass distributions are believed to broaden and shift toward lower invariant mass in an environment with restored chiral symmetry. The ρ meson with its relatively short lifetime would be a good probe for such modifications to the resonance properties, if the decaying ρ mesons from the initial state are replenished through formations from two pions. A model based on the Gromit framework was used to gain insight into such a regeneration of ρ mesons in the collision dynamics. It was found that the ρ is sufficiently regenerated to supply probes at all stages of the collision. Furthermore, the regeneration of ρ mesons is sensitive to the existence of hadrons at the early, hot and dense phase of a relativistic

heavy-ion collision. A larger number of ρ mesons reconstructed from lepton pairs from a relativistic heavy-ion collision than from a cocktail of nucleon-nucleon collisions would indicate the existence of hadrons at early stages, which is inconsistent with the formation of a QGP.

The Gromit framework for microscopic transport models based on the Boltzmann transport equation was introduced in Chapter 3. It provides a general framework that can be used for any degrees of freedom and any interaction; it is expandable, modular, transparent, and easy to debug and maintain. Gromit, therefore, provides a common framework that can be used to study the different stages of a relativistic heavy-ion collision at RHIC energies with their vastly different dynamics.

Like some other Boltzmann transport models the Gromit framework introduces an arbitrary model parameter, the sampling factor λ, which has a profound effect on the extracted results. These effects were investigated in Chapter 4 for simplified models and shown for particle spectra and elliptic flow, to vanish in the Boltzmann limit, $\lambda \to \infty$. Large sampling factors were also found to eliminate sensitivities to a variety of arbitrary choices inherent to Boltzmann-type simulations and to solve a variety of problems related to acausal propagation. This is linked to the reduction of the interaction range between particles in the simulation that restores the locality of interactions.

In nature, nevertheless, particles indeed interact over a finite range, either by exchange of off-shell particles or through a mutual interaction through classical fields. Therefore, Chapter 5 sought to understand the degree to which these effects are physical as opposed to representing numeric artifacts. Nonlocal effects were interpreted in terms of viscous parameters, allowing the incorporation of nonlocal effects into hydrodynamic models in a straight-forward manner. Knowing the viscous parameters also provides criteria for tuning Boltzmann algorithms so that they are consistent with quantum transport considerations.

The tuning can be accomplished by either changing the sampling factor or by adjusting the scattering algorithms. The simple manner in which the viscous parameters scale with density and cross section should simplify such a procedure.

As transport theories address the first one fm/c of a relativistic heavy-ion collision, the role of nonlocal interactions becomes increasingly important. For times above 2 fm/c, it is unlikely that the nonlocalities play any significant role as the effects scale as τ^{-3}. Since the nuclei pass one another at RHIC in less than 0.2 fm/c, whereas cross sections approach a square fm, nonlocal effects might provide a nonnegligible source of stopping as the viscous drag converts longitudinal collective velocity to heat. The role for such effects in the stopping phase at LHC collisions should be even greater.

The influence of resonance decays on correlation function were studied in Chapter 6. A new method was proposed to correctly calculate correlation functions from semi-classical models, exploiting the source function of the resonance and its creation point in spacetime as opposed to the creation points of the final-state pions. This method is easily applicable to generate correlation functions from the event histories of simulations. When using direct pions, the creation points of the final-state pions provide all the necessary information for creating correlation functions. By considering the creation points of the resonances that decayed into the final-state pions, all spacetime points at which the resonance might have decayed were coherently accounted for by modifying the prescription for generating correlation weights.

It was found that the proposed modification is important only for sources that are quantum-mechanical in nature. If the source is large and the product of the momentum and spatial uncertainties are large, $\Delta p\, \Delta x \gg \hbar$, the behavior of the correlation function is dominated by the exponential term that is determined by the points at which the resonance is created. Quantum considerations in resonant decays could play an important role when

considering the decay of small sources that push the limits of the uncertainty principle. However, such sources are also accompanied by questions regarding the quantum nature of the source functions responsible for initial creation of the resonances, i.e., the smoothness approximation might not be justified. For such problems, unless the off-shell behavior of the source functions is known, as in the case of a thermal model, the treatments presented here address only half the problem.

In Chapter 7, the Gromit framework was also used to explore the influence of hadronic interactions on balance functions, a new observable that has been proposed as a possible signal of late-stage hadronization. It was found that hadronic interactions widen the $\pi^+\pi^-$ balance function in relative rapidity, but not in q^2_{inv}. These seemingly contradictory results can be explained as a kinematic consequence of a cooling of the collision region due to hadronic rescattering.

Furthermore, it was demonstrated that previous definitions of balance functions are applicable only for a vanishing net charge. A new formalism for constructing balance functions in the presence of net charges was introduced and studied numerically. Though not entirely efficient, the new balance function was shown to remove even the dramatic effects of the net electric charge of the protons in a relativistic heavy-ion collision. Finally, for $\pi^+\pi^-$ the width, not so much the shape, of the balance functions were found to be somewhat affected by the new formalism. This can have implications for other studies but does not alter the conclusions about the effects of hadronic rescattering mentioned above.

Appendix

Appendix A

Parameter Definitions for Numerical Simulations

A.1 Initialization File for Pionwind Study

```
# specifications for pionwind calculation
particles {
   add Species N  { mass = 0.938; maxXS= 10; pdgId= 2212; baryon= 1;}
   add Species pi { mass = 0.1396; maxXS= 10; pdgId= 211; }
}
collisions {
   add PionWindModel {
   xs = 10;
#  collisions = pi pi, pi N;  # comment out to disable N N
   }
}
run {
   t0 = 1; tf = 64;
   rand = R250 { }
   events = 4;
   testParticles = 32;
   initCond = BjorkenInitCond {
      T = { pi=0.165, N=0.180 }
      N = { pi=2400, N=240 }
      posDist = Radial { etamin = -2; etamax = 2; rmax = 5; }
   }
   generator= TauEtaGenerator {
      boundary_cond=          simple;
      mesh_min=               {-10,-10,-4};
      mesh_max=               {10,10,4}
      collision_file=         col.out;
   }
}
```

```
analysis {
   add Histogram {
      variable = mt - m; weight = 1/(2*PI*mt);
      species = pi;
      xrange = [0, 2]; xstep = 0.05; format = "%.3f %10.4f %10.4f";
      acceptance = Interval { range = [-0.5, 0.5]; variable = y; }
      file = "pi.mt";
   }
   add Histogram {
      variable = mt - m; weight = 1/(2*PI*mt);
      species = N;
      xrange = [0, 2]; xstep = 0.05; format = "%.3f %10.4f %10.4f";
      acceptance = Interval { range = [-0.5, 0.5]; variable = y; }
      file = "N.mt";
   }
}
```

A.2 Initialization File for Balance Function Study

```
loadlib "~/lib/libhijing.so";
particles {
   add PDG {
      names = gamma, D, D_s, pi, K, eta, rho, omega, K*, eta',
              f_0, a_0, phi, h_1, b_1, a_1, f_2,
              N, Lambda, Sigma, Xi, Delta, Sigma*, Xi*, Omega
   }
}
decays {
   load "tables/resonances.tbl";
}
collisions {
   add ResonanceDecayInverter { }  # 76 resonance formation channels
   add AddQuarkModel { }           # 2775 elastic channels
}
run {
   t0 = 1;
   tf = 1000;
   rand = R250 { }
   events = 100;
   initCond = HijingInitCond {
      bmin = 0; bmax = 0; # min and max impact parameter
      targ = A; targA = 197; targZ = 79;  # target (Au)
      proj = A; projA = 197; projZ = 79;  # projectile (Au)
      frame = CMS; # frame of calculation, do not change
      eframe = 200; # cms energy
      particlesToPropagate = hadrons; # propagate hadrons or partons
      hadronDecay = 1;      # decay hadrons via jetset
      jetQuenching = 0;     # jet quenching, turn off
      nuclearShadowing = 1; # nuclear shadowing is on
      softRad = 1;          # soft radiation is on
      baryonJunction = 0;   # baryon junctions are temporarily off
   }
   generator= TauEtaGenerator {
      boundary_cond=          simple;
      min_cell_width=         {.625, .625, .625};
      mesh_min=               {-10,-10,-6};
      mesh_max=               {10,10,6}
   }
}
analysis {
   add CustomOutput { when= initial; file= initial.out; }
   add CustomOutput { when= final; file= final.out; }
}
```

Bibliography

Bibliography

[1] S. Abachi et al. Observation of the top quark. *Phys. Rev. Lett.*, 74:2632–2637, 1995.

[2] F. Abe et al. Observation of top quark production in $\bar{p}p$ collisions with the collider detector at fermilab. *Phys. Rev. Lett.*, 74:2626–2631, 1995.

[3] P. Abreu et al. Two-dimensional analysis of the Bose-Einstein correlations in e^+e^- annihilation at the Z0 peak. *Phys. Lett.*, B471:460–470, 2000.

[4] K. H. Ackermann et al. Elliptic flow in Au + Au collisions at $\sqrt{s_{NN}} = 130$ GeV. *Phys. Rev. Lett.*, 86:402–407, 2001.

[5] C. Adler et al. Elliptic flow from two- and four-particle correlations in Au + Au collisions at $\sqrt{s_{NN}} = 130$ GeV. [nucl-ex/0206001], 2002.

[6] C. Adler et al. Mid-rapidity anti-proton to proton ratio from Au + Au collisions at $\sqrt{s_{NN}} = 130$ GeV. *Phys. Rev. Lett.*, 86:4778–4782, 2001.

[7] J. Aichelin. Can one extract source radii from transport theories? *Nucl. Phys.*, A617:510, 1997.

[8] H. Aihara et al. Observation of strangeness correlations in e^+e^- annihilation at $\sqrt{s} = 29$ GeV. *Phys. Rev. Lett.*, 53:2199, 1984.

[9] H. Aihara et al. Study of baryon correlations in e^+e^- annihilation at 29 GeV. *Phys. Rev. Lett.*, 57:3140, 1986.

[10] N. S. Amelin et al. Collectivity, energy density and baryon density in pb on pb collisions. *Phys. Lett.*, B261:352–356, 1991.

[11] A. A Amsden, G. F. Bertsch, F. H. Harlow, and J. R. Nix. Relativistic hydrodynamic theory of heavy ion collisions. *Phys. Rev. Lett.*, 35:905–908, 1975.

[12] Anthony A. Amsden, Francis H. Harlow, and J. Rayford Nix. Relativistic nuclear fluid dynamics. *Phys. Rev.*, C15:2059–2071, 1977.

[13] Bo Andersson, G. Gustafson, G. Ingelman, and T. Sjostrand. Parton fragmentation and string dynamics. *Phys. Rept.*, 97:31, 1983.

[14] Bo Andersson, G. Gustafson, and B. Nilsson-Almqvist. A model for low p(t) hadronic reactions, with generalizations to hadron - nucleus and nucleus-nucleus collisions. *Nucl. Phys.*, B281:289, 1987.

[15] Bo Andersson, G. Gustafson, and T. Sjostrand. A model for baryon production in quark and gluon jets. *Nucl. Phys.*, B197:45, 1982.

[16] A. A. Anselm. Classical states of the chiral field and nuclear collisions at very high-energy. *Phys. Lett.*, B217:169–172, 1989.

[17] A. A. Anselm and M. G. Ryskin. Production of classical pion field in heavy ion high-energy collisions. *Phys. Lett.*, B266:482–484, 1991.

[18] N. Armesto, C. Pajares, and D. Sousa. Analysis of the first RHIC results in the string fusion model. *Phys. Lett.*, B527:92–98, 2002.

[19] P. Avery et al. Bose-Einstein correlations in e^+e^- annihilations in the Upsilon region. *Phys. Rev.*, D32:2294–2302, 1985.

[20] A. M. Baldin, L. A. Didenko, V. G. Grishin, A. A. Kuznetsov, and Z. V. Metreveli. Universality of hadron jets in soft and hard particle interactions at high-energies. *Z. Phys.*, C33:363, 1987.

[21] J. Barrette et al. Two-proton correlations from 14.6-A-GeV/*c* Si + Pb and 11.5-A-GeV/*c* Au + Au central collisions. *Phys. Rev.*, C60:054905, 1999.

[22] S. A. Bass and A. Dumitru. Dynamics of hot bulk QCD matter: From the quark-gluon plasma to hadronic freeze-out. *Phys. Rev.*, C61:064909, 2000.

[23] S. A. Bass et al. Microscopic models for ultrarelativistic heavy ion collisions. *Prog. Part. Nucl. Phys.*, 41:225–370, 1998.

[24] Steffen A. Bass, Pawel Danielewicz, and Scott Pratt. Clocking hadronization in relativistic heavy ion collisions with balance functions. *Phys. Rev. Lett.*, 85:2689–2692, 2000.

[25] E. Bauge et al. Observation of a saturation in the time scale for multifragment emission in symmetric heavy-ion collisions. *Phys. Rev. Lett.*, 70:3705–3708, 1993.

[26] L. Beaulieu et al. Signals for a transition from surface to bulk emission in thermal multifragmentation. *Phys. Rev. Lett.*, 84:5971–5974, 2000.

[27] M. Belt Tonjes, G.D. Westfall, and A.M. Vandermolen. Clocking hadronization at RHIC. In G.D. Westfall and W. Bauer, editors, *Proceedings of the 17th Winter Workshop on Nuclear Dynamics*. EP Systema Bt., Debrecen, Hungary, 2001.

[28] Marguerite Belt Tonjes. *Using the Balance Function to Search for Late Hadronization in Au+Au Collisions at a Center of Mass Energy of 130 GeV per Nucleon Pair*. Ph.D. thesis, Michigan State University, 2002.

[29] Christoph Berger et al. A measurement of charge properties of quark jets at PETRA. *Nucl. Phys.*, B214:189, 1983.

[30] G. F. Bertsch, P. Danielewicz, and M. Herrmann. Hanbury-Brown-Twiss analysis in a solvable model. *Phys. Rev.*, C49:442, 1994.

[31] G. F. Bertsch and S. Das Gupta. A guide to microscopic models for intermediate energy heavy ion collisions. *Phys. Rept.*, 160:189–233, 1988.

[32] G. F. Bertsch, H. Kruse, and S. D. Gupta. Boltzmann equation for heavy ion collisions. *Phys. Rev.*, C29:673–675, 1984.

[33] Jean-Paul Blaizot and Andre Krzywicki. Soft pion emission in high-energy heavy ion collisions. *Phys. Rev.*, D46:246–251, 1992.

[34] N. Borghini, P. M. Dinh, Jean-Yves Ollitrault, A. M. Poskanzer, and S. A. Voloshin. Effects of momentum conservation on the analysis of anisotropic flow. *Phys. Rev.*, C66:014901, 2002.

[35] Nicolas Borghini, Phuong Mai Dinh, and Jean-Yves Ollitrault. Flow analysis from multiparticle azimuthal correlations. *Phys. Rev.*, C64:054901, 2001.

[36] Nicolas Borghini, Phuong Mai Dinh, and Jean-Yves Ollitrault. A new method for measuring azimuthal distributions in nucleus nucleus collisions. *Phys. Rev.*, C63:054906, 2001.

[37] A. S. Borisov et al. Observation of a high-energy cosmic-ray family caused by a CENTAURO-type nuclear interaction in the joint emulsion chamber experiment at the pamirs. *Phys. Lett.*, B190:226, 1987.

[38] R. Brandelik et al. Evidence for charged primary partons in $e^+e^- \to$ two jets. *Phys. Lett.*, B100:357, 1981.

[39] David A. Brown and Pawel Danielewicz. Partons in phase space. *Phys. Rev.*, D58:094003, 1998.

[40] Frank R. Brown et al. On the existence of a phase transition for qcd with three light quarks. *Phys. Rev. Lett.*, 65:2491–2494, 1990.

[41] A. Capella, U. Sukhatme, C-I Tan, and J. Tran Thanh Van. Dual parton model. *Phys. Rept.*, 236:225–329, 1994.

[42] K. C. Chase and A. Z. Mekjian. Exact methods for expectation values in canonical fragmentation models. *Phys. Rev.*, C52:R2339–R2341, 1995.

[43] Sen Cheng and Scott Pratt. Quantum corrections for pion correlations involving resonance decays. *Phys. Rev.*, C63:054904, 2001.

[44] Sen Cheng and Scott Pratt. Isospin fluctuations from a thermally equilibrated hadron gas, 2002. nucl-th/0207051, submitted to Phys. Rev. C.

[45] Sen Cheng et al. The effect of finite-range interactions in classical transport theory. *Phys. Rev.*, C65:024901, 2002.

[46] S. A. Chin. Transition to hot quark matter in relativistic heavy ion collision. *Phys. Lett.*, B78:552–555, 1978.

[47] S. K. Choi et al. A measurement of Bose-Einstein correlations in e^+e^- annihilation at TRISTAN. *Phys. Lett.*, B355:406–414, 1995.

[48] John C. Collins and M. J. Perry. Superdense matter: Neutrons or asymptotically free quarks? *Phys. Rev. Lett.*, 34:1353, 1975.

[49] Fred Cooper and Graham Frye. Single particle distribution in the hydrodynamic and statistical thermodynamic models of multiparticle production. *Phys. Rev.*, D10:186, 1974.

[50] Fred Cooper, Graham Frye, and Edmond Schonberg. Landau's hydrodynamic model of particle production and electron-positron annihilation into hadrons. *Phys. Rev.*, D11:192, 1975.

[51] Michael Creutz. *Quarks, gluons and lattices*. Cambridge University Press, Cambridge, New York, Melbourne, 1983.

[52] P. Danielewicz and M. Gyulassy. Dissipative phenomena in quark gluon plasmas. *Phys. Rev.*, D31:53–62, 1985.

[53] Pawel Danielewicz. Determination of the mean-field momentum-dependence using elliptic flow. *Nucl. Phys.*, A673:375–410, 2000.

[54] Pawel Danielewicz and Scott Pratt. Delays associated with elementary processes in nuclear reaction simulations. *Phys. Rev.*, C53:249–266, 1996.

[55] S. das Gupta and A. Z. Mekjian. Phase transition in a statistical model for nuclear multifragmentation. *Phys. Rev.*, C57:1361–1365, 1998.

[56] C. Derreth, W. Greiner, H. T. Elze, and J. Rafelski. Strangeness abundances in anti-p nucleus annihilations. *Phys. Rev.*, C31:1360–1364, 1985.

[57] J. Dias de Deus and S. Jadach. On the universality of quark jet fragmentation. *Phys. Lett.*, B70:73, 1977.

[58] H. J. Drescher, M. Hladik, S. Ostapchenko, T. Pierog, and K. Werner. Parton-based Gribov-Regge theory. *Phys. Rept.*, 350:93–289, 2001.

[59] D. Drijard et al. Density, charge and transverse momentum correlations of particles in nondiffractive proton-proton collisions at $\sqrt{s} = 52.5$ GeV. *Nucl. Phys.*, B155:269, 1979.

[60] D. Drijard et al. Quantum number effects in events with a charged particle of large transverse momentum. Part 1. Leading particles in jets. *Nucl. Phys.*, B156:309, 1979.

[61] D. Drijard et al. Quantum number effects in events with a charged particle of large transverse momentum. Part 2. Charge correlations in jets. *Nucl. Phys.*, B166:233, 1980.

[62] W. Ehehalt and W. Cassing. Relativistic transport approach for nucleus nucleus collisions from SIS to SPS energies. *Nucl. Phys.*, A602:449–486, 1996.

[63] H. T. Elze and W. Greiner. Finite size effects for quark-gluon plasma droplets. *Phys. Lett.*, B179:385–392, 1986.

[64] H. T. Elze, W. Greiner, and J. Rafelski. On the color singlet quark-glue-plasma. *Phys. Lett.*, B124:515, 1983.

[65] Hans-Thomas Elze, Walter Greiner, and Johann Rafelski. Color degrees of freedom in a quark-glue plasma at finite baryon density. *Z. Phys.*, C24:361–365, 1984.

[66] Enrico Fermi. High-energy nuclear events. *Prog. Theor. Phys.*, 5:570–583, 1950.

[67] Z. Fodor and S. D. Katz. Lattice determination of the critical point of QCD at finite t and μ. *JHEP*, 03:014, 2002.

[68] Z. Fodor and S. D. Katz. A new method to study lattice QCD at finite temperature and chemical potential. *Phys. Lett.*, B534:87–92, 2002.

[69] Barry A. Freedman and Larry D. McLerran. Fermions and gauge vector mesons at finite temperature and density. 3. The ground state energy of a relativistic quark gas. *Phys. Rev.*, D16:1169, 1977.

[70] S. J. Gaff, A. Galonsky, C. K. Gelbke, T. Glasmacher, M. Huang, J. J. Kruse, G. J. Kunde, R. Lemmon, W. G. Lynch, M. B. Tsang, J. Wang, and P. D. Zecher. Time scales from two-neutron intensity interferometry for the reaction Ar-40 + Ho-165 at E/A = 25 MeV. *Phys. Rev.*, C58:2161–2166, 1998.

[71] Sean Gavin and Joseph I. Kapusta. Kaon and pion fluctuations from small disoriented chiral condensates. *Phys. Rev.*, C65:054910, 2002.

[72] Klaus Geiger and Berndt Müller. Dynamics of parton cascades in highly relativistic nuclear collisions. *Nucl. Phys.*, B369:600–654, 1992.

[73] Murray Gell-Mann. A schematic model of baryons and mesons. *Phys. Lett.*, 8:214–215, 1964.

[74] Murray Gell-Mann and M Levy. The axial vector current in beta decay. *Nuovo Cim.*, 16:705, 1960.

[75] R. Ghetti et al. Neutron-neutron intensity interferometry in E/A = 45 MeV Ni-58 + Al-27, Ni-nat and Au-197 reactions. *Phys. Rev.*, C62:037603, 2000.

[76] S. L. Glashow. Partial symmetries of weak interactions. *Nucl. Phys.*, 22:579–588, 1961.

[77] Roy J. Glauber. Coherent and incoherent states of the radiation field. *Phys. Rev.*, 131:2766–2788, 1963.

[78] Gerson Goldhaber. Multi-pion correlations in e^+e^- annihilation at SPEAR. In J. Dias de Deus and J. Soffer, editors, *Proceedings of the Int. Conf. on High Energy Physics, Lisbon, 1981*. European Physical Society, Erice, 1982.

[79] Gerson Goldhaber, Sulamith Goldhaber, Won-Yong Lee, and Abraham Pais. Influence of Bose-Einstein statistics on the antiproton proton annihilation process. *Phys. Rev.*, 120:300–312, 1960.

[80] K. Goulianos. Diffractive interactions of hadrons at high-energies. *Phys. Rept.*, 101:169, 1983.

[81] D. E. Groom et al. Review of particle physics. *Eur. Phys. J.*, C15:1, 2000.

[82] D. J. Gross and Frank Wilczek. Asymptotically free gauge theories. I. *Phys. Rev.*, D8:3633–3652, 1973.

[83] D. J. Gross and Frank Wilczek. Ultraviolet behavior of non-Abelian gauge theories. *Phys. Rev. Lett.*, 30:1343–1346, 1973.

[84] D. J. Gross and Frank Wilczek. Asymptotically free gauge theories. 2. *Phys. Rev.*, D9:980–993, 1974.

[85] Miklos Gyulassy, Yang Pang, and Bin Zhang. Transverse energy evolution as a test of parton cascade models. *Nucl. Phys.*, A626:999–1018, 1997.

[86] Miklos Gyulassy and Xin-Nian Wang. HIJING 1.0: A Monte Carlo program for parton and particle production in high-energy hadronic and nuclear collisions. *Comput. Phys. Commun.*, 83:307, 1994.

[87] M. Y. Han and Yoichiro Nambu. Three-triplet model with double SU(3) symmetry. *Phys. Rev.*, 139:B1006–B1010, 1965.

[88] R. Hanbury Brown and R. Q. Twiss. A new type of interferometer for use in radio astronomy. *Phil. Mag.*, 45:663–682, 1954.

[89] R. Hanbury Brown and R. Q. Twiss. A test of a new type of stellar interferometer on Sirius. *Nature*, 178:1046–1048, 1956.

[90] D. O. Handzy et al. Understanding proton emission in central heavy-ion collisions. *Phys. Rev. Lett.*, 75:2916–2919, 1995.

[91] Ulrich Heinz and Barbara V. Jacak. Two-particle correlations in relativistic heavy-ion collisions. *Ann. Rev. Nucl. Part. Sci.*, 49:529, 1999.

[92] D. Horn and R. Silver. *Ann. Phys.*, 66:509, 1971.

[93] P. Huovinen, P. F. Kolb, Ulrich W. Heinz, P. V. Ruuskanen, and S. A. Voloshin. Radial and elliptic flow at RHIC: Further predictions. *Phys. Lett.*, B503:58–64, 2001.

[94] Sangyong Jeon and Joseph Kapusta. Linear extrapolation of ultrarelativistic nucleon nucleon scattering to nucleus nucleus collisions. *Phys. Rev.*, C56:468–480, 1997.

[95] Sangyong Jeon and Scott Pratt. Balance functions, correlations, charge fluctuations and interferometry. *Phys. Rev.*, C65:044902, 2002.

[96] Ferencz Jüttner. Das Maxwellsche Gesetz der Geschwindigkeitsverteilung in der Relativtheorie. *Ann. Phys. und Chemie*, 34:856–882, 1911.

[97] David E. Kahana, Declan Keane, Yang Pang, Tom Schlagel, and Shan Wang. Collective flow from the intranuclear cascade model. *Phys. Rev. Lett.*, 74:4404–4407, 1995.

[98] Frithjof Karsch. Thermodynamics of 2 and 3 flavour qcd. *AIP Conf. Proc.*, 602:323–332, 2001.

[99] J. H. Koch, N. Ohtsuka, and E. J. Moniz. Nuclear photoabsorption and compton scattering at intermediate-energy. *Annals Phys.*, 154:99–160, 1984.

[100] P. Koch, B. Muller, and J. Rafelski. Strangeness in relativistic heavy ion collisions. *Phys. Rept.*, 142:167–262, 1986.

[101] P. F. Kolb, Ulrich W. Heinz, P. Huovinen, K. J. Eskola, and K. Tuominen. Centrality dependence of multiplicity, transverse energy, and elliptic flow from hydrodynamics. *Nucl. Phys.*, A696:197–215, 2001.

[102] P. F. Kolb, P. Huovinen, Ulrich W. Heinz, and H. Heiselberg. Elliptic flow at SPS and RHIC: From kinetic transport to hydrodynamics. *Phys. Lett.*, B500:232–240, 2001.

[103] G. Kortemeyer, W. Bauer, K. Haglin, J. Murray, and S. Pratt. Causality violations in cascade models of nuclear collisions. *Phys. Rev.*, C52:2714–2724, 1995.

[104] L. D. Landau. On the multiparticle production in high-energy collisions. *Izv. Akad. Nauk SSSR Ser. Fiz.*, 17:51–64, 1953.

[105] C. M. G. Lattes, Y. Fujimoto, and S. Hasegawa. Hadronic interactions of high-energy cosmic ray observed by emulsion chambers. *Phys. Rept.*, 65:151, 1980.

[106] R. Lednicky and T. B. Progulova. Influence of resonances on Bose-Einstein correlations of identical pions. *Z. Phys.*, C55:295, 1992.

[107] Bao-An Li and Che Ming Ko. Formation of superdense hadronic matter in high-energy heavy ion collisions. *Phys. Rev.*, C52:2037–2063, 1995.

[108] Zi-wei Lin and C. M. Ko. Partonic effects on the elliptic flow at RHIC. *Phys. Rev.*, C65:034904, 2002.

[109] Dénes Molnár and Miklos Gyulassy. New solutions to covariant nonequilibrium dynamics. *Phys. Rev.*, C62:054907, 2000.

[110] Denes Molnar and Miklos Gyulassy. Elliptic flow and freeze-out from the parton cascade mpc. *Nucl. Phys.*, A698:379–382, 2002.

[111] Dénes Molnár and Miklos Gyulassy. Saturation of elliptic flow at RHIC: Results from the covariant elastic parton cascade model MPC. *Nucl. Phys.*, A697:495–520, 2002.

[112] Azwinndini Muronga. Second order dissipative fluid dynamics for ultra- relativistic nuclear collisions. *Phys. Rev. Lett.*, 88:062302, 2002.

[113] J. L. Nagle. First results from RHIC: What are they telling us? In Eric Norman, Lee Schroeder, and Gordon Wozniak, editors, *Nuclear Physics in the 21st Century*, volume 610 of *AIP Conference Proceedings*, pages 70–81. American Institute of Physics, College Park, 2002.

[114] Y. Nara, N. Otuka, A. Ohnishi, K. Niita, and S. Chiba. Study of relativistic nuclear collisions at AGS energies from p + Be $\rightarrow$ Au + Au with hadronic cascade model. *Phys. Rev.*, C61:024901, 2000.

[115] Y. Nara, S. E. Vance, and P. Csizmadia. A study of parton energy loss in Au+Au collisions at RHIC using transport theory. *Phys. Lett.*, B531:209–215, 2002.

[116] K. Niyogi, P. Ghose, and A. K. Ray. Renormalizability and lepton - hadron universality in pion beta decay in a gauge field theory. *Phys. Rev.*, D13:2403–2412, 1976.

[117] Jean-Yves Ollitrault. Flow systematics from SIS to SPS energies. *Nucl. Phys.*, A638:195c–206c, 1998.

[118] S. S. Padula and M. Gyulassy. Pion interferometry of O + AU at 200-A/GeV. *Nucl. Phys.*, A498:555c–560c, 1989.

[119] Sandra S. Padula, Miklos Gyulassy, and Sean Gavin. Pion interferometric tests of transport models. *Nucl. Phys.*, B329:357, 1990.

[120] Y. Pang, T. J. Schlagel, and S. H. Kahana. Cascade for relativistic nucleus collisions. *Phys. Rev. Lett.*, 68:2743–2746, 1992.

[121] C. Pinkenburg et al. Elliptic flow: Transition from out-of-plane to in-plane emission in Au + Au collisions. *Phys. Rev. Lett.*, 83:1295–1298, 1999.

[122] I. U. Pomeranchuk. *Dokl. Akad. Novk. USSR*, 78:889, 1951.

[123] A. M. Poskanzer et al. Centrality dependence of directed and elliptic flow at the SPS. *Nucl. Phys.*, A661:341–344, 1999.

[124] S. Pratt. Pion lasers from high-energy collisions. *Phys. Lett.*, B301:159–164, 1993.

[125] S. Pratt. Validity of the smoothness assumption for calculating two- boson correlations in high-energy collisions. *Phys. Rev.*, C56:1095, 1997.

[126] S. Pratt. What we are learning from correlation measurements. *Nucl. Phys.*, A638:125, 1998.

[127] S. Pratt and K. Haglin. Hadronic phase space density and chiral symmetry restoration in relativistic heavy ion collisions. *Phys. Rev.*, C59:3304–3308, 1999.

[128] S. Pratt and V. Zelevinsky. Explaining Centauro events by formation of pions in the isospin singlet channel. *Phys. Rev. Lett.*, 72:816–819, 1994.

[129] Scott Pratt. Canonical and microcanonical distributions for Fermi systems. *Phys. Rev. Lett.*, 84:4255–4259, 2000.

[130] Scott Pratt and Subal Das Gupta. Statistical models of nuclear fragmentation. *Phys. Rev.*, C62:044603, 2000.

[131] Johann Rafelski and Berndt Muller. Strangeness production in the quark-gluon plasma. *Phys. Rev. Lett.*, 48:1066, 1982. Erratum, ibid 56:2334, 1986.

[132] Krishna Rajagopal and Frank Wilczek. Emergence of coherent long wavelength oscillations after a quench: Application to QCD. *Nucl. Phys.*, B404:577–589, 1993.

[133] Krishna Rajagopal and Frank Wilczek. Static and dynamic critical phenomena at a second order QCD phase transition. *Nucl. Phys.*, B399:395–425, 1993.

[134] Ralf Rapp and Edward V. Shuryak. Resolving the antibaryon production puzzle in high-energy heavy-ion collisions. *Phys. Rev. Lett.*, 86:2980–2983, 2001.

[135] Ralf Rapp and Edward V. Shuryak. Regeneration of anti-protons in ultrarelativistic heavy-ion collisions. *Nucl. Phys.*, A698:587–590, 2002.

[136] Lanny Ray. Correlations, fluctuations and flow at star. In *16th International Conference on Ultrarelativistic Nucleus-Nucleus Collisions, Nantes, France*. 2002. To be published.

[137] RHIC Transport Theory Collaboration. *http://www.phy.duke.edu/rttc/*.

[138] Asher Shor and Ronald S. Longacre. Effects of secondary interactions in proton - nucleus and nucleus-nucleus collisions using the HIJET event generator. *Phys. Lett.*, B218:100, 1989.

[139] Edward V. Shuryak. The correlation of identical pions in multibody production. *Phys. Lett.*, B44:387–389, 1973.

[140] Edward V. Shuryak. Instantons in quark plasma, multi - baryon hadrons and neutron stars. *Phys. Lett.*, B81:65, 1979.

[141] Josef Sollfrank et al. Hydrodynamical description of 200-A-GeV/c S + Au collisions: Hadron and electromagnetic spectra. *Phys. Rev.*, C55:392–410, 1997.

[142] H. Sorge. Highly sensitive centrality dependence of elliptic flow: A novel signature of the phase transition in QCD. *Phys. Rev. Lett.*, 82:2048–2051, 1999.

[143] H. Sorge, H. Stocker, and W. Greiner. Relativistic quantum molecular dynamics approach to nuclear collisions at ultrarelativistic energies. *Nucl. Phys.*, A498:567c–576c, 1989.

[144] An Tai and Ben-Hao Sa. LUCIAE 3.0: A new version of a computer program for firecracker model and rescattering in relativistic heavy- ion collisions. *Comput. Phys. Commun.*, 116:353–365, 1999.

[145] D. Teaney, J. Lauret, and Edward V. Shuryak. Flow at the SPS and RHIC as a quark gluon plasma signature. *Phys. Rev. Lett.*, 86:4783–4786, 2001.

[146] D. Teaney, J. Lauret, and Edward V. Shuryak. Hydro + cascade, flow, the equation of state, predictions and data. *Nucl. Phys.*, A698:479–482, 2002.

[147] Derek Teaney and Raju Venugopalan. Classical computation of elliptic flow at large transverse momentum. *Phys. Lett.*, B539:53–58, 2002.

[148] E. A. Uehling. Transport phenomena in Einstein-Bose and Fermi-Dirac gases. II. *Phys. Rev.*, 46:917–929, 1934.

[149] E. A. Uehling and G. E. Uhlenbeck. Transport phenomena in Einstein-Bose and Fermi-Dirac gases. I. *Phys. Rev.*, 43:552–561, 1933.

[150] Alexander Volya, Scott Pratt, and Vladimir Zelevinsky. Multiple pion production from an oriented chiral condensate. *Nucl. Phys.*, A671:617–643, 2000.

[151] Xin-Nian Wang and Miklos Gyulassy. HIJING: A Monte Carlo model for multiple jet production in p p, p A and A A collisions. *Phys. Rev.*, D44:3501–3516, 1991.

[152] S. Weinberg. *Gravitation and Cosmology*. John Wiley & Sons, New York, 1972.

[153] S. Weinberg. Conceptual foundations of the unified theory of weak and electromagnetic interactions. *Rev. Mod. Phys.*, 52:515–523, 1980.

[154] K. Werner. Strings, pomerons, and the VENUS model of hadronic interactions at ultrarelativistic energies. *Phys. Rept.*, 232:87–299, 1993.

[155] Urs Achim Wiedemann and Ulrich Heinz. Particle interferometry for relativistic heavy-ion collisions. *Phys. Rept.*, 319:145–230, 1999.

[156] G. Wolf, G. Batko, W. Cassing, U. Mosel, K. Niita, and M. Schäfer. Dilepton production in heavy ion collisions. *Nucl. Phys.*, A517:615–638, 1990.

[157] Cheuk-Yin Wong. Dynamics of nuclear fluid. VIII. time-dependent Hartree-Fock approximation from a classical point of view. *Phys. Rev.*, C25:1460–1475, 1982.

[158] E. E. Zabrodin, C. Fuchs, L. V. Bravina, and Amand Faessler. Elliptic flow at collider energies and cascade string models: The role of hard processes and multi-pomeron exchanges. *Phys. Lett.*, B508:184–190, 2001.

[159] Bin Zhang. ZPC 1.0.1: A parton cascade for ultrarelativistic heavy ion collisions. *Comput. Phys. Commun.*, 109:193–206, 1998.

[160] Bin Zhang, Miklos Gyulassy, and Che Ming Ko. Elliptic flow from a parton cascade. *Phys. Lett.*, B455:45–48, 1999.

[161] Bin Zhang, Miklos Gyulassy, and Yang Pang. Equation of state and collision rate tests of parton cascade models. *Phys. Rev.*, C58:1175–1182, 1998.

[162] Bin Zhang, C. M. Ko, Bao-An Li, and Zi-wei Lin. A multi-phase transport model for nuclear collisions at RHIC. *Phys. Rev.*, C61:067901, 2000.

[163] Bin Zhang and Yang Pang. Frame dependence of parton cascade results. *Phys. Rev.*, C56:2185–2190, 1997.

[164] J. Zimanyi and T. Csörgő. Multi-boson correlations using wave-packets. I: Exact results. *Heavy Ion Phys.*, 9:241, 1999.